

UNIVERSITY OF CALIFORNIA

Los Angeles

Thermal Isostasy:

Spreading Ridges, Fracture Zones, and Thermal Swells


A dissertation submitted in partial satisfaction of  
the requirement for the degree of Doctor of Philosophy  
in Geophysics and Space Physics

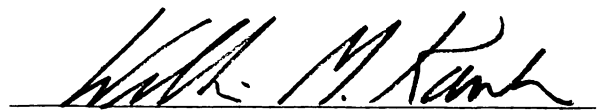
by

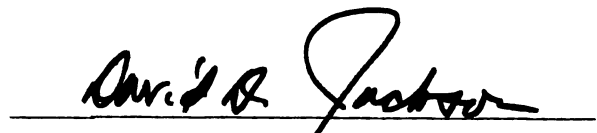
David Thomas Sandwell

1981


The dissertation of David Thomas Sandwell is approved.

  
\_\_\_\_\_  
LeRoy M. Dorman

  
\_\_\_\_\_  
William M. Kaula

  
\_\_\_\_\_  
David D. Jackson

  
\_\_\_\_\_  
Henry W. Menard

  
\_\_\_\_\_  
Gerald Schubert, Committee Chair

University of California, Los Angeles

1981

The dissertation of David Thomas Sandwell is approved.

---

LeRoy M. Dorman

---

William M. Kaula

---

David D. Jackson

---

Henry W. Menard

---

Gerald Schubert, Committee Chair

University of California, Los Angeles

1981

TABLE OF CONTENTS

	Page
ACKNOWLEDGMENTS . . . . .	v
VITA and PUBLICATIONS . . . . .	vi
ABSTRACT. . . . .	vii
INTRODUCTION. . . . .	1
CHAPTER 1. SPREADING RIDGES. . . . .	14
Geoid Height Versus Age for Symmetric Spreading Ridges. . . . .	15
Appendix A: Derivation of the Geoid Height-Age Relation for the Plate Cooling Model. . . . .	22
CHAPTER 2. FRACTURE ZONES. . . . .	25
Geoid Height-Age Relation from Seasat Altimeter Profiles Across the Mendocino Fracture Zone . . . . .	26
Appendix A: A Simple Fracture Zone Model. . . . .	64
Appendix B: A Physical Fracture Zone Model. . . . .	66
Lithospheric Flexure at Fracture Zones. . . . .	77
Appendix A: Temperatures in the Vicinity of a Fracture Zone . . . . .	115
Appendix B: A Method for Determining the Solution Coefficients. . . . .	117
CHAPTER 3. THERMAL SWELLS. . . . .	127
A Compensation Mechanism for the Central Pacific. . . . .	128
Appendix A: Derivation of Equation 12 . . . . .	136
Thermal Isostasy: The Response of a Moving Lithosphere to a Distributed Heat Source . . . . .	139
Appendix A: The Thermomechanical Response of a Moving Lithosphere to a Distributed Heat Source . . . . .	191
Appendix B: Response Functions for Lithospheric Thinning. . . . .	201
REFERENCES for INTRODUCTION . . . . .	212



## ACKNOWLEDGMENTS

All of the members of the dissertation committee have played an important role in directing and supervising the research contained within this dissertation. I especially thank Gerald Schubert for teaching me how to focus on the key aspects of each research topic, LeRoy Dorman for helping me through the many sticky data analysis and mathematical problems, and William Kaula for convincing me to pursue a Ph.D. The software developed by Bob Parker and Loren Shure has saved me months of programming and illustration time.

Much of the text of this manuscript is reprinted from the Journal of Geophysical Research. The coauthors listed in these publications have directed and supervised this research.

## VITA

- April 7, 1953 -- Born, Hartford, Connecticut.
- 1971 - 1974 -- Rensselaer Polytechnic Institute.
- 1974 - 1975 -- B.S., University of Connecticut.
- 1976 - 1978 -- M.S., University of California, Los Angeles.
- 1977 - 1981 -- Research Assistant, Department of Earth and Space Sciences, University of California, Los Angeles.

## PUBLICATIONS

- Sandwell, D.T. and K.A. Poehls, A compensation mechanism for the Central Pacific, J. Geophys. Res., 85, no. B7, 3751-3758, 1980.
- Sandwell, D.T. and G. Schubert, Geoid height versus age for symmetric spreading ridges, J. Geophys. Res., 85, no. B12, 7235-7241, 1980.
- Sandwell, D.T., Thermal Isostasy: the response of a moving lithosphere to a distributed heat source, J. Geophys. Res., in press, 1981.
- Sandwell, D.T. and G. Schubert, Lithospheric flexure at fracture zones, J. Geophys. Res., in press, 1981.
- Sandwell, D.T. and G. Schubert, Geoid height-age relation from Seasat altimeter profiles across the Mendocino fracture zone, J. Geophys. Res., submitted, Aug. 21, 1981.
- Liu, C.S., D.T. Sandwell, and J.R. Curray, The negative gravity field over the 85°E ridge, J. Geophys. Res., submitted, Nov. 15, 1981.

ABSTRACT OF DISSERTATION

Thermal Isostasy:  
Spreading Ridges, Fracture Zones, and Thermal Swells

by

David Thomas Sandwell

Doctor of Philosophy in Geophysics and Space Physics

University of California, Los Angeles, 1981

Professor Gerald Schubert, Chair

Some mesoscale variations in seafloor depth are maintained by thermal buoyancy forces within the oceanic lithosphere. These features are classified as spreading ridges, fracture zones, or thermal swells depending upon their morphology. Recently, accurate measurements of ocean geoid heights have provided a new data type which I use with other geophysical observations to study these thermotectonic features and to infer the thermal and mechanical structure of the oceanic lithosphere.

Correlations of geoid height with age over symmetric spreading ridges are in agreement with predictions of several lithospheric cooling that were proposed to explain the depth-age relation. Large uncertainties in these geoid height-age estimates, which precluded discrimination among the cooling models, were reduced by examining geoid height steps across the large age offset (~25 Myr) Mendocino fracture zone, FZ. The more accurate FZ-derived geoid-age estimates demonstrate that the lithospheric thermal structure deviates from the boundary layer cooling model at a young age (20 - 30 Myr).

Small but systematic deviations between the model and observed FZ geoid steps indicate that FZ's do not slip vertically. This no-slip hypothesis is tested by comparing 5 bathymetric profiles crossing the Mendocino and Pioneer FZ's to the predictions of a lithospheric flexure model. Best fitting models have no-slip and require an increase in flexural rigidity with age. The model also explains ridge and trough type topography that is characteristic of both young and old FZ's.

The Hawaiian swell is also investigated, using geoid height and bathymetry data. Compensation models demonstrate the lower two-thirds of the lithosphere was replaced by hot mantle material. This litho-

spheric reheating is modelled by an elastic-plastic lithosphere passing through a three-dimensional heat source. The model generates heat flow, bathymetry, and gravitational potential for an arbitrarily shaped heat source. This general formulation also allows creation of spreading ridge and FZ models by simply varying the heat source geometry. Therefore, this model establishes a link between the three morphologically distinct features.

## INTRODUCTION

Horizontal temperature gradients within the oceanic lithosphere produce many of the large scale morphological features that appear in the seafloor topography including spreading ridges, fracture zones, and thermal swells. Thermomechanical models of these features have been developed primarily to match the observed bathymetry, heat flow, gravity, and seafloor magnetic data. Recently, accurate measurements of ocean geoid heights by the Geos-3 and Seasat radar altimeters have provided an alternate information source for these thermotectonic features. In this dissertation I use this geoid height data to re-examine these features from a slightly different point of view.

Geoid height, unlike seafloor topography or surface heat flow, is sensitive to the depth and horizontal extent of the stresses that are maintaining the elevated seafloor. However, it is also influenced by lateral density variations in the mantle. As I will show, it is difficult to separate the lithospheric geoid contribution from the mantle geoid contribution. Therefore, I have used these data mainly to test and refine existing models. In the few cases where the model geoid heights systematically disagreed with the observed geoid heights, I have used the differences to make new inferences about the thermo-mechanical properties and structure of the oceanic lithosphere. While confirming existing models appears to be a rather uninteresting research topic, it has led to some unexpected and interesting results.

Furthermore this reinvestigation of spreading ridges, fracture zones, and thermal swells, from a geodetic point of view, clearly demonstrates that they originate from common physical processes.

This study is divided into three chapters corresponding to the three main classifications of thermotectonic features. In Chapter 1 I examine the change in geoid height with crustal age for a number of symmetric spreading ridges. Chapter 2 is devoted to the study of geoid height and bathymetry across the Mendocino and Pioneer fracture zones. Finally, in Chapter 3 I investigate the relationship between geoid height and bathymetry over the Hawaiian Swell. The underlying connection between these three types of thermotectonic features is presented in the final part of Chapter 3 where I propose a general thermomechanical model for the response of a moving lithosphere to a distributed heat source.

Each chapter is composed of one or two research papers. Since the papers were designed for publication, they contain separate introductions, conclusions, equation numbers, figure numbers, references, etc. Also they do not contain some of the non-essential technical aspects of the research. For completeness, I have added important derivations and numerical calculation techniques as appendices to each paper. None of the papers contains the background material that is required to make a Ph.D. dissertation as nearly as self contained and coherent as possible. The remainder of this introduction is devoted to this goal. The topics include: 1) A description of the ocean geoid, i.e. what geoid undulations represent, how they are measured,

and the type of errors they contain; 2) A discussion of how the thermal and mechanical properties of the earth are used to constrain the possible density structures that are consistent with the external gravity field; 3) An overview of this dissertation to point out the logical progression from one study to the next.

The geoid is defined as the equipotential surface of the earth that coincides with the mean sea surface when it is undisturbed by winds or tides. Suppose the earth was a uniformly rotating, self-gravitating mass of inviscid fluid. It would be in a state of hydrostatic equilibrium and its shape would be roughly an ellipsoid of revolution (Clairaut, 1743). This ideal mathematical figure of the earth, called the spheroid, has been calculated from the earth's rotation rate and its radial density structure (Darwin, 1910). Geoid heights, which are deviations of the geoid from the spheroid, result from deviatoric stresses within the earth.

Various methods have been proposed for determining geoid undulations including integration of astrogeodetic observations, Stokes integration of surface gravity measurements, tracking of artificial satellites, and satellite tracking of orbiting radar altimeters. A combination of the final two techniques has provided a remarkably accurate determination of oceanic geoid undulations. The lower degree and order spherical harmonic coefficients ( $l, m \leq 36$  Lerch et al., 1981) are most accurately determined by precisely tracking orbital perturbations of artificial satellites (Kaula, 1966). The higher harmonics of the gravity field cannot be accurately determined by this technique



for two main reasons. First at typical satellite altitudes, the orbital perturbations due to shorter wavelength variations in the gravity field are small because of upward continuation. Second, the amplitude of the gravity field decreases rapidly with increasing degree (i.e. as  $l^{-2}$ , Kaula, 1969). This insensitivity of a satellite's orbit to the higher harmonics of the gravity field is, however, the ideal situation for an orbiting radar altimeter. Perhaps the simplest, most accurate method of measuring the shorter wavelength sea surface undulations is to place a satellite into a nearly circular orbit and have the satellite continually monitor its own altitude above the seasurface using a radar altimeter. This altitude is then subtracted from the distance between the satellite and the earth's center of mass to determine the geoid and ultimately the geoid height.

In practice, the altimeter technique has exceeded expectations (Stanley, 1979). The largest errors arise from an incomplete knowledge of the satellite's radial position. Fortunately, these orbit determination errors introduce long wavelength trends ( $> 4000$  km) in individual altimeter profiles. Since the long wavelength geoid undulations are known quite accurately, the altimetric data has been combined with the low degree and order spherical harmonic coefficients to produce an ocean geoid height model with an accuracy of less than one meter on a  $1^\circ$  by  $1^\circ$  grid (Rapp, 1979; Marsh et al., 1981). The data in this  $1^\circ$  by  $1^\circ$  form are used in Chapters 1 and 3 to investigate symmetric spreading ridges and thermal swells, respectively.

In Chapter 2 I have used the individual altimeter profiles

since they contain the shorter wavelengths that are needed to resolve the fracture zone geoid step. In this form, repeat passes of Seasat altimeter data show significant coherence for geoid undulations with wavelengths greater than 30 km and nearly perfect coherence within the wavelength band 100 to 4000 km (Brammer and Sailor, 1981). Moreover, in this wavelength band the signal to noise ratio is typically greater than 50. These attributes of the altimeter data along with the global oceanic coverage (i.e. a track spacing of 0.6 degrees at the equator) make the data ideally suited for studying intermediate wavelength tectonic features.

In the southern oceans Seasat coverage is nearly an order of magnitude more complete than the bathymetric coverage. Indeed, these data could be used to locate unsurveyed portions of fracture zones and to identify large seamounts that have not been detected by other geophysical methods. Before this can be attempted, however, we must understand how seafloor bathymetry is reflected in geoid undulations.

The external gravity field is nonuniquely related to the internal mass distribution of the earth. Because of this, it is not clear that there should be any relationship between geoid height and other observables such as bathymetry and crustal age. However a knowledge of the earth's thermal and rheological properties can be used to "reduce" this nonuniqueness.

The primary source of rheological information comes from the analysis of post-glacial rebound data. The rapid melting of the Laurentide and Fennoscandia ice sheets approximately 17,000 years ago

produced a spatial redistribution of about  $3 \times 10^{17}$  kg of water. The earth's mechanical and gravitational response to this load shift is revealed in time variations in eustatic sea level (Walcott, 1973). A visco-elastic earth model with a 100 km thick elastic lithosphere and a mantle with a constant viscosity of  $10^{17} \text{ m}^2 \text{ s}^{-1}$  is consistent with global time variations in sea level that have taken place over the last several thousand years (Cathles, 1975; Peltier, 1976). From this value of mantle viscosity or even directly from the emergence data it is evident that the mantle relieves deviatoric stresses over a characteristic time of 5000 years. The lithosphere, on the other hand, can maintain deviatoric stresses for more than a few million years.

These ideas naturally led to the concept of isostatic compensation which plays a crucial role in this dissertation. Suppose that mantle convection was shut off a few million years ago. Since the viscous relaxation time of the mantle is much less than  $10^6$  yr, the entire earth, except for the higher viscosity lithosphere, would be in a state of hydrostatic equilibrium; all geoid undulations would arise from stresses within the lithosphere. Suppose further that the rheology of the lithosphere is linear and isotropic. Under these conditions the geoid height is an isotropic linear functional of the topography (Dorman and Lewis, 1970). Moreover, the lithospheric density structure is uniquely related to the gravity field and the topography.

As we all know, the earth does not satisfy these ideal conditions; however, it may come close. All compensation models that have been proposed for seafloor topography including local compensation models such as Airy or Pratt type compensation, regional compensation

models incorporating an elastic or viscoelastic lithosphere, and the thermal compensation model presented in Chapter 3, predict that the relationship between geopotential and topography is isotropic and linear. This knowledge of the earth's rheology justifies the first major assumption that is implicitly used throughout this dissertation: a portion of the observed geoid undulations are coherent and in phase with the seafloor topography.

The largest uncertainty in the interpretation of geoid height comes from an incomplete knowledge of the deviatoric stresses associated with mantle convection. For wavelengths greater than about 1000 km, the geoid undulations associated with mantle convection are sometimes greater than the geoid heights arising from stresses within the lithosphere. Indeed most of the data analysis in this dissertation deals with separating the lithospheric geoid contribution from the mantle geoid contribution.

In Chapter 1 we have assumed that the lithospheric contribution to the geoid is correlated with the age of the lithosphere just as seafloor depths are correlated with age. Moreover, we have assumed that mantle convection patterns are on the average uncorrelated with age. Certainly, mantle flow and crustal age are correlated, at least in the vicinity of the spreading center, because mantle material must replace the void left behind by the moving plates. However, this upwelling may produce only a small geoid signal. Indeed, some boundary layer convection models indicate that the subduction zones drive the convection and ridges are the sites of passive upwelling (Turcotte

and Oxburgh, 1967; Hager and O'Connell, 1981). These ideas are also consistent with the geoid height data since recently it was shown that subduction zones are a dominant source of long and intermediate wavelength geoid undulations (Kaula, 1980; McAdoo, 1981). However, the final justification for treating the mantle geoid signal as uncorrelated noise comes from the results of our own geoid height-age correlations which show approximate agreement with the predictions of the simple lithospheric cooling models.

The major problem that we encountered in this geoid height-age study was that the amplitude of the uncorrelated geoid signal was sometimes greater than the amplitude of the correlated geoid signal. This produced large uncertainties in the geoid height-age estimates. To improve the signal to noise ratio we examined the step in the geoid height associated with the large age offset ( $\sim 25$  Myr) across the Mendocino FZ (Chapter 2). In general, the FZ geoid step is smooth and the overall change in geoid height takes place over a distance of several hundred kilometers. However, the step is superimposed upon longer wavelength geoid undulations that are apparently unrelated to the FZ. The two signals were separated by fitting the gravitational edge effect model (Dorman, 1975), plus a regional trend, to the observed geoid height profiles. The parameters of the best fitting model provided an estimate of the overall geoid offset. These geoid offset estimates were normalized by the age offsets along the FZ (Atwater and Menard, 1970) to construct a geoid height-age relation for ages 15-135 Myr. As expected, the uncertainties in this geoid height-age

relation are less than one half the size of the uncertainties in the geoid height-age estimates derived from the symmetric spreading ridges. These smaller uncertainties allow us to demonstrate that the thermal structure of the lithosphere, along the Mendocino FZ, begins to deviate from the prediction of the boundary layer cooling model at a very young age (20-30 Myr).

In the process of fitting the gravitational edge effect model to the individual altimeter profiles we found a small but systematic discrepancy between the model and the observations. Twenty-two of the 28 profiles that we examined show a small depression on the older side of the FZ that could not be matched by the model. We surmised that the model failed because it did not account for thermal and mechanical interactions between the lithospheric segments on either side of the FZ. We first calculated the effect of thermal coupling on the geoid step (i.e. lateral heat conduction). However, we found that this only broadens the geoid step and does not produce the observed asymmetry in the step. Next we investigated the effect of mechanical coupling. If complete mechanical coupling occurs (i.e. no vertical slip) then the lithosphere must flex to accommodate the difference in subsidence rates across the FZ. Initial modelling showed that this effect could explain much of the discrepancy between the observed and model geoid steps but only if the Mendocino FZ did not slip vertically at any time during its evolution. The model also predicted that the bathymetry adjacent to the FZ should deviate by hundreds of meters from the depth-age relation. Therefore, it could be tested by matching it to the bathymetric data.

In the final part of Chapter 2 we examine five bathymetric profiles crossing the Mendocino and Pioneer FZ's at various ages to test for the absence of vertical slip on the fossil fault planes. We modeled the flexural part of the FZ topography using the thin elastic plate model that was developed to explain the plate bending at subduction zones and surrounding large seamounts. However, we also had to include the effects of both age-dependent flexural rigidity (Watts, 1978; Caldwell and Turcotte, 1979) and elastic coupling between the Pioneer and Mendocino FZ's to adequately fit the observed profiles. The results of forward modelling indicate that at least these two FZ's have not slipped during their evolutions.

From a theoretical point of view, fracture zone flexure is rather unique since it involves at least two interactions between the thermal and mechanical structure of the lithosphere. First, the amplitude of the flexure results from the difference in thermal subsidence rate across the FZ. Second, the wavelength of the flexure is related to the effective elastic thickness of the lithosphere, which is also a function of the thermal structure.

These thermomechanical interactions will also be important for other features such as thermal swells and spreading ridges when the characteristic wavelength of the lithospheric thermal perturbation is

less than the flexural wavelength. In Chapter 3 I show that the lower bound on the width of a thermal swell is governed by the flexural wavelength. Thus, it is not a coincidence that thermal swells are always wider than the flexural wavelength. In many cases linear seamount chains and the flexural topography they produce are superimposed on thermal swells. The problem of separating these two types of topography has not been considered previously. Those who have interpreted the flexural topography adjacent to the Hawaiian-Emperor seamount chain, have ignored the swell topography (Walcott, 1970; Watts, 1978) while those who have modelled the Hawaiian swell have ignored the seamount chain (Detrick and Crough, 1978; Crough, 1978). Even though these two types of topography have different characteristic wavelengths, they are nevertheless superimposed and there may be significant spectral leakage between them.

In the first part of Chapter 3 we address the problem of separating the topography associated with the Hawaiian swell from the topography produced by the Hawaiian-Emperor seamount chain. Geoid height data were used to discriminate between the two modes of compensation. Following the approach of Dorman and Lewis (1970) the geoid and topography data were summarized by calculating a linear isotropic, geoid height/topography transfer function. When interpreting these transfer function estimates, however, we encountered a number of problems. First, we found that there was no single physically reasonable compensation model that simultaneously fit all of the transfer function estimates within their uncertainties. For example, the best fitting local compensation model, with all of the



compensating masses lying within the lithosphere, did not fit the longer wavelength ( $>1100$  km) transfer function estimates. Similarly, the longer wavelength transfer function estimates could be fit by forcing the compensating masses deeper (i.e. 40-80 km) but this model failed to fit the shorter wavelength estimates. Therefore, we proposed that the shorter wavelength topography, associated with the linear seamount chain, is compensated at shallow depths ( $\sim 14$  km) while the longer wavelength swell topography is compensated much deeper (40 - 80 km). Moreover, we assigned 1100km as the sharp crossover wavelength between the two modes of compensation.

This study posed more questions than it answered. How can this transfer function be physically interpreted in the crossover wavelength band (500-1600 km)? How is the flexural topography distinguished from the swell topography at a distance of 125 to 400 km away from the seamount chain? Is the geoid height isotropically and linearly related to the topography of the elongate thermal swell? Before these problems could be addressed, we needed a theoretical model that could predict the geoid height/topography transfer function for a thermal swell that is created as the lithosphere moves over a hot spot. One-dimensional models have been proposed to explain the subsidence of the swell topography. However, to calculate the geoid height the lithospheric reheating problem must be solved in three dimensions.

In the final part of Chapter 3 I derive a solution to the

three-dimensional reheating problem, which I use to calculate the observable response of a moving lithosphere (i.e. the surface heat flow, the seafloor topography, and the gravitational potential) to a stationary embedded heat source. The heat source representation is used as a means of rapidly heating or reheating the lithosphere without introducing the nonlinear mathematics associated with upwelling of mantle material at a spreading ridge or hot spot. From this linear solution to the problem I demonstrate that the geoid/topography transfer function for an elongate thermal swell is indeed linear and it is nearly isotropic ( 10-20% anisotropic). A comparison of this thermal transfer function with the flexure transfer function shows that the two are partially separated in wavelength space at the flexural wavelength, however, there is a rather broad wavelength band, 300-1000 km where the two transfer functions overlap.

Perhaps the most important aspect of the thermomechanical model of lithospheric reheating is that it can be used to calculate the surface heat flow, the seafloor topography, and the geopotential for any time-independent thermal structure. These models include: symmetric/anti-symmetric spreading ridges, fracture zones, and arbitrarily shaped thermal swells. Some of these thermotectonic features can be modelled using other techniques, however the more general formulation of the problem (Chapter 3) clearly demonstrates that the three morphologically distinct features, that I re-examine in this dissertation, have a common physical connection; they are all isostatically compensated by thermal buoyancy forces within the lithosphere.

CHAPTER 1  
SPREADING RIDGES

## Geoid Height Versus Age for Symmetric Spreading Ridges

DAVID SANDWELL AND GERALD SCHUBERT

*Department of Earth and Space Sciences, University of California at Los Angeles, Los Angeles, California 90024*

Geoid height-age relations have been extracted from Geos 3 altimeter data for large areas in the North Atlantic, South Atlantic, southeast Indian, and southeast Pacific oceans. Except for the southeast Pacific area, geoid height decreases approximately linearly with the age of the ocean floor for ages less than about 80 m.y. in agreement with the prediction of an isostatically compensated thermal boundary layer model (Haxby and Turcotte, 1978). The geoid-age data for 0 to 80 m.y. are consistent with constant slopes of  $-0.094 \pm 0.025$ ,  $-0.131 \pm 0.041$ , and  $-0.149 \pm 0.028$  m/m.y. for the South Atlantic, southeast Indian, and North Atlantic regions, respectively. For ages greater than 80 m.y. the geoid-age relation for the North Atlantic is nearly flat, indicating a reduction in the rate of boundary layer thickening with age. The uncertainties in the geoid slope-age estimates are positively correlated with spreading velocity.

### INTRODUCTION

It has long been recognized that the horizontally rigid plates sliding across the earth are the surface expressions of large-scale mantle convection. The plates themselves are thermomechanical boundary layers associated with convection at highly supercritical Rayleigh number [Turcotte and Oxburgh, 1967; Schubert, 1979]. The density variations associated with the lithospheric boundary layer contribute significantly both to the forces driving the plates [Hager, 1978; Schubert, 1980] and to the departures in the shape of the earth (geoid) from hydrostatic equilibrium [Kaula, 1972]. Density anomalies not associated with the thermal structure of the lithosphere also contribute to the geoid and tend to mask the lithospheric signal.

A theoretical lithospheric geoid signal has been derived by Haxby and Turcotte [1978] by using a long-wavelength, flat earth approximation to the geoid height  $N$  of an isostatically compensated thermal boundary layer:

$$N = \frac{-2\pi G \rho_m \alpha (T_m - T_0) \kappa}{g} \left[ 1 + \frac{2\rho_m \alpha (T_m - T_0)}{(\rho_m - \rho_w) \pi} \right] t \quad (1)$$

where  $g$  is the acceleration of gravity,  $G$  is the gravitational constant,  $\alpha$  is the thermal expansion coefficient,  $(T_m - T_0)$  is the temperature difference across the surface thermal boundary layer,  $\kappa$  is the thermal diffusivity,  $\rho_m$  is mantle density,  $\rho_w$  is seawater density, and  $t$  is the age of the crust. Equation (1), which is based on the indefinite growth of a thermal boundary layer at the upper boundary of a cooling semi-infinite half space, predicts that geoid height should decrease linearly with increasing crustal age. Chapman [1977] has found that geoid height decreases with crustal age for individual tracks of Geos 3 data crossing the southwest Indian ridge. A similar decrease has also been observed [Haxby and Turcotte, 1978; Haxby, 1979] for tracks of Geos 3 data that cross a number of spreading ridges, including one that crosses the northern Mid-Atlantic Ridge. That particular track shows a decrease consistent with a linear geoid height-age relation of slope  $-0.16$  m/m.y. for ages less than 50 m.y. For at least this one track it is apparent that the part of the geoid due to density anomalies associated with lithospheric cooling and subsidence is dominating the overall convective signal. However, as we will see in the following section, a geoid height-age dependence is not usually apparent when observed geoid height contours are super-

imposed on isochrons of the world's oceans. Thus the signal of the isostatically compensated oceanic lithosphere is hidden in the observed geoid. It is not even clear that this signal can be extracted from the data, since its predicted magnitude is 10-15 m (see the model results of Figure 7) while typical geoid undulations are 33 m [Kaula, 1966]. We will show that the lithospheric contribution to the geoid can be obtained from observations. Moreover, we will demonstrate that the signal is consistent with the theoretical linear geoid height-age relation for young ages but deviates from it for ages greater than 80 m.y.

Our study is made possible by the extensive oceanic coverage of the Geos 3 altimeter. These sea surface measurements are ideally suited to the study of the variations of the gravitational potential over spreading ridges because the signal-to-noise ratio of these data is near its peak for wavelengths between 800 and 4000 km. In contrast, the signal-to-noise ratio for shipboard gravity measurements is low in this wavelength interval [Chapman and Talwani, 1979].

### DATA ANALYSIS

Sea surface heights averaged over  $1^\circ$  by  $1^\circ$  areas were obtained from processed Geos 3 altimeter data [Rapp, 1979]. The relatively small deviations between the sea surface and the geoid caused by oceanic circulation were neglected in this analysis. Age data taken from Pitman *et al.* [1974] were averaged over  $2^\circ$  by  $2^\circ$  areas since there was insufficient resolution for reliable  $1^\circ$  by  $1^\circ$  averages. Crustal ages for  $2^\circ$  by  $2^\circ$  areas in the Cretaceous quiet zone (85-110 m.y.) were obtained by linearly interpolating between magnetic lineations. Four oceanic regions containing both geoid and age data were chosen for study. The boundaries of these regions were adjusted to insure that equal areas of seafloor were contained within each 5 to 10 m.y. time interval on either side of the ridge. Figure 1 shows the outline of each area. The velocity vectors indicate present-day plate motions [Minster and Jordan, 1978].

Figure 2 shows a contour map of the geoid (heavy lines) superimposed upon age contours (dashed lines) for the region in the South Atlantic. There is no geoid height-age relationship obvious on the basis of a visual inspection of these contours. If geoid height were strictly related to age, the contours would be parallel, and geoid heights would be symmetric about the ridge. However, a large-amplitude long-wavelength geoid undulation, trending roughly NW to SE, effectively masks the age-dependent signal. Geoid height and age contours in either

Copyright © 1980 by the American Geophysical Union.

Paper number 80B0926.  
0148-0227/80/080B-0926\$01.00

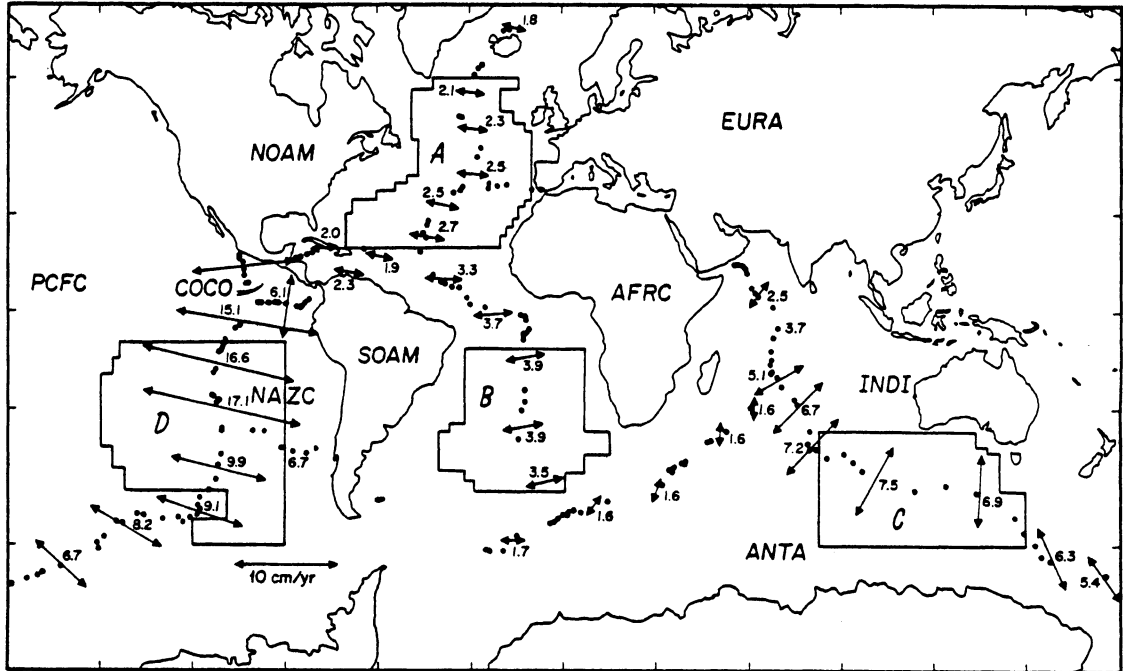


Fig. 1. World map outlining areas chosen for geoid height-age analysis. Dots represent earthquake epicenters. Arrows are present-day spreading velocities [Minster and Jordan, 1978].

the southeast Pacific or the southeast Indian Ocean areas outlined in Figure 1 also have no apparent visual correlation. In the area of the North Atlantic (Figure 1), though geoid height contours are symmetric about the ridge, they are not parallel to isochrons because of a long-wavelength trend in the geoid parallel to the ridge (Figure 3).

In order to extract a geoid height-age relation from the data we have calculated the time rate of change of geoid height in the direction of increasing age. This procedure eliminates geoid height variations parallel to the isochrons. Long-wavelength antisymmetric trends across the ridge can be removed by averaging geoid slopes over equal areas within a given time interval on either side of the ridge [Chapman, 1977]. The slope of the geoid in the direction of increasing age  $\partial N/\partial t$  is obtained by taking the scalar product of the horizontal gradient of geoid height  $\nabla_h N$  with the horizontal gradient of crustal age  $\nabla_h t$ :

$$\frac{\partial N}{\partial t} = \frac{\nabla_h N \cdot \nabla_h t}{\nabla_h t \cdot \nabla_h t} \quad (2)$$

Age gradients were computed on a  $2^\circ$  by  $2^\circ$  grid using a first difference formula and the  $2^\circ$  by  $2^\circ$  average age data. A geoid height gradient was obtained at the same point as an age gradient by determining the slope of the plane which best fit the 16 nearest  $1^\circ$  by  $1^\circ$  geoid height determinations. Geoid slopes on the  $2^\circ$  by  $2^\circ$  grid were then calculated from (2). These individual slopes were weighted by the latitude-dependent area of each  $2^\circ$  by  $2^\circ$  square before averaging the slopes within a given time interval. The slope of any  $2^\circ$  by  $2^\circ$  area that straddled a ridge was not included. Most slope estimates were based on averages over 10 to 40 times the area in a  $2^\circ$  by  $2^\circ$  square at the equator. The standard deviations of the average slope estimates were also computed from the individual slopes within each time interval. The magnitudes of the standard deviations are measures of the contributions of density anomalies not directly related to age to the mean slope estimates.

The  $2^\circ$  grid spacing used above eliminates geoid undula-

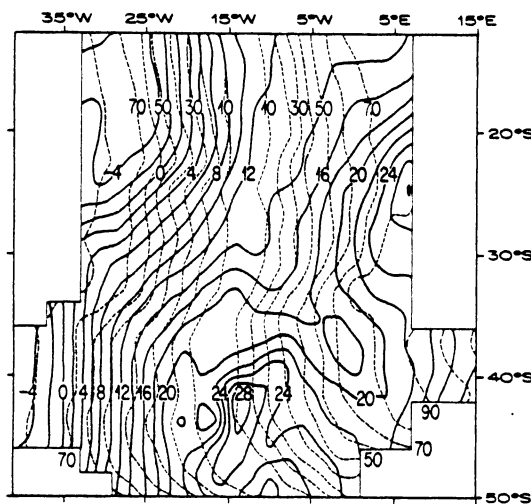


Fig. 2. Geoid height contours (solid curves) and isochrons (dashed curves) superimposed for a large portion of the South Atlantic. Geoid heights are contoured at 2 m intervals and ages are contoured at 10-m.y. intervals. Geoid height contours were made from digitized  $2^\circ \times 2^\circ$  averages.

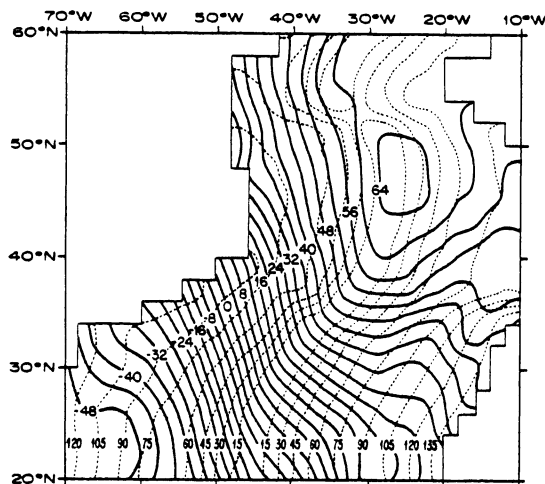


Fig. 3. Geoid heights (solid curves) superimposed on age contours (dashed lines) for a region of the North Atlantic. The geoid is contoured at 4-m intervals, and ages are contoured at 15-m.y. intervals.

tions and age variations with wavelengths shorter than several hundred kilometers. The gradient operation prewhitens the data by dividing their spectra by the wavelength. This suppresses the longest wavelengths and removes the mean.

#### RESULTS

Time rates of change of geoid height in the direction of increasing age for all four oceanic areas are shown in Figure 4. Each data point is the average geoid slope within either 5 m.y. time intervals for the southeast Pacific (Figure 4a) and southeast Indian (Figure 4c) Ocean areas or 10 m.y. time intervals for the North Atlantic (Figure 4a) Ocean and South Atlantic (Figure 4b) Ocean areas. The vertical bars represent 1 standard deviation of the mean. Each dashed horizontal line is the best fitting (in the least squares sense) constant slope approximation to the geoid-age relations for ages less than 80 m.y. The maximum ages range from 50 m.y. for the southeast Indian Ocean area to 130 m.y. for the North Atlantic Ocean area. The upper limits on ages within each area were set by the availability of symmetric age data. Figure 5 shows the geoid height versus age curves for the four oceanic areas obtained by integrating the mean values of the geoid slope versus age data of Figure 4. Table 1 is a compilation of all the data shown in Figures 4 and 6.

##### North Atlantic

The slope estimates for the North Atlantic are negative and statistically different from zero for ages less than 80 m.y. The estimates for greater ages are close to zero and have relatively small uncertainties. A best fitting constant slope was determined to test the prediction of (1). For the 0 to 80 m.y. age interval the mean of the slope estimates weighted by the inverse of their variances is  $-0.149 \pm 0.028$  m/m.y. The constant slope approximation lies within 1 standard deviation of all the slope-age estimates between 0 and 50 m.y. (Figure 4a). The data in the interval 50 to 80 m.y. are not closely approximated by the best fitting constant slope. However, these data have relatively large uncertainties, and therefore they have rela-

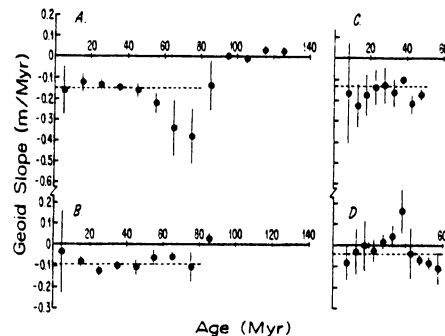


Fig. 4. Estimates of the slope of the geoid in the direction of increasing age, as a function of age, for each of the four oceanic regions outlined in Figure 1. Error bars represent 1 standard deviation. Dashed line is the best fitting constant slope between 0 and 80 m.y. (a) North Atlantic, (b) South Atlantic, (c) SE Indian, (d) SE Pacific.

tively little influence on the value of the best fitting constant slope.

The individual slopes contributing to the mean slope estimates between 50 and 80 m.y. have a nearly bimodal distribution; i.e., they cluster into two groups on either side of the mean. The group with the more negative slopes derives from the region north of  $30^{\circ}\text{N}$ . The portion of this region between the 70-m.y. isochrons (Figure 3) contains both broad residual depth and gravity anomalies [Sclater *et al.*, 1975; Cochran and Talwani, 1977, 1978]. We believe that the anomalous slope in the topography along the perimeter of the residual depth anomaly causes the anomalous geoid slopes in the 50 to 80 m.y. age interval. To substantiate this hypothesis, we computed separate slope estimates for the region lying north of  $30^{\circ}\text{N}$  (Figure 6, solid circles) and for the region lying south of  $32^{\circ}\text{N}$  (Figure 6, open circles). Within the 50 to 80 m.y. age interval the slope estimates for the two regions are quite different.

The integral of the slope-age data for the entire North Atlantic (solid line, Figure 5) yields a drop of 18 m in 90 m.y. If the data north of  $32^{\circ}\text{N}$  are excluded, the drop in the geoid height is only 12.5 m in 90 m.y.

##### South Atlantic

The estimates of geoid slope are nearly constant in the 0 to 80 m.y. age interval. The best fitting linear geoid slope-age re-

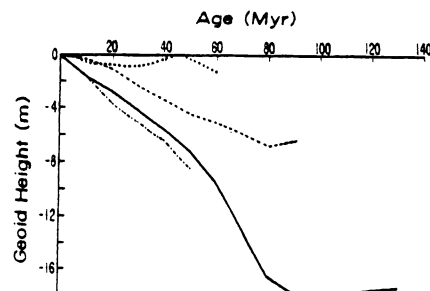


Fig. 5. Geoid height-age relations obtained by integrating the slope estimates of Figure 4. North Atlantic (solid line), South Atlantic (dashed line), SE Indian (dash-dot line), SE Pacific (dotted line).

TABLE I. Average Geoid Slopes

	t, m.y.												
	5	15	25	35	45	55	65	75	85	95	105	115	125
A	8.3	28.5	21.2	17.8	24.2	30.3	37.2	38.6	26.6	18.0	19.0	13.0	10.5
	( $\partial N/\partial t$ )	-0.161	-0.121	-0.133	-0.146	-0.160	-0.220	-0.380	-0.138	0.012	-0.008	0.031	0.028
	$\sigma$	0.115	0.040	0.025	0.010	0.029	0.047	0.113	0.131	0.119	0.018	0.017	0.013
A	4.8	18.8	15.0	11.7	18.0	23.2	26.5	27.0	16.8	7.3	6.6		
	( $\partial N/\partial t$ )	-0.192	-0.129	-0.142	-0.133	-0.173	-0.264	-0.484	-0.206	0.007	-0.048		
	$\sigma$	0.062	0.030	0.016	0.008	0.021	0.041	0.071	0.146	0.016	0.023		
A	4.4	12.3	7.1	7.0	7.9	8.7	12.4	13.3	12.3	13.1	15.0	11.4	9.7
	( $\partial N/\partial t$ )	-0.190	-0.133	-0.111	-0.159	-0.113	-0.096	-0.274	-0.148	0.009	-0.022	0.033	0.040
	$\sigma$	0.168	0.056	0.041	0.012	0.039	0.037	0.191	0.107	0.020	0.017	0.014	0.018
A	35.6	36.0	24.9	29.6	32.6	29.0	35.4	58.0	27.7				
	( $\partial N/\partial t$ )	-0.033	-0.079	-0.123	-0.102	-0.106	-0.062	-0.060	-0.106	0.025			
	$\sigma$	0.194	0.022	0.019	0.018	0.034	0.035	0.024	0.070	0.022			
t, m.y.													
A	27.0	38.2	25.0	25.9	21.0	24.4	19.7	15.2	9.0	8.8			
	( $\partial N/\partial t$ )	0.196	-0.168	-0.227	-0.176	-0.138	-0.129	-0.165	-0.104	-0.219	-0.174		
	$\sigma$	0.610	0.241	0.102	0.098	0.084	0.086	0.065	0.013	0.043	0.022		
A	62.5	70.2	77.7	60.7	44.0	37.7	39.8	31.4	17.4	12.9	5.5	2.3	
	( $\partial N/\partial t$ )	-0.031	-0.084	-0.031	-0.002	-0.026	0.014	0.042	0.162	-0.038	-0.084	-0.109	
	$\sigma$	0.225	0.081	0.106	0.118	0.052	0.029	0.049	0.107	0.118	0.023	0.029	0.074

A is the area normalized by a  $2^\circ$  by  $2^\circ$  square at the equator; ( $\partial N/\partial t$ ) is the mean geoid slope in m/m.y.;  $\sigma$  is the standard deviation in m/m.y.

lation for the South Atlantic,  $-0.094 \pm 0.025$  m/m.y., lies within 1.25 standard deviations of all of the slope estimates in the age range 0 to 80 m.y. (Figure 4b). The one slope estimate for ages greater than 80 m.y. is nearly zero. The relatively small uncertainties in the data and the good overall fit of the constant slope approximation to the geoid height-age relation between 0 and 80 m.y. indicate that a linear geoid height-age relation is consistent with the data from the entire South Atlantic. The integral of the slope-age estimates (dashed line in Figure 5) has a 6 m decrease in the 0 to 80 m.y. time span.

#### Southeast Indian Ocean

The available data for this area extend only to 50 m.y., and the uncertainties in most of the slope estimates are larger than in the Atlantic regions (Figure 4c). The best fitting constant slope of  $-0.131 \pm 0.041$  m/m.y. lies an average of 1.3 standard deviations away from the data. Integration of the slope estimates yields a geoid height-age relation (dash-dot line in Figure 5) with an 8.5 m decrease in 50 m.y.

#### Southeast Pacific

In contrast to the other oceanic areas, geoid height in the southeast Pacific region does not appear to decrease with age (Figure 4d). The overall drop in geoid height (dotted line in Figure 5) between the ages of 0 and 60 m.y. is only 1.5 m. The best fitting constant slope of  $-0.041 \pm 0.054$  m/m.y. lies more than 1 standard deviation away from 5 of the 11 slope estimates. The data within the 20 to 45 m.y. interval are incompatible with a geoid height-age relation of constant negative slope. The slope-age data in this age band reflect the geoid high centered over the Peru-Chile trench. In general, the free air gravity high associated with a subduction zone and its outer rise extends no more than a few hundred kilometers seaward of the trench axis [Watts and Talwani, 1974]. However, all major subduction zones have a geoid high extending roughly 2000 km [McAdoo, 1980] from the trench with an amplitude of more than 20 m [Rapp, 1979]. The geoid anomaly associated with the Peru-Chile trench contributes positive values to slope estimates for seafloor with ages between 10 and 45 m.y. on the east side of the east Pacific rise. As a result, the decrease in geoid height associated with lithospheric cooling is effectively offset in this age interval by the increase in geoid height with proximity to the trench. The failure to extract a meaningful geoid height-age relation in the southeast Pacific could also be due to the complicated ridge geometry, i.e., the presence of a triple junction, and to the presence of fossil spreading ridges.

#### DISCUSSION AND SUMMARY

The general results of the geoid slope-age analysis are the following:

1. Geoid height-age relations associated with lithospheric cooling can be extracted from the observed geoid over oceanic areas.
2. The North Atlantic, South Atlantic, and southeast Indian Ocean regions all have geoid heights which decrease nearly linearly with age for ages less than about 80 m.y., consistent with the signature of an isostatically compensated cooling lithospheric plate.
3. The slope of the geoid in the direction of increasing age is close to zero in the North Atlantic for ages greater than 80 m.y. Only one data point is available for the South Atlantic

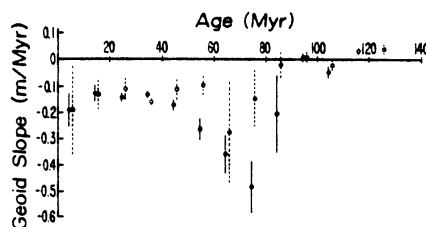


Fig. 6. Estimates of the slope of the geoid in the direction of increasing age, as a function of age, for the North Atlantic north of  $30^{\circ}\text{N}$  (solid circles) and south of  $32^{\circ}\text{N}$  (open circles). The error bars represent 1 standard deviation. The region north of  $30^{\circ}\text{N}$  contains a broad residual depth anomaly.

for ages exceeding 80 m.y. At 85 m.y. the geoid slope in the South Atlantic is also close to zero.

4. Geoid undulations that are unrelated to crustal age cannot be completely removed by the above data analysis technique.

One other conclusion that can be drawn from Figures 1 and 4 is that the uncertainties in the geoid slope estimates have a positive correlation with spreading velocity. This correlation was unexpected, but in retrospect it is easy to explain. Uncertainties in the slope estimates arise from geoid anomalies that are unrelated to age. Since fast spreading ridges (half-rate 3–10 cm/yr) have more seafloor area per time interval than slow spreading ridges (half-rate 0–3 cm/yr), there are more age-independent geoid anomalies per time interval in the faster spreading oceans. When this is combined with the fact that the change in geoid height per time interval is nearly independent of spreading velocity, it is not surprising that this uncertainty-velocity correlation exists. This observation suggests that the best geoid height-age results will come from a reanalysis of the southwest Indian ridge by using more data than were available to Chapman [1977].

Through (1), the slopes of the observed geoid height-age relations (Figure 4) can be used to constrain the value of the product  $\alpha(T_m - T_0)$  appropriate to the oceanic upper mantle. The values of  $\alpha$ ,  $\kappa$ , and  $T_m - T_0$ , derived from the empirical depth-age and heat flow-age relations for the North Atlantic [Parsons and Sclater, 1977], yield a slope of  $-0.16$  m/m.y. This lies within the error bounds of the best fitting constant geoid slope-age relations (ages < 80 m.y.) for both the North Atlantic and southeast Indian oceans. For the South Atlantic a slope of  $-0.16$  m/m.y. falls below all of the uncertainties in the 0 to 80 m.y. slope estimates. More work needs to be done in this region to determine if the depth, heat flow, and geoid data are mutually consistent with the isostatically compensated thermal boundary layer cooling model. The lithospheric cooling model cannot explain the observed geoid slope-age relation for the southeast Pacific region. Since this relation (Figure 4d) is significantly different from the observed geoid slope-age relations of the other three regions, we believe that the lithospheric cooling signal was not successfully extracted from the geoid observations in the southeast Pacific. The geoid anomaly associated with the Peru-Chile trench and the complications associated with the presence of a triple junction and a fossil spreading center in the area of study contribute to the difficulty in deducing the lithospheric geoid signal in the southeast Pacific.

The observed flattening in the geoid height-age relation for



ages greater than 80 m.y. in the North Atlantic cannot be explained by the boundary layer cooling model. Accordingly, we have investigated the possibility that the flattening might be understood in terms of a plate cooling model. In this model [see, e.g., *Parsons and Sclater, 1977*] a plate of constant thickness  $l$  cools to the surface; both the surface temperature  $T_0$  and the temperature at the base of the plate  $T_m$  are held constant. *Parsons and Sclater [1977]* have given analytic formulas for the depth of the ocean  $D(t)$  and the thermally induced density anomaly in the plate. These formulas together with the *Ockendon and Turcotte [1977]* approximation for the geoid height  $N$  can be used to derive the geoid height-age relation for the cooling plate model. The result is

$$N(t) = \frac{-2\pi GP^2}{g} \left\{ (\rho_m - \rho_w) \frac{D^2(t)}{2} + \alpha \rho_m (T_m - T_0) \left[ \frac{1}{6} + \frac{2}{\pi^2} \sum_{n=1}^{\infty} \frac{(-1)^n}{n^2} \exp(-n^2 ct) \right] \right\} \quad (3)$$

where

$$c = \pi^2 \kappa / P^2 \quad (4)$$

$$D(t) = \frac{\alpha \rho_m (T_m - T_0)}{2(\rho_m - \rho_w)} \left( 1 - \frac{8}{\pi^2} \sum_{n=1}^{\infty} \frac{\exp[-(2n-1)^2 ct]}{(2n-1)^2} \right) \quad (5)$$

A flat earth approximation and the neglect of horizontal heat conduction have been assumed in deriving (3).

Figure 7 shows geoid height versus age for the cooling plate model with  $\kappa = 8 \times 10^{-3} \text{ cm}^2/\text{s}$ ,  $\alpha = 3.1 \times 10^{-5} \text{ K}^{-1}$ ,  $\rho_m = 3.33 \text{ g/cm}^3$ ,  $\rho_w = 1.025 \text{ g/cm}^3$ ,  $T_m = 1365^\circ\text{C}$ ,  $T_0 = 0^\circ\text{C}$ ,  $l = 128 \text{ km}$ , and  $g = 982 \text{ cm/s}^2$ . These parameter values are the same as those used by *Parsons and Sclater [1977]* for the North Atlantic. Figure 8 shows the geoid slope of this model as a function of age together with the data for the North Atlantic from Figure 4. The model shows a flattening in the geoid height-age relation and a geoid height which approaches 15 m at old ages (Figure 7). *Parsons and Richter [1980]* have shown that the ridge driving force can be related to the lithospheric geoid anomaly. For a geoid anomaly of about 15 m they obtain a driving force of about  $3.5 \times 10^{13} \text{ dyne/cm}$ . The geoid slope-age relation of this particular model does not compare especially well with the data (Figure 8), which appear to show a more abrupt change from a nearly constant nonzero value of slope to an approximately zero value near 80 m.y.

The observed flattenings of the depth-age and heat flow-

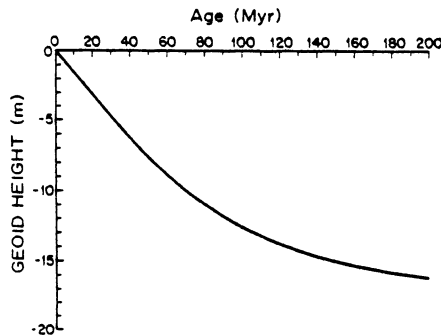


Fig. 7. Geoid height versus age for a cooling plate model of the oceanic lithosphere. The model and parameter values are described in the text.

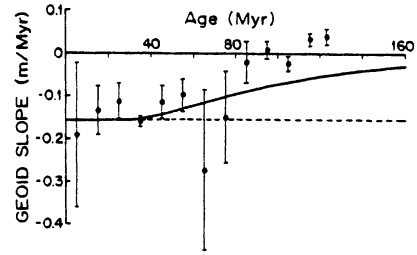


Fig. 8. Geoid slope versus age for the cooling plate model of Figure 7 together with the data for the North Atlantic from Figure 4.

age [*Parsons and Sclater, 1977*] and geoid-age relations indicate that heat is being introduced into the base of the old oceanic lithosphere. Possible heat sources include shear heating [*Schubert et al., 1976*] and small-scale convection [*Richter and Parsons, 1975; Parsons and McKenzie, 1978*]. To discriminate between these various models, the thermal boundary layer signal must be removed from the depth, heat flow, and geoid observations. The results of this study provide an empirical geoid height-age relation that can be removed from the geoid over large oceanic areas, so that the smaller scale upper mantle heat transfer mechanisms can be further investigated.

Finally, we note that significant extensions of this study may be possible by using age data from magnetic lineations identified since the *Pitman et al. [1974]* compilation and from Deep-Sea Drilling Project drill sites and ages inferred from rigid plate rotations. This would facilitate both higher resolution in areas already studied and inclusion of additional areas into the data base.

*Acknowledgments.* We thank Richard Rapp for supplying  $1^\circ$  by  $1^\circ$  averages of the oceanic geoid and Brad Hager for helpful comments on an earlier version of this paper. This research was supported by the National Science Foundation under EAR 77-15198 and the National Aeronautics and Space Administration under NSG 5263.

#### REFERENCES

- Chapman, M. E., Geoid anomaly over mid-ocean ridges (abstract), *Eos Trans. AGU*, 58, 368, 1977.
- Chapman, M. E., and M. Talwani, Comparison of gravimetric geoids with Geos-3 altimetric geoid, *J. Geophys. Res.*, 84, 3803-3816, 1979.
- Cochran, J. R., and M. Talwani, Free-air gravity anomalies in the world's oceans and their relationship to residual elevation, *Geophys. J. R. Astron. Soc.*, 50, 495-552, 1977.
- Cochran, J. R., and M. Talwani, Gravity anomalies, regional elevation, and the deep structure of the North Atlantic, *J. Geophys. Res.*, 83, 4907-4924, 1978.
- Hager, B. H., Oceanic plate motions driven by lithospheric thickening and subducted slabs, *Nature*, 276, 156-159, 1978.
- Haxby, W. F., The mid-ocean ridge geoid anomaly (abstract), *Eos Trans. AGU*, 60, 391, 1979.
- Haxby, W. F., and D. L. Turcotte, On isostatic geoid anomalies, *J. Geophys. Res.*, 83, 5473-5478, 1978.
- Kaula, W. M., Tests and combination of satellite determinations of the gravity field with gravimetry, *J. Geophys. Res.*, 71, 5303-5314, 1966.
- Kaula, W. M., Global gravity and mantle convection, *Tectonophysics*, 13, 341-359, 1972.
- McAdoo, D. C., Interpretation of geoid anomalies in the vicinity of subduction zones (abstract), *Eos Trans. AGU*, 61, 370, 1980.
- Minster, J. B., and T. H. Jordan, Present-day plate motions, *J. Geophys. Res.*, 83, 5331-5354, 1978.
- Ockendon, J. R., and D. L. Turcotte, On the gravitational potential and field anomalies due to thin mass layers, *Geophys. J. R. Astron. Soc.*, 48, 479-492, 1977.

SANDWELL AND SCHUBERT: GEOID HEIGHT VERSUS AGE

- Parsons, B., and D. McKenzie, Mantle convection and the thermal structure of the plates, *J. Geophys. Res.*, *83*, 4485-4496, 1978.
- Parsons, B., and F. M. Richter, A relation between the driving force and geoid anomaly associated with mid-ocean ridges, *Earth Planet. Sci. Lett.*, in press, 1980.
- Parsons, B., and J. G. Sclater, An analysis of the variation of ocean floor bathymetry and heat flow with age, *J. Geophys. Res.*, *82*, 803-827, 1977.
- Pitman, W. C., R. L. Larson, and E. M. Herron, The age of the ocean basins, map, Geol. Soc. of Am., Inc., Boulder, Color., 1974.
- Rapp, R. H., Global anomaly and undulation recovery using Geos-3 altimeter data, *Tech. Rep. 285*, Ohio State Dep. of Geod. Sci., Columbus, 1979.
- Richter, F. M., and B. Parsons, On the interaction of two scales of convection in the mantle, *J. Geophys. Res.*, *80*, 2529-2541, 1975.
- Schubert, G., Subsolidus convection in the mantles of terrestrial planets, *Ann. Rev. Earth Planet. Sci.*, *7*, 289-342, 1979.
- Schubert, G., Self-driven motions of plates and descending slabs, in *Mechanisms of Plate Tectonics and Continental Drift*, edited by P. A. Davies and S. K. Runcorn, Academic, New York, 1980.
- Schubert, G., C. Froidevaux, and D. A. Yuen, Oceanic lithosphere and asthenosphere: Thermal and mechanical structure, *J. Geophys. Res.*, *81*, 3525-3540, 1976.
- Sclater, J. G., L. A. Lawver, and B. Parsons, Comparison of long-wavelength residual elevation and free air gravity anomalies in the North Atlantic and possible implications for the thickness of the lithospheric plate, *J. Geophys. Res.*, *80*, 1031-1052, 1975.
- Turcotte, D. L., and E. R. Oxburgh, Finite amplitude convection cells and continental drift, *J. Fluid Mech.*, *28*, 29-42, 1967.
- Watts, A. B., and M. Talwani, Gravity anomalies seaward of deep sea trenches and their tectonic implications, *Geophys. J. R. Astron. Soc.*, *36*, 57-90, 1974.

(Received March 3, 1980;  
revised June 11, 1980;  
accepted July 2, 1980.)

Appendix A. Derivation of the Geoid Height-Age Relation for  
the Plate Cooling Model

The temperature versus depth and age for a one-dimensional plate cooling model of the oceanic lithosphere is (McKenzie, 1967)

$$T(t, z') = T_o + (T_m - T_o) \left( z' + \frac{2}{\pi} \sum_{n=1}^{\infty} \frac{\sin(n\pi z')}{n} \exp(-n^2 ct) \right) \quad (\text{A-1})$$

where  $t$  is the lithospheric age,  $z'$  is the depth beneath the seafloor normalized by the lithospheric thickness  $\ell$ ,  $T_o$  is the surface temperature,  $T_m$  is the temperature at the base of the lithosphere, and

$$c = \frac{\pi^2 \kappa}{\ell^2} \quad (\text{A-2})$$

where  $\kappa$  is the thermal diffusivity. The subsidence of the seafloor away from the ridge crest, normalized by the lithospheric thickness, is (Parsons and Sclater, 1977)

$$D(t) = \frac{\alpha \rho_m (T_m - T_o)}{2(\rho_m - \rho_w)} \left( 1 - \frac{8}{\pi^2} \sum_{n=1}^{\infty} \frac{\exp(-(2n-1)^2 ct)}{(2n-1)^2} \right) \quad (\text{A-3})$$

where  $\alpha$  is the coefficient of thermal expansion and  $\rho_m$  is the mantle density.

Ockendon and Turcotte (1977) have shown that for isostatically compensated topography, with a characteristic wavelength that is much greater

than  $2\pi$  the depth of compensation, the geoid height is approximately

$$N(t) = \frac{-2\pi G}{g} \int_0^{\infty} \rho(t, z) z \, dz \quad (\text{A-4})$$

where  $G$  is the gravitational constant and  $g$  is the acceleration of gravity. It is not clear that this long wavelength approximation is valid for the plate cooling model. However, we will proceed with the derivation. In Chapter 3 we check the approximation by calculating the exact geoid height-age relation for the plate cooling model. From the exact calculation we demonstrate that the O-T approximation works remarkably well for this model.

As in the depth-age calculation, we assume that temperature and density are related linearly by the coefficient of thermal expansion as follows:

$$\rho(t, z') = \rho_m (1 + \alpha(T_m - T(t, z'))) \quad (\text{A-5})$$

Since we are interested in variations in geoid height we subtract the ridge crest density-depth function from the density structure at all ages

$$\rho(t, z) = \begin{cases} (\rho_w - \rho_m) & 0 < z < D(t) \\ \alpha \rho_m (T_m - T(t, z - D(t))) & D(t) < z < 1 + D(t) \end{cases} \quad (\text{A-6})$$

Inserting this density/depth function into (A-4) we find

$$N(t) = \frac{-2\pi G \ell^2}{g} \int_0^{D(t)} (\rho_w - \rho_m) z \, dz - \frac{2\pi G \ell^2}{g} \alpha \rho_m (T_m - T_o) \int_0^1 \left[ 1 - z' - \frac{2}{\pi} \sum_{n=1}^{\infty} \frac{\sin(n\pi z')}{n} \exp(-n^2 ct) \right] (z' + D(t)) \, dz' \quad (\text{A-7})$$

The second integral is evaluated by interchanging the order of summation and integration. The interchange is valid for all  $t > 0$ ; when  $t = 0$  the series is not uniformly convergent and  $N(0)$  is undefined. For greater ages the geoid height-age relation is

$$N(t) = \frac{-2\pi G \ell^2}{g} \left[ (\rho_m - \rho_w) \frac{D(t)^2}{2} + \alpha \rho_m (T_m - T_o) \left( \frac{1}{6} + \frac{2}{\pi^2} \sum_{n=1}^{\infty} \frac{(-1)^n}{n^2} \exp(-n^2 ct) \right) \right] \quad (\text{A-8})$$

CHAPTER 2  
FRACTURE ZONES

GEOID HEIGHT-AGE RELATION FROM SEASAT ALTIMETER PROFILES  
ACROSS THE MENDOCINO FRACTURE ZONE

David T. Sandwell and Gerald Schubert  
Department of Earth & Space Sciences  
University of California  
Los Angeles, CA 90024

September 21, 1981

## ABSTRACT

Twenty-eight Seasat altimeter profiles crossing the Mendocino Fracture Zone are used together with seafloor ages determined from magnetic lineations to estimate the change in oceanic geoid height with age, between ages of 15 and 135 Myr. An unbiased estimate of the overall geoid offset along each profile is determined from a least-squares fit of the along track derivative of the geoid to the geoid slope predicted from a simple two-layer gravitational edge effect model. Uncertainties based upon the statistical properties of each profile are also determined. A geoid slope-age relation is constructed by normalizing the geoid offsets and uncertainties by the age offsets. The results are in agreement with geoid slope-age relations determined from symmetrically spreading ridges (Sandwell and Schubert, 1980). However, the fracture zone estimates have smaller uncertainties and show less scatter. A comparison of these results with the geoid slope-age prediction of the boundary layer cooling model shows that the thermal structure begins to deviate from this model at an early age (20 to 40 Myr). A plate cooling model with a thickness of 125 km is most compatible with the geoid slope-age estimates although significant deviations occur; these may indicate that the lithospheric thermal structure is not entirely age dependent.



## INTRODUCTION

It is generally accepted that the oceanic lithosphere is the surface thermal boundary layer of a mantle convection system (Oxburgh and Turcotte, 1978). According to boundary layer theory (Turcotte and Oxburgh, 1967), the cooling and contraction of the oceanic lithosphere as it slides away from the ridge crest results in a surface heat flow which decreases with the age of the crust  $t$  as  $t^{-1/2}$  and a seafloor depth which increases with crustal age as  $t^{1/2}$ . Boundary layer theory correctly predicts the observed surface heat flow-age relation for seafloor as old as 110 Myr (Lister and Davis, 1976; Sclater and Parsons, 1976; Parsons and McKenzie, 1978). However, the observed depth-age relation begins to flatten from the  $t^{1/2}$  law for ages greater than about 70 Myr (Parsons and Sclater, 1977). This flattening in the average depth-age relation indicates a reduction in boundary layer thickening with age; theory predicts that the surface thermal boundary layer grows in thickness proportionately to  $t^{1/2}$ . Any mechanism which supplies heat to the base of the lithosphere can retard its rate of cooling and thickening with age. Shear heating in the asthenosphere (Schubert et al., 1976), small scale convection driven by boundary layer instability (Richter and Parsons, 1975), large scale upwelling due to internal heat sources (Jarvis and Peltier, 1980) and lithospheric thinning by hot spots (Heestand and Crough, 1981) are all possibilities. The cooling of a constant thickness plate (McKenzie, 1967) provides a mathematical model of limited boundary layer growth although it cannot discriminate among the physical processes that may be responsible for it.

Accurate measurements of the ocean geoid by the GEOS-3 and Seasat radar altimeters have provided a further constraint on the thermal structure of the cooling lithosphere. Boundary layer theory predicts that geoid height decreases

linearly with age with a slope of approximately  $-0.15 \text{ m Myr}^{-1}$  (Haxby and Turcotte, 1978). This linear decrease in geoid height with age, for ages up to 50 Myr, has been observed on GEOS-3 profiles crossing both the Southwest Indian Ridge (Chapman, 1977) and the Mid-Atlantic Ridge (Haxby and Turcotte, 1978; Haxby, 1979). For many spreading ridges, however, long wavelength geoid undulations that are unrelated to lithospheric cooling tend to mask the age-dependent geoid signal. Despite this difficulty, the signal can be recovered (albeit with some degree of uncertainty) from geoid height measurements over symmetrically spreading ridges or fracture zones with large age offsets. For symmetrically spreading ridges, the portion of the geoid that is related to the age of the lithosphere is symmetric in age about the ridge and invariant along isochrons. By using this a priori knowledge of the properties of the geoid signal associated with lithospheric cooling, Sandwell and Schubert (1980) have extracted geoid height-age relations from the observed geoid for large areas in the north Atlantic, south Atlantic, southeast Indian and Southeast Pacific oceans. Except for the southeast Pacific region the data are consistent with the linear decrease predicted by the thermal boundary layer cooling model for ages less than about 80 Myr. For greater ages, however, the observed geoid height-age relations suggested a reduction in the rate of boundary layer thickening with age. In fact, these data are also consistent with plate cooling models having thicknesses of about 125 km, as we show later.

An alternate method of extracting the geoid signal associated with lithosphere cooling is to measure the offset in geoid height across a fracture zone (Crough, 1979). Furthermore, if the age offset is known, a geoid height-age relation can be constructed. One advantage of this technique is that the change in geoid height across a fracture zone FZ occurs over a relatively short distance

(several hundred kilometers). Thus, the regional geoid undulations, which are dominant at wavelengths greater than a few thousand kilometers, can be distinguished from the shorter wavelength geoid step. Crough (1979) has estimated the geoid step across the Mendocino FZ using GEOS-3 altimeter data and has found that the step estimates are consistent with the thermal boundary layer model if the thermal diffusivity of the lithosphere is  $3.3 \times 10^{-7} \text{ m}^2 \text{ s}^{-1}$ . This value of diffusivity is, however, less than one-half the value needed to account for the observed depth-age relation. Crough (1979) suspected that systematic errors in the estimates of the geoid step may have biased his estimate of the diffusivity. Indeed, the geoid step observed in Seasat altimeter profiles crossing the younger portion of the Mendocino FZ are well matched by the gravitational edge effect model (Dorman, 1975) using the age-dependent thermal structure of the boundary layer cooling model with a more reasonable diffusivity of  $8 \times 10^{-7} \text{ m}^2 \text{ s}^{-1}$  (Sandwell et al., 1980). As pointed out by Detrick (1981), the systematic bias in the geoid step estimates made by Crough (1979) occurs because the actual geoid step is smooth (i.e. 90% of the step amplitude takes place over a distance of several hundred kilometers) while the fitting function that was used to estimate the step assumes that the entire step takes place over a distance of 200 km (Crough, 1979). By correcting for this bias in the step estimation procedure, Detrick (1981) has found that the age variation of the step in the geoid height across the Mendocino FZ is consistent with the prediction of the thermal boundary layer model for ages less than about 30 Myr. At greater ages (30 - 60 Myr) however, Detrick's (1981) geoid height step estimates are better explained by a plate cooling model with a 100 km thick lithosphere.

In this study we estimate the geoid height-age relation from Seasat

profiles crossing the Mendocino FZ for ages between 15 and 140 Myr. Rather than estimate the geoid height offset using the method described by Crough (1979), we use a fitting function that more closely approximates the observed smooth step-like variation in the geoid across the fracture zone. The advantages of this technique are that the estimate of the overall step in geoid height is unbiased and the uncertainties in the step estimate truly reflect geoid undulations that are unrelated to the thermo-gravitational edge effect. In the following sections we discuss the fitting procedure and the geoid height and age data. We then construct the geoid height-age relation and compare it with independently determined estimates (Sandwell and Schubert, 1980; Detrick, 1981). Finally, we discuss the implications of the derived geoid height-age relation for thermal models of the oceanic upper mantle.

#### THEORY FOR ESTIMATING THE GEOID STEP

The long wavelength, flat earth approximation (Ockendon and Turcotte, 1977) to the geoid of an isostatically compensated cooling lithosphere shows that geoid height depends only upon the age of the lithosphere. While this long wavelength approximation (i.e. the characteristic wavelength of horizontal density variations  $\gg 2\pi$  times the average depth of compensation) is valid for the rather smooth lateral changes in density associated with seafloor spreading, it should not be used to model the geoid step across the sharp age and density contrasts at a FZ. Because of the gravitational edge effect (Dorman, 1975), geoid height across a FZ is smooth and occurs over a characteristic distance of  $2\pi$  times the average compensation depth. Thus, the overall amplitude of the geoid step can only be determined from the differ-

ence between geoid heights far (i.e.  $\gg 300$  km) on either side of the FZ. In theory, this is a valid method of estimating the geoid offset. However, in practice this step measurement technique fails because the smooth FZ geoid signal is generally superimposed upon much larger amplitude geoid undulations that are unrelated to the FZ. This problem can be alleviated somewhat by measuring the geoid offset between two points closer to the FZ (e.g. 100 km on either side of the FZ), in which case the regional geoid will not have as large an effect upon the step estimate. However, only a portion of the step will then be measured. Thus, it is apparent that the entire geoid step cannot be observed in the presence of long wavelength noise (noise in this case is the part of the geoid that is unrelated to the FZ). It is only in the immediate vicinity of the FZ (i.e. within 100 km) that its geoid signal can be unambiguously identified. The overall amplitude of the geoid step must therefore be extrapolated from the small portion of the step that stands out from the regional geoid. This requires the introduction of a FZ model whose parameters are determined from a fit of the model geoid to the observed geoid in the vicinity of the FZ. An extrapolation of the model geoid to distances far from the FZ then provides an estimate of the overall geoid step.

To perform this extrapolation properly, the model must contain the basic characteristics of the FZ density structure. However, it must have only a few adjustable parameters and the geoid for the model must be easily evaluated so that it is useful as a fitting function. The simple two-layer model shown at the bottom of Figure 1 satisfies these requirements. It is derivable from the more physical model in the middle of the figure which shows two adjacent isostatically compensated quarter spaces with ages  $t_1$  and  $t_2$  and densities  $\rho(z, t_1)$  and  $\rho(z, t_2)$  ( $z$  is depth). Since we are concerned with the change in geoid height

Figure 1. Gravitational edge effect model used as a fitting function to estimate the overall geoid step. Top: smooth step in geoid height associated with two isostatically compensated quarter spaces;  $\Delta N$  is the geoid offset. Center: each quarter space has a density-depth relation that is age dependent. Bottom: the density contrast across the FZ is approximated by two semi-infinite mass sheets of mass per area  $\sigma$  and  $-\sigma$  at depths  $s$  and  $d$ , respectively.

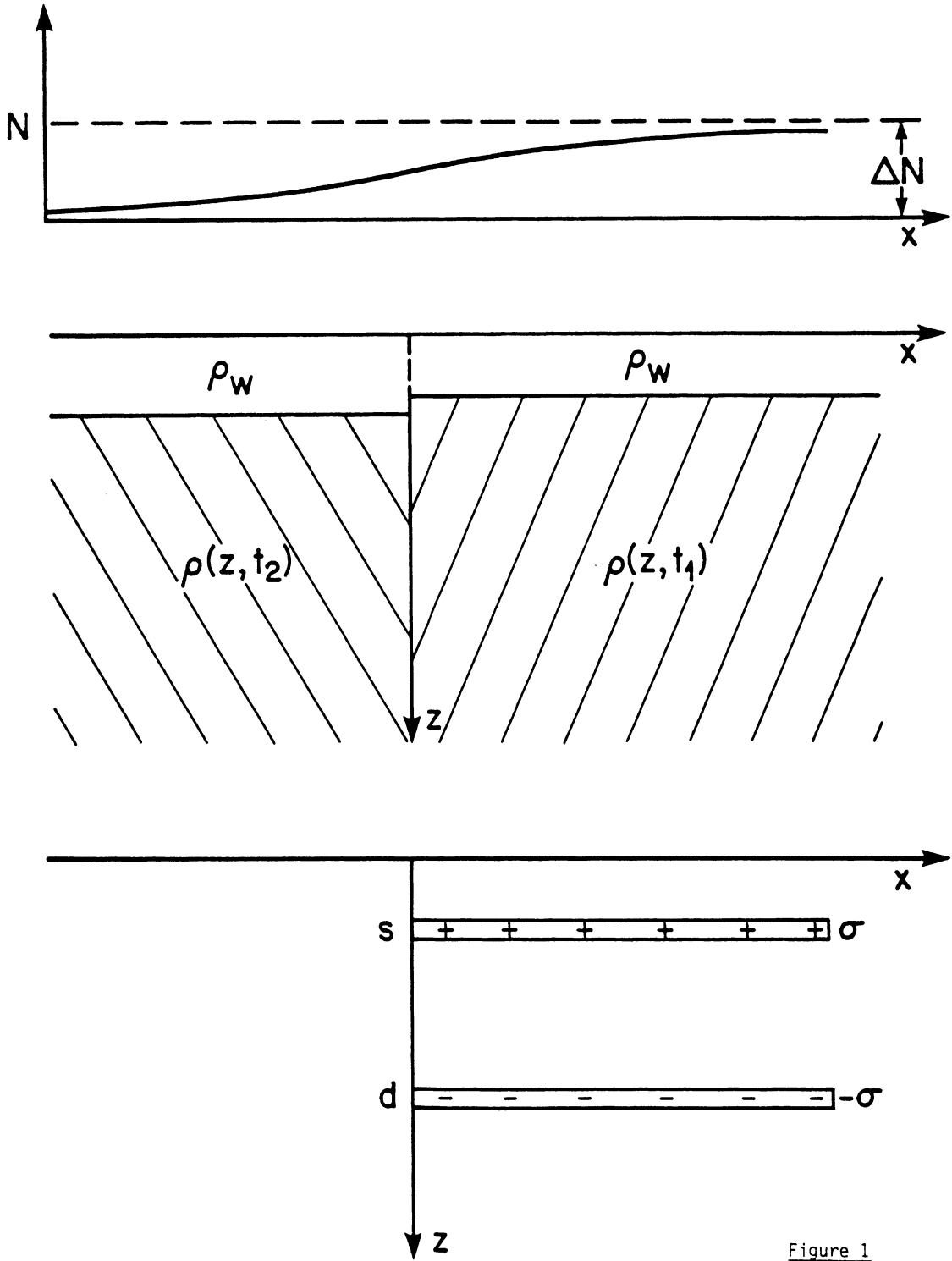


Figure 1

across the FZ we subtract the density on the left  $\rho(z, t_2)$  from the density on both sides. In this new configuration the density on the left side is zero; the largest density contrast on the right side occurs at the average seafloor depth  $s$  and is associated with the change in seafloor depth across the FZ. We approximate this horizontal density contrast by a thin sheet with mass per area  $\sigma$  at depth  $s$ . The total density contrast at greater depths is represented by a second mass sheet with mass per area  $-\sigma$  at the average compensation depth  $d$ . Clearly, this two-layer model does not represent the actual lateral density variations across a FZ since we have compressed the compensating mass into a single sheet and we have ignored the effects of lateral heat conduction (Louden and Forsyth, 1976; Detrick, 1981) and lithospheric flexure (Sandwell and Schubert, 1981). We will show, however, that good fits to the observed geoid steps can be obtained by varying the two parameters  $\sigma$  and  $d$ .

The geoid height  $N$  associated with this model is derived in the Appendix; it is given by

$$N(x) = \frac{2\pi G \sigma d}{g} \left\{ \frac{1}{2} \left(1 - \frac{s}{d}\right) + \frac{1}{\pi} \left(\arctan \frac{x}{d} - \frac{s}{d} \arctan \frac{x}{s}\right) + \frac{x}{2\pi d} \ln \left(\frac{x^2 + d^2}{x^2 + s^2}\right) \right\}, \quad (1)$$

where  $G$  is the universal gravitational constant,  $g$  is the gravitational acceleration, and  $x$  is the horizontal distance from the FZ. The overall geoid step  $\Delta N$  is derivable from (1) according to

$$\Delta N = \lim_{x \rightarrow \infty} N(x) = \frac{2\pi G \sigma}{g} (d - s). \quad (2)$$

We can rewrite (1) in terms of  $\Delta N$  as

$$N(x) = \Delta N \left[ \frac{1}{2} + \left(1 - \frac{s}{d}\right)^{-1} \left\{ \frac{1}{\pi} \left(\arctan \frac{x}{d} - \frac{s}{d} \arctan \frac{x}{s}\right) + \frac{x}{2\pi d} \ln \left(\frac{x^2 + d^2}{x^2 + s^2}\right) \right\} \right]. \quad (3)$$



The model contains only 2 adjustable parameters,  $\Delta N$  and  $d$ , because the average seafloor depth  $s$  is known.

We will show in the next section that it is preferable to fit the model to the along-track derivative of the observed geoid rather than to the geoid itself because the power spectrum of the geoid slope is nearly white and Gaussian statistics can be used. The geoid slope is

$$\frac{dN}{dx} = \frac{\Delta N}{2\pi(d-s)} \ln \left( \frac{x^2 + d^2}{x^2 + s^2} \right) \quad (4)$$

The form of (4) reveals the role of each of the model parameters. An increase in compensation depth  $d$  produces both a broadening in the geoid slope profile and a decrease in its amplitude in such a way that the total area (i.e. the geoid offset) under the geoid slope profile is  $\Delta N$ . The model is linear in the parameter  $\Delta N$ , and by design this parameter defines the total geoid offset. In the next section we present the data and use (4) to estimate the geoid offsets for Seasat altimeter profiles crossing the Mendocino FZ at many locations.

## DATA

### Location of the Mendocino FZ

The Mendocino FZ in the northeast Pacific was chosen for this geoid-age study because of its great horizontal extent and large age offset. As shown in Figure 2, the Mendocino FZ runs continuously from the west coast of North America at  $40^{\circ}\text{N}$  to well beyond the Hawaiian-Emperor seamount chain at its western extreme. At  $220^{\circ}\text{E}$  it branches into northern and southern extensions. East of  $210^{\circ}\text{E}$  the location of the FZ is defined by the bathymetric

Figure 2. Location map of the Mendocino FZ. The dashed lines separating regions A, B, and C indicate portions of the FZ that are not readily apparent on bathymetric charts. Seafloor ages on the northern side of the Mendocino FZ increase continuously from 0 Myr at  $\sim 230^{\circ}\text{E}$  to 140 Myr at  $165^{\circ}\text{E}$ . Tracks of 28 Seasat altimeter orbits are labelled by their orbital revolution number and direction, A-ascending, D-descending.

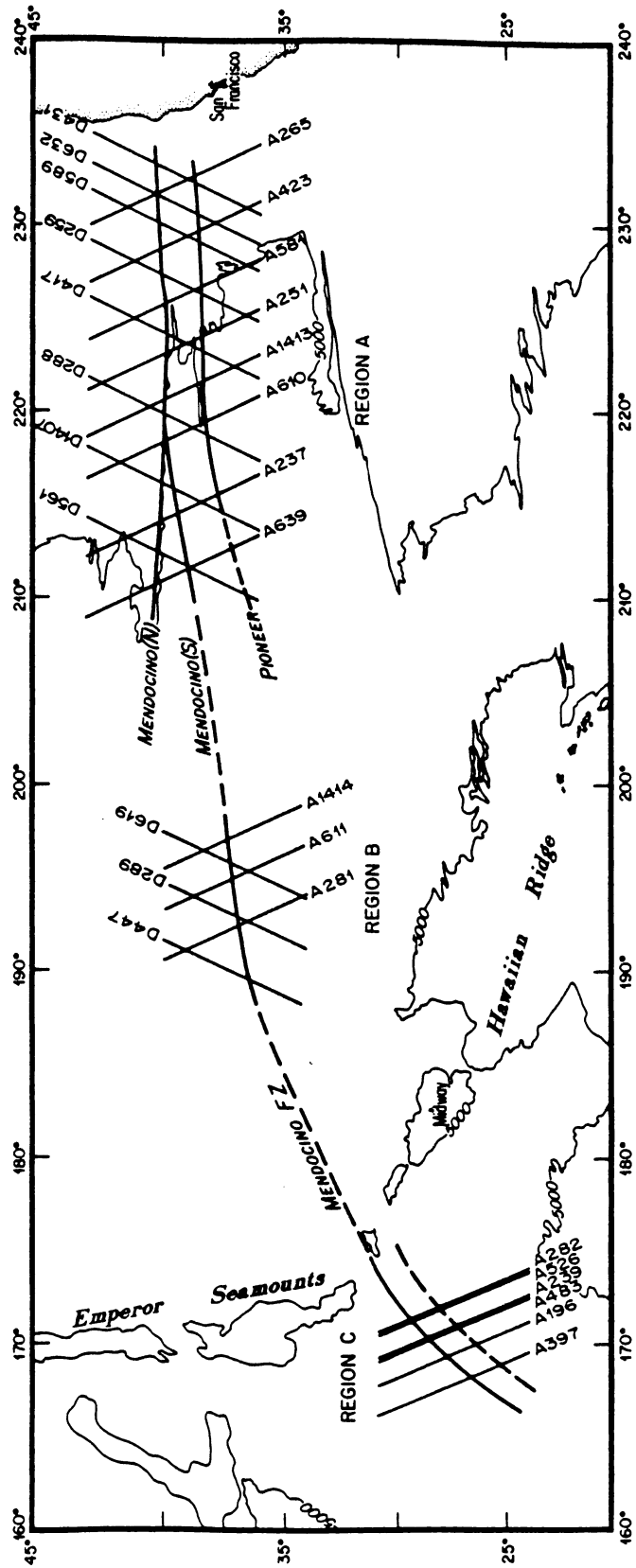


Figure 2

scarp on the chart "Bathymetry of the Northeast Pacific" by Mammerickx and Smith (1981). Between  $200^{\circ}\text{E}$  and  $210^{\circ}\text{E}$  the Mendocino FZ appears quite diffuse, i.e. many parallel scarps exist, as indicated by the dashed line in Figure 2 (Chase et al., 1971). However, a single scarp which we believe is the western extension of the Mendocino south reappears to the west of  $200^{\circ}\text{E}$  (Region B of Figure 2). To the west of Region B the FZ is again diffuse and sometimes absent in the bathymetric contours. Along this section it is crosscut by the Hawaiian Swell and the Hawaiian-Emperor Seamount chain. The westernmost segment of the Mendocino FZ is observed in bathymetric contours lying southwest of Midway Island (Figure 3 of Mammerickx, 1981). The Pioneer FZ, with a somewhat smaller age offset, lies approximately 150 km to the south of the younger portion of the Mendocino FZ (Region A).

#### Age Offset along the Mendocino FZ

The age of the Mendocino FZ varies from 0 Myr at its eastern extreme, where it intersects the Juan de Fuca ridge, to over 130 Myr at a longitude of  $170^{\circ}\text{E}$ . Magnetic anomalies have been identified in Region A of Figure 2 by Atwater and Menard (1970). We have used the time scale of Ness et al. (1980) to date these anomalies and to determine the age offset of the Mendocino FZ as a function of longitude between  $210^{\circ}\text{E}$  and  $230^{\circ}\text{E}$ . Similarly, the Mesozoic magnetic anomalies that have been identified (Hayes and Pitman, 1970) and dated (Larson and Chase, 1972; Larson and Pitman, 1972) in Region C were used to calculate age offset versus longitude along the westernmost portion of the Mendocino FZ. The results are shown by the solid portions of the curve in Figure 3. The age offsets in region B, however, are not well established. We have used the plate reconstruction model of Larson and Chase (1972) to infer the longitude dependence of the age offset shown by the dashed curve between

180°E and 210°E in Figure 3. Essentially, age offset increases continuously from 11 Myr at 180°E to 26 Myr at 210°E. The age offset curve in Figure 3 is used in the next section, together with estimates of the overall geoid step, to determine the change in geoid height with age.

#### Geoid Height Profiles across the Mendocino FZ

The locations of 28 Seasat altimeter profiles that were used to estimate geoid offsets along the Mendocino FZ are shown in Figure 2. We have not used the Seasat profiles that pass over the more diffuse segments of the FZ (dashed lines on Figure 2) because our model assumes that the age and density offsets across the FZ occur at a sharp boundary. The geoid height, which is well approximated by the sea surface height, is shown in Figures 4(a) and (b) for the 11 ascending orbits and 11 descending orbits in regions A and B. In each case the steepest portion of the smooth step in the geoid coincides with the location of the Mendocino FZ. The smaller step at approximately 38.5°N corresponds to the Pioneer FZ. The geoid step associated with the Mendocino FZ in region C is not readily apparent, however, in the geoid profiles shown in Figure 5 (the location of the Mendocino FZ is marked by an arrow on each of the profiles). To enhance the FZ geoid signal with respect to the noise, we have shifted four of these profiles (A239, A483, A196, and A397) so that they line up at the FZ and have made a composite geoid profile by averaging their geoid slopes and integrating the stacked geoid slope profile. This stacked profile, plus a constant, is the uppermost profile in Figure 5. The nearly coincident profiles A282 and A526 were not used to compute the composite geoid profile since a large seamount at 29.5°N, 173.5°E dominates the FZ geoid signal.

Figure 3. Age offsets across the Mendocino FZ versus longitude. The age offsets along the solid portions of the curve were determined from dated seafloor magnetic lineations. Along the dashed part of the curve age offsets are derived from a plate reconstruction model.

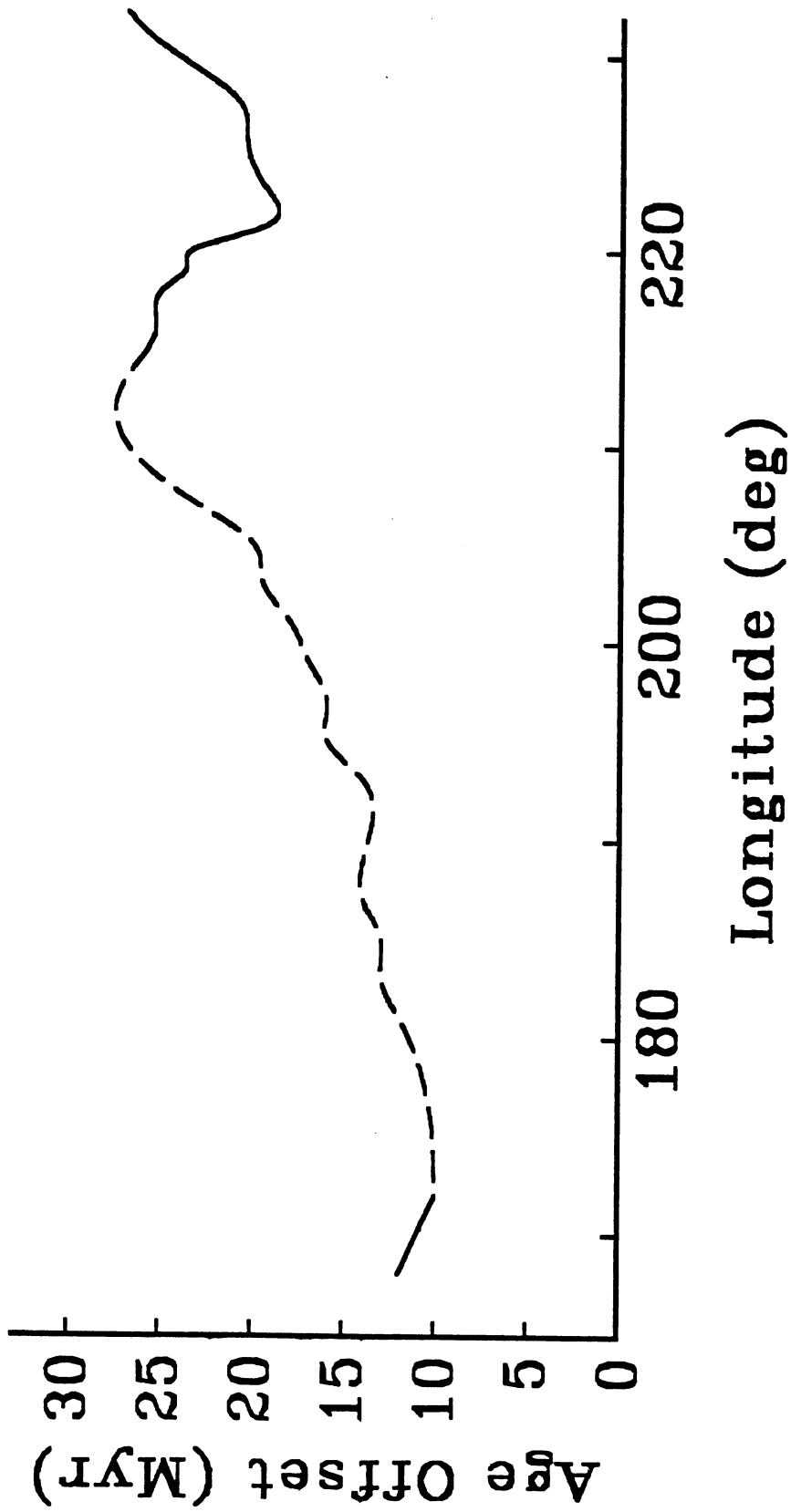


Figure 3

Figure 4. Relative geoid heights along the orbital tracks of Regions A and B for ascending orbits (a) and descending orbits (b). A smooth step in the geoid height occurs at the Mendocino FZ.

Figure 5. Relative geoid height profiles from Region C. The location of the Mendocino FZ, determined from bathymetric contours (Mammerickx, 1981), is marked by an arrow on each profile. The FZ geoid step is not readily apparent on these profiles. To enhance the FZ geoid signal the profiles A239, A483, A196, and A397 were aligned at the arrows and stacked to yield the profile shown at the top. Profiles A526 and A282 were not used because of the seamount near the FZ.



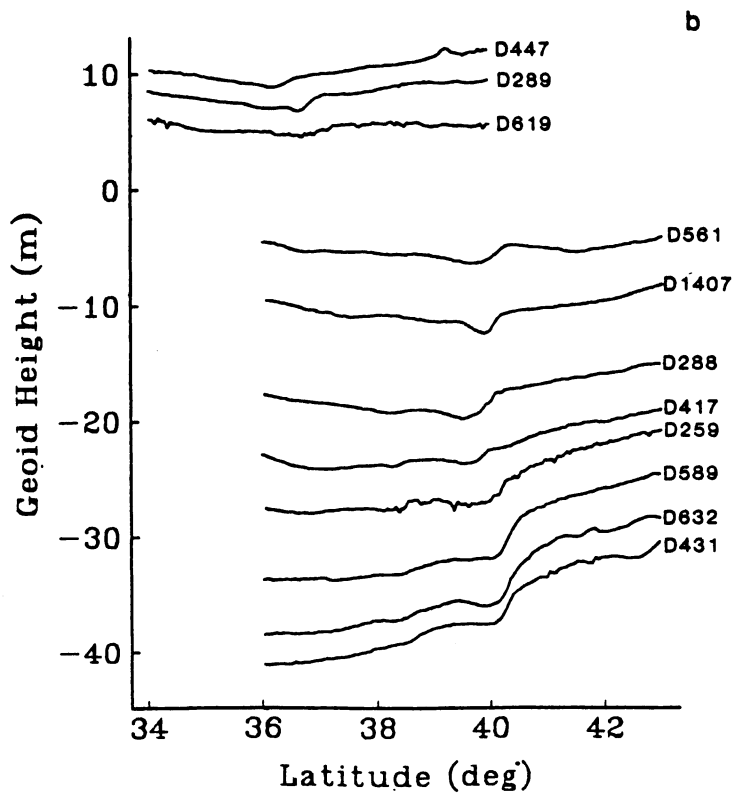
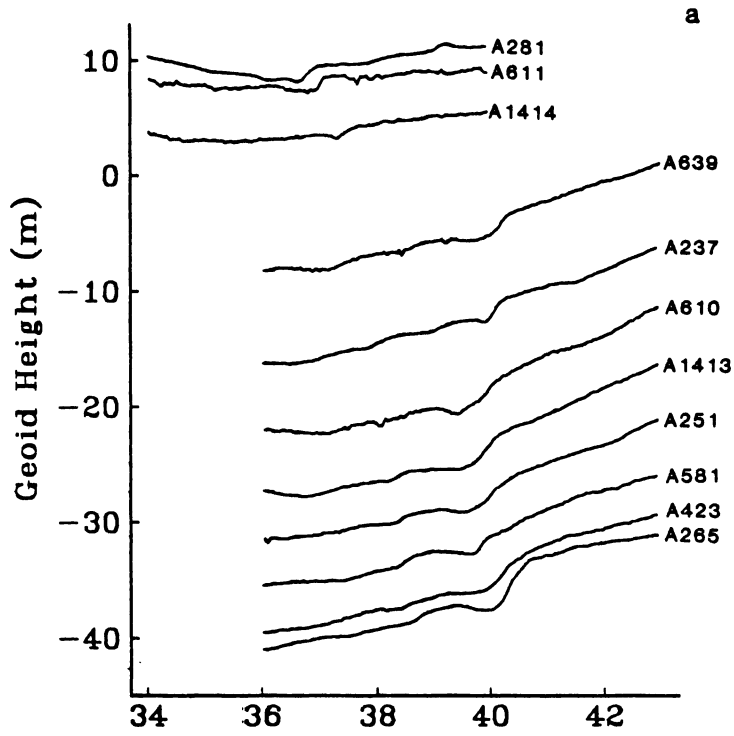


Figure 4

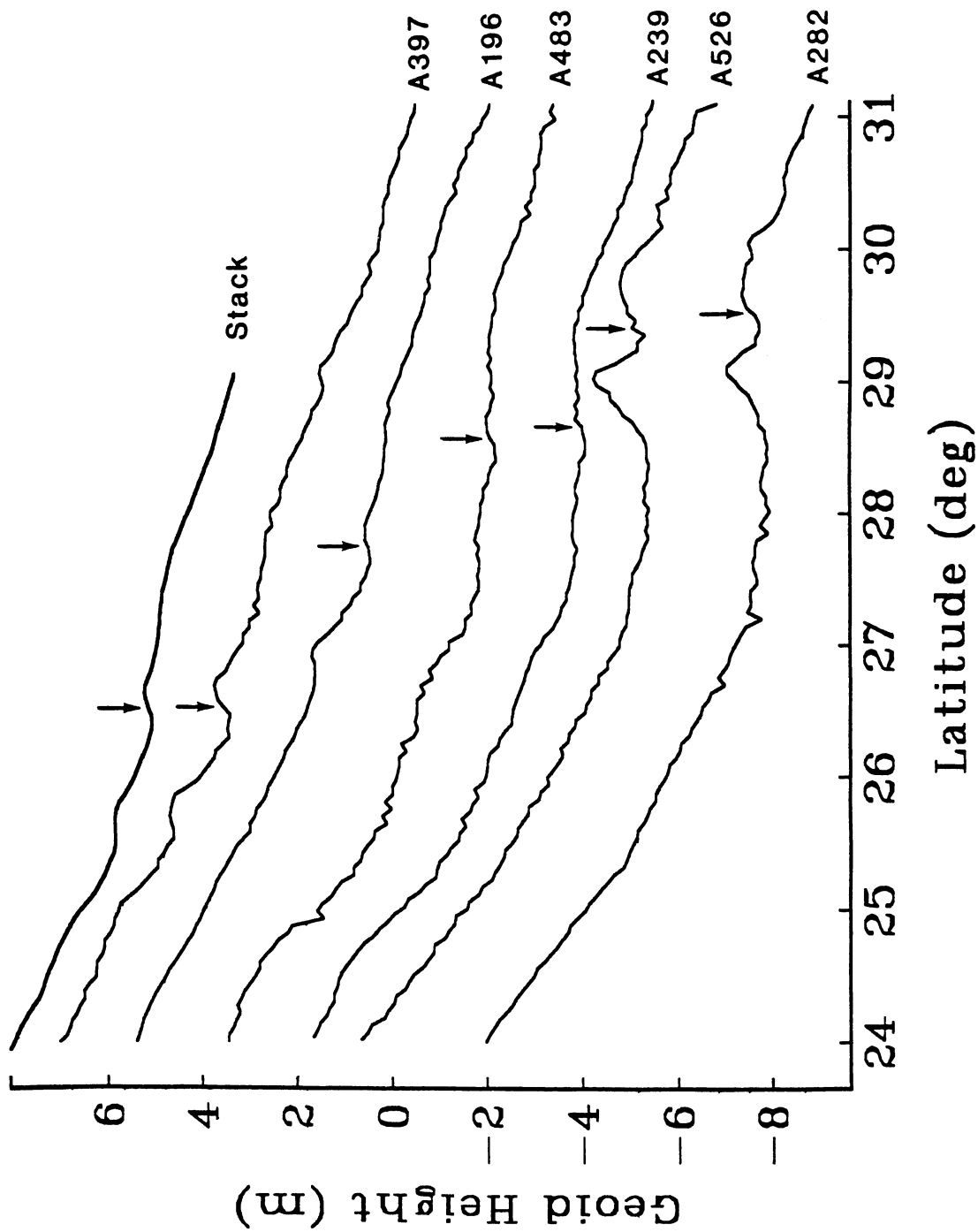


Figure 5

## RESULTS

It is apparent from the profiles shown in Figures 4 and 5 that the smooth step associated with the Mendocino FZ is superimposed upon both longer wavelength regional geoid undulations and shorter wavelength geoid variations (noise). The regional geoid can be modelled by a second order polynomial (Crough, 1979), but the shorter wavelength noise cannot be directly separated from the FZ geoid signal. Instead, the best estimate of the overall geoid offset is found by varying the model parameters  $\Delta N$  and  $d$  and the parameters of the quadratic fit to the regional geoid until the rms of the residuals between the model and the data is minimized. This least squares fitting procedure requires that the residuals have a Gaussian distribution or, alternatively, that the power spectrum of the residuals is white. However, after fitting a geoid profile using this procedure we found that the power spectrum of the residuals was red, i.e. it decreased with increasing wavenumber  $k$  according to  $k^{-2}$ . We therefore pre-whitened the noise spectrum by taking the along-track derivative of the geoid profile (an example is given in Figure 6). This technique not only whitens the noise spectrum but it also has other advantages. First, the derivative of the regional geoid representation has one less parameter. Second, the FZ geoid signal dominates the geoid slope whereas it is a minor component of the geoid. Thus, more emphasis is placed upon minimizing the residuals in the vicinity (within 100 km) of the FZ rather than those far from the FZ. Finally, the peak in the geoid slope clearly delineates the FZ and can be used to locate it in areas where bathymetric data are unavailable.

The overall geoid offset for each of the profiles was estimated by minimizing the sum of the squares of the differences between the observed geoid slope and the model geoid slope

Figure 6. Power spectrum of the along track derivative of the geoid profile A423 (solid curve). The dashed curve represents the power spectrum after the best fitting model was removed. This spectrum is nearly "white" for wavenumbers less than the corner wavenumber marked by the arrow at  $2.6 \times 10^{-4} \text{ m}^{-1}$ . The spectra were smoothed for presentation.

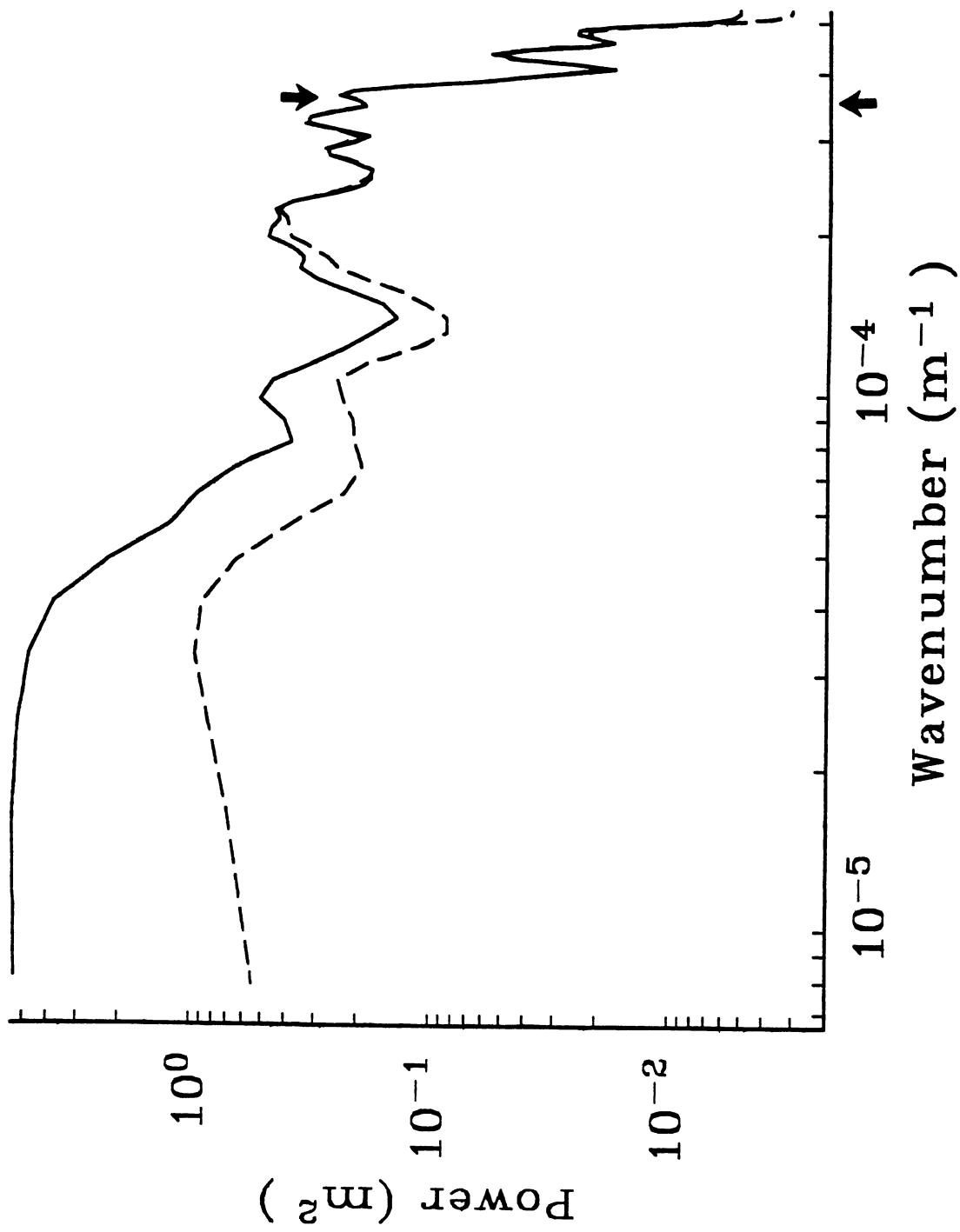


Figure 6

$$\frac{dN}{dx} = ax + b + \frac{\Delta N}{2\pi(d-s)} \ln \left( \frac{(x - x_0)^2 + d^2}{(x - x_0)^2 + s^2} \right) \quad , \quad (5)$$

where  $a$  and  $b$  specify the slope and intercept of the derivative of the regional geoid and  $x_0$  is the location of the FZ. We included an additional term for the profiles in region A to account for the effect of the geoid step at the Pioneer FZ on the Mendocino FZ geoid signal. The parameter estimation problem is linear in all of the model parameters except for  $x_0$  and  $d$ . The best set of model parameters was determined by using an iterative nonlinear technique due to Marquardt (1963). In general, the algorithm required two iterations to converge and the final set of model parameters was insensitive to the starting model. However, profiles A251 and D417, which pass over the same part of the Mendocino FZ, and individual profiles in Region C required special attention. For profiles A251 and D417 satisfactory results, i.e. non-negative compensation depths  $d$ , were obtained by choosing a different starting model. Problems arose in fitting the model to the individual profiles in Region C because the FZ geoid signal is smaller than the noise. The signal was boosted to roughly twice the noise level by stacking four of the geoid profiles, as described earlier.

An uncertainty estimate for each of the model parameters was calculated from a linear approximation to the model in the neighborhood of the best set of model parameters. The uncertainty estimate is highly dependent upon the number of degrees of freedom in the geoid slope profile. For a white noise spectrum that has a corner wavenumber (i.e. the power spectrum falls rapidly at higher wavenumbers) of  $k_{\text{cor}} = \frac{2\pi}{\lambda_{\text{cor}}}$ , the number of degrees of freedom is

$$(n - p) \lambda_{\text{min}} / \lambda_{\text{cor}} \quad ,$$

where  $n$  is the number of data points in the profile,  $p$  is the number of model parameters, and  $\lambda_{\min}$  is twice the distance between data points. Figure 6 shows the power spectrum of the geoid slope (solid line) and the residual geoid slope (dashed line) for profile A423. The residual power spectrum is nearly white for wavenumbers between  $8 \times 10^{-6} \text{ m}^{-1}$  and  $3 \times 10^{-4} \text{ m}^{-1}$ . At higher wavenumbers the power declines rapidly. This corner wavenumber is shown by an arrow in Figure 6;  $\lambda_{\text{COR}}$  has a value of 21 km.

Examples of model fits to observed geoid profiles from regions A, B, and C and their associated residuals are shown in Figure 7. In every case the model (5) was fit to the along-track derivative of the profile. The fit to the geoid height was obtained by integrating the model. In general, the rms of the residual geoid is less than 0.5 m. Twenty out of 22 profiles from regions A and B have a geoid slope with a component which is antisymmetric about the Mendocino FZ. For ascending orbits the geoid slope is depressed on the older side of the FZ. Similarly, the descending orbits show elevated geoid slopes on the older side. This antisymmetric component cannot be fit by (5) because the gravitational edge effect predicts a geoid slope that is symmetric about the FZ. The asymmetry may be a result of flexure at the FZ caused by the difference in subsidence rates on either side of the FZ together with the difference in age-dependent flexural rigidities across the FZ (Sandwell and Schubert, 1981).

A complete summary of the estimated geoid offsets and their uncertainties, the age offsets  $\Delta t$ , the average ages  $t_{\text{ave}}$ , and the changes in geoid height divided by the associated age offsets is given in Table 1. The estimates of the overall geoid offset  $\Delta N$  divided by the age offset  $\Delta t$ , and associated uncertainties, are plotted against the average age of the two lithospheric segments

Figure 7. Best fitting models to profiles from Region A (D589), Region B(D619), and Region C (stacked profile) are shown in the upper, middle and lower rows, respectively. The parameters of the model (5) were varied in a least squares fit to the along track derivative of the geoid shown in the left column (filtered for presentation with a 16 km half-width Gaussian filter). The integral of the model, plus a constant, and the observed geoid profile are shown in the center column. The residual geoid height is plotted on the right and has typical values of  $\pm 0.3$  m.



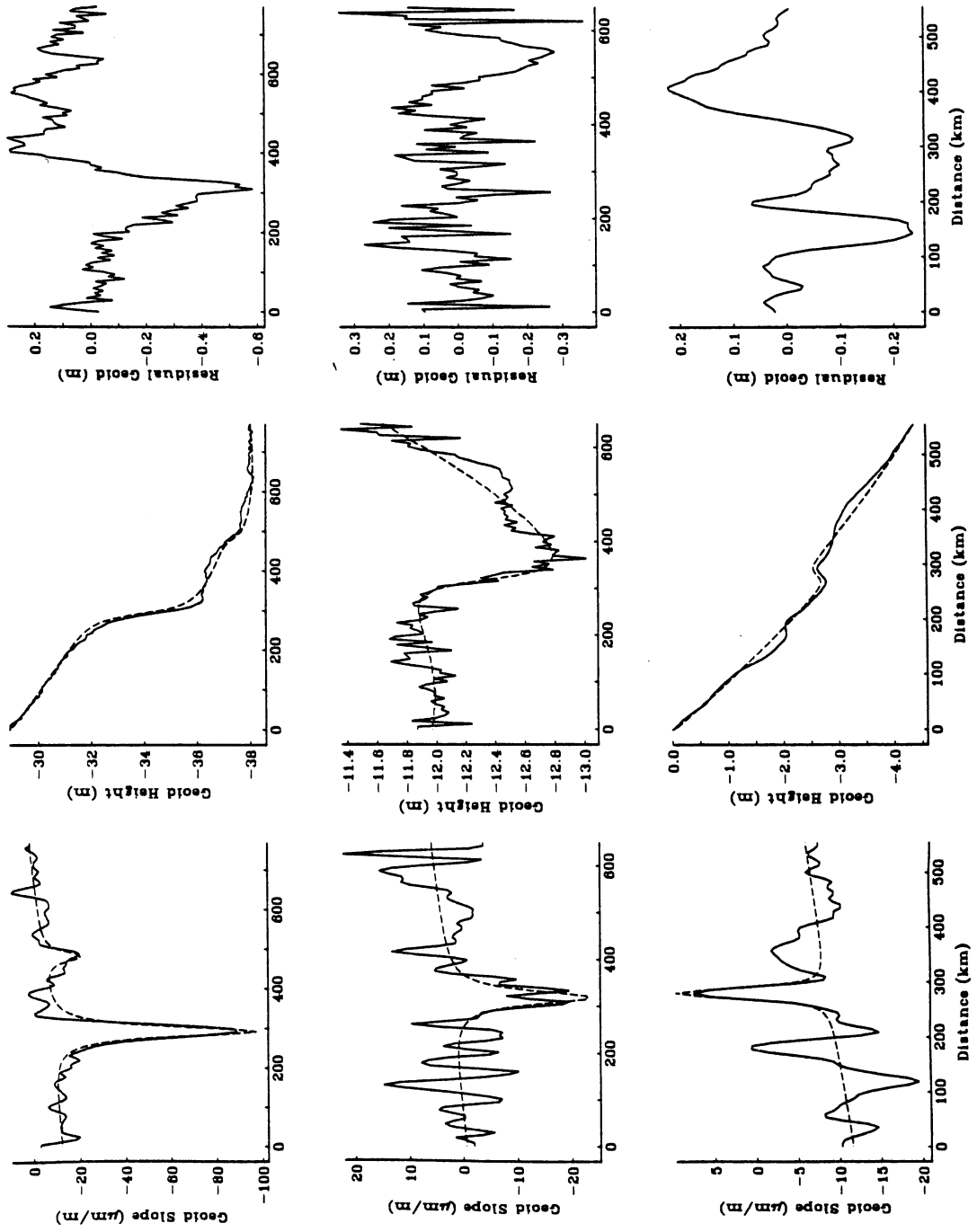


Figure 7

TABLE 1. Age, Age Offset, Geoid Offset and Change in Geoid Height With Age Offset for Profiles Crossing the Mendocino FZ.

Orbit #	$t_{ave}$ Myr	$\Delta t$ Myr	$\Delta N \pm \sigma_{\Delta N}$ m	$\Delta N/\Delta t \pm \sigma_{\Delta N/\Delta t}$ m
<u>Region A</u>				
A265	15.6	-26.9	4.84 $\pm$ 0.86	-0.179 $\pm$ 0.032
D431*	16.0	22.0	-3.28 $\pm$ 0.68	-0.149 $\pm$ 0.031
D632	16.1	26.8	-5.13 $\pm$ 1.16	-0.191 $\pm$ 0.051
D589	19.3	24.3	-4.53 $\pm$ 0.52	-0.186 $\pm$ 0.025
A423	22.4	-22.5	3.44 $\pm$ 0.75	-0.155 $\pm$ 0.034
D259	27.4	21.7	-3.44 $\pm$ 1.10	-0.158 $\pm$ 0.060
A581	29.0	-20.5	2.82 $\pm$ 2.10	-0.138 $\pm$ 0.101
D417	32.0	20.0	-2.44 $\pm$ 1.23	-0.122 $\pm$ 0.063
A251	34.2	-19.2	2.33 $\pm$ 0.73	-0.114 $\pm$ 0.042
A1413	39.1	-22.6	2.92 $\pm$ 0.78	-0.129 $\pm$ 0.041
D288	40.6	23.5	-3.36 $\pm$ 0.66	-0.143 $\pm$ 0.033
A610	43.0	-24.8	3.07 $\pm$ 1.03	-0.124 $\pm$ 0.049
D1407	46.3	25.4	-1.84 $\pm$ 0.30	-0.072 $\pm$ 0.014
A237	50.0	-26.4	2.19 $\pm$ 0.57	-0.083 $\pm$ 0.022
D561	55.0	26.0	-1.92 $\pm$ 0.59	-0.074 $\pm$ 0.023
A639	60.3	25.4	2.18 $\pm$ 0.49	-0.086 $\pm$ 0.023
<u>Region B</u>				
A1414	84.0	-16.0	1.12 $\pm$ 0.469	-0.070 $\pm$ 0.035
D619	85.4	16.0	-1.51 $\pm$ 0.383	-0.094 $\pm$ 0.028
A611	86.0	-16.0	1.12 $\pm$ 0.409	-0.070 $\pm$ 0.030
D289	88.2	14.0	-1.15 $\pm$ 0.429	-0.082 $\pm$ 0.037
A281	88.8	-13.8	1.61 $\pm$ 0.456	-0.117 $\pm$ 0.033
D447	91.7	13.5	-1.51 $\pm$ 0.303	-0.112 $\pm$ 0.022
<u>Region C</u>				
A239+A483 +A196+A397	133.3	-11.3	0.59 $\pm$ 0.362	-0.052 $\pm$ 0.032

\* This profile intersects the Mendocino FZ to the east of the Juan de Fuca spreading ridge and therefore it has a smaller offset than adjacent profiles.

in Figure 8. For ages less than about 20 Myr, the geoid slope is slightly greater than  $-0.15 \text{ m Myr}^{-1}$  while for greater ages it is between  $-0.05$  and  $-0.10 \text{ m Myr}^{-1}$ . In the next section we compare this geoid slope - age relation with independently determined estimates. We then discuss all of the data in terms of lithospheric cooling models.

## DISCUSSION

The overall geoid steps for 18 Seasat altimeter profiles crossing the Mendocino FZ have recently been estimated by Detrick (1981). Many of the profiles used in his study either intersect the profiles we have chosen or are identical to ours. However, different methods were used in the two studies to estimate the geoid step. To compare our results with Detrick's (1981), we have corrected his estimates for the bias introduced by his measurement procedure (using his bias model, Figure 8 of Detrick, 1981) and averaged his estimates over 10 Myr time intervals. We have also averaged our estimates, weighted by their uncertainties, over the same 10 Myr age intervals. Both sets of results are shown in Figure 9, where the asterisks represent Detrick's estimates and the octagons represent our points. The agreement is quite good, considering that more than half of our profiles were taken from different orbits than Detrick's. The major difference between the two studies lies in the data selection at ages greater than 60 Myr. We did not use the profiles crossing the Mendocino FZ between ages of 60 Myr and 80 Myr since this portion of the FZ is not clearly delineated in the bathymetric contours (Chase et al., 1971). In addition, we have estimated  $\Delta N/\Delta t$  at 88 Myr and 135 Myr although the formal uncertainty in the 88 Myr estimate

Figure 8. Geoid slope estimates and uncertainties for profiles shown in Figures 4 and 5 determined by normalizing the geoid offsets by the age offsets. These are plotted against the average age across the FZ. Octagons (ascending orbits), asterisks (descending orbits).

Figure 9. Geoid slope - age estimates averaged over 10 Myr age intervals for the Mendocino FZ, the North Atlantic south of  $32^{\circ}\text{N}$ , and the South Atlantic. The estimates for the Southeast Indian Ocean were averaged over 5 Myr age intervals (octagons). Asterisks represent Mendocino FZ geoid slope - age estimates from Detrick (1981). Symmetric spreading ridge data are from Sandwell and Schubert (1980). Also shown are geoid slope - age relations predicted by plate cooling models with plate thicknesses of 100 km (dotted curve), 125 km (solid curve), and 200 km (dashed curve).

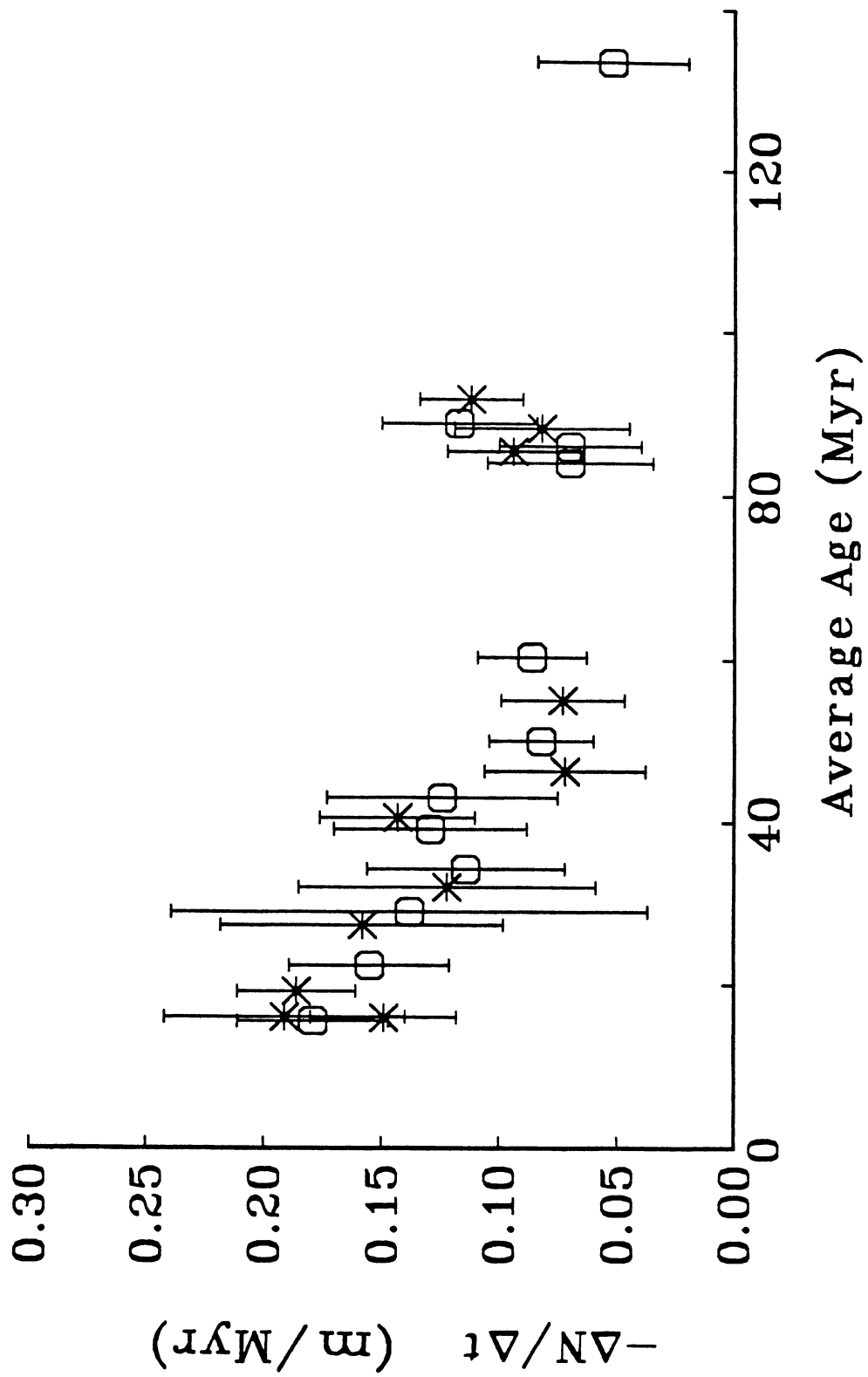


Figure 8

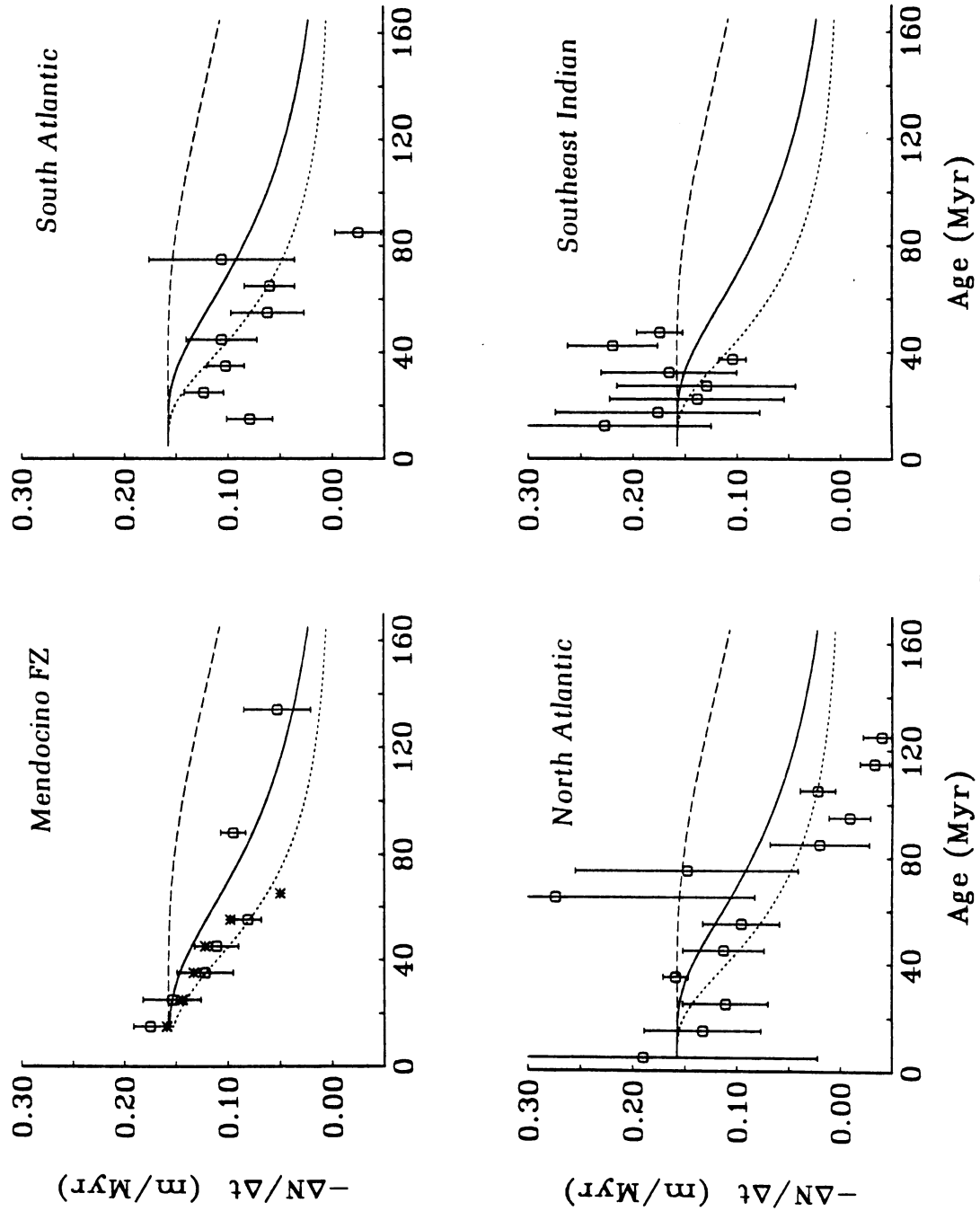


Figure 9

may not reflect the actual uncertainty because the age offset in this region is only poorly constrained. The good agreement between the two data sets at young ages lends additional support to the validity of our estimates at 88 and 135 Myr even though these two points do not lie along the general trend of the other points.

Further comparisons can be made with the estimated geoid slope - age relations for symmetrically spreading ridges (Sandwell and Schubert, 1980). Figure 9 also shows estimates and uncertainties of the geoid slope for the North Atlantic south of 32°N, the South Atlantic, and the Southeast Indian Ocean areas (Sandwell and Schubert, 1980). In general, our estimates from these three oceanic areas are consistent with the FZ estimates; however, the FZ data have smaller uncertainties and show less scatter. These smaller uncertainties allow us to discriminate among the various lithospheric cooling models. The boundary layer cooling model predicts that the geoid slope remains constant for all ages; a value of  $-0.15 \text{ m Myr}^{-1}$  has been estimated by Haxby and Turcotte (1978). The results from the symmetrically spreading ridges are consistent with a constant geoid slope for ages less than 80 Myr. The more accurate FZ geoid slope estimates, however, are consistent with the boundary layer model only for ages less than about 40 Myr. Figure 9 also shows geoid slope - age relations for plate cooling models (Sandwell and Schubert, 1980; Parsons and Richter, 1980). The values of the thermal parameters used in these model calculations are from the best-fitting plate model of the depth-age relation in the North Pacific (Parsons and Sclater, 1977): thermal expansion coefficient =  $3.3 \times 10^{-5} \text{ K}^{-1}$ , temperature contrast across the plate = 1330 K, thermal diffusivity =  $8 \times 10^{-7} \text{ m}^2 \text{ s}^{-1}$ . Theoretical geoid slope-age relations for plate thicknesses of 200 km (dashed curves), 125 km (solid curves), and 100 km (dotted curves) illustrate

the sensitivity of the relation to this parameter. Values of plate thickness between about 100 and 125 km are most consistent with all of the geoid slope estimates. Because the uncertainties in the geoid slope estimates for the symmetrically spreading ridges are relatively large, these data are also consistent with a plate thickness of 200 km, which gives a flattening in the geoid height - age relation at 80 Myr. However, this value of plate thickness is incompatible with the FZ geoid slope estimates.

The geoid slope - age relation is much more sensitive to the thickness of the lithosphere than are the depth-age and heat flow-age relations. To demonstrate this, the heat flow-age relation for well sedimented seafloor throughout the oceans (Sclater et al., 1980), the depth-age relation for the North Atlantic south of 35°N (Parsons and Sclater, 1977), and the depth-age relation for the North Pacific (Sclater et al., 1971; Parsons and Sclater, 1977) are shown in Figure 10 together with the predictions of the plate cooling models using the same parameter values as in Figure 9. The heat flow-age relation is notably insensitive to the lithospheric thickness while the depth-age relation is moderately sensitive to this parameter. In contrast, the geoid slope-age relation changes by more than an order of magnitude at 160 Myr when the lithospheric thickness is changed from 100 km to 200 km. Thus, small changes in the thermal structure near the base of the lithosphere produce large changes in the geoid slope for ages greater than about 40 Myr.

A better understanding of the enhanced sensitivity of the geoid slope to thermal perturbations in the lower portion of the lithosphere comes directly from the long wavelength, flat-earth approximation to the geoid height for isostatically compensated topography (Ockendon and Turcotte, 1977)

$$N(x) = \frac{-2\pi G}{g} \int_0^{\infty} \rho(x,z) z dz \quad . \quad (6)$$



Figure 10. Heat flow-age relation (top) for well sedimented seafloor throughout the oceans (Sclater et al., 1980) and depth-age relations for the North Atlantic (middle) and the North Pacific (bottom) (Sclater et al., 1971; Parsons and Sclater, 1977). Curves are predictions of the plate cooling model for plate thicknesses of 100 km (dotted), 125 km (solid) and 200 km (dashed).

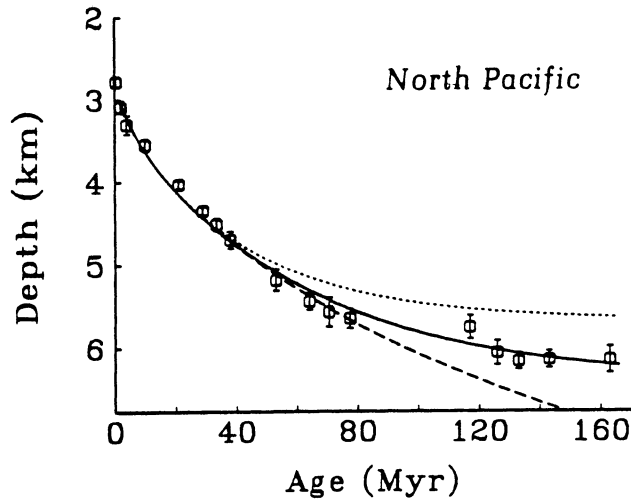
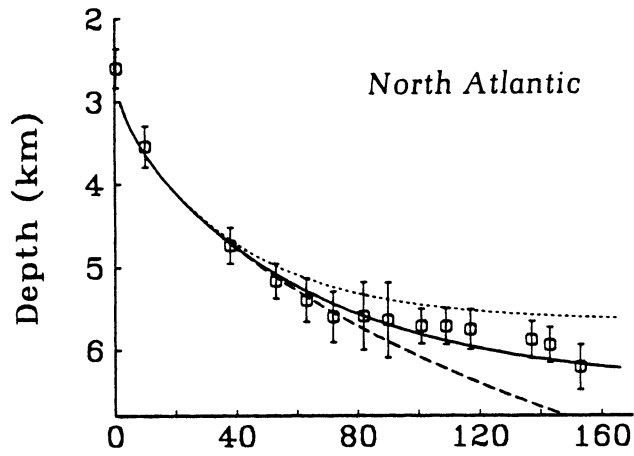
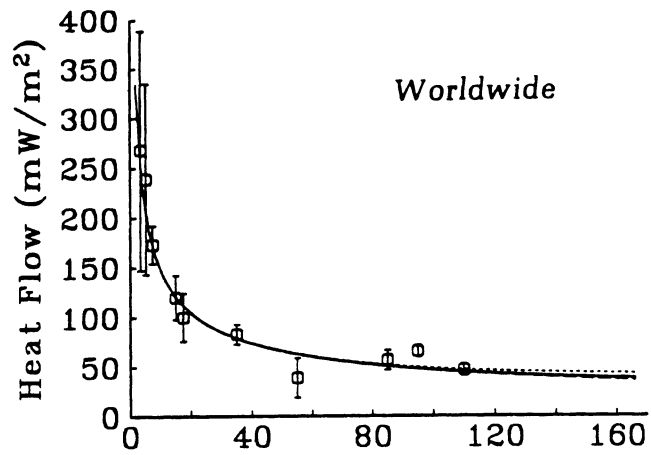


Figure 10

Seafloor depth is proportional to

$$\int_0^{\infty} \rho(x,z) dz$$

It is apparent from these equations that density variations at depth have more effect upon the geoid than the seafloor elevation simply because of the weighting function  $z$  in the integrand.

Based upon the data and models presented in Figures 9 and 10 we believe that the average lithospheric thermal structure is best approximated by a plate cooling model with a 125 km thick plate. A plate model with 100 km thickness does not fit the geoid slope - age estimates from the Mendocino FZ at 88 and 135 Myr, and it also does not fit the North Pacific depth-age data for ages greater than 40 Myr. A thick plate model (200 km) shows a generally poor fit to all but the heat flow data. In contrast the predictions of the 125 km thick plate model are in good agreement with the depth-age and heat flow-age data (Parsons and Sclater, 1977) and provide the best overall fit to the Mendocino geoid slope - age estimates.

Although on the average the 125 km thick plate model has the best fit to all of the data it does not fit the Mendocino geoid slope estimates in detail. A 100 km thick plate model provides a better fit to these estimates between 15 and 60 Myr while a 140 km thick plate model better fits the estimates at greater ages. This same effect occurs with the North Pacific seafloor depths although these deviations are hidden in Figure 10 by averaging seafloor depths along isochrons. The North Pacific contains large areas of seafloor that are either shallower or deeper than the average depth-age relation (Menard, 1973; Mammerrickx, 1981). Such broad residual depth anomalies have been explained by age independent

heat inputs into the base of the lithosphere, i.e. lithospheric reheating (Heestand and Crough, 1981). By averaging along isochrons, the average depth-age relation is extracted and the residual depth anomalies are reflected in the uncertainties.

In this study we have sampled only a small portion of the seafloor that is adjacent to the Mendocino FZ. Therefore, our geoid slope - age estimates may not represent the average geoid slope - age relation in the North Pacific. Furthermore, we have shown that these estimates are very sensitive to the thermal structure of the lowermost portion of the lithosphere. It appears that the significant departures (Figure 9) in the geoid slope-age estimates from the 125 km thick plate model are reflecting deviations in the thermal structure along the Mendocino FZ from the plate cooling model. Obviously this occurs along the portion of the Mendocino FZ that is crosscut by the Hawaiian swell since the FZ geoid signal is absent in this region. In addition, smaller reheating anomalies that have intersected other segments of the Mendocino FZ will also erase a portion of the FZ geoid signal. The enhanced sensitivity of the geoid height to thermal perturbations near the base of the lithosphere makes this data set very useful for mapping lithospheric reheating anomalies.

APPENDIX : A SIMPLE FRACTURE ZONE MODEL

The geometry of the two-layer FZ model (Dorman, 1975) is shown in Figure 1. The gravitational potential  $U$  is produced by two semi-infinite sheets of mass with mass per unit area  $\sigma$  and  $-\sigma$  at depths  $s$  and  $d$  beneath the observation plane. The potential  $U$  is the three-dimensional convolution of the density structure  $\rho$  with the Green's function due to a point mass

$$U(\underline{r}) = \int \rho(\underline{r}_0) \frac{G}{|\underline{r} - \underline{r}_0|} dV_0 \quad , \quad (A1)$$

where  $\underline{r}_0$  is the position vector of the source,  $\underline{r}$  is the location of the observer,  $dV_0$  is the element of volume at  $\underline{r}_0$ , and the integration extends over all space. Upon integrating over  $z_0$  from  $-\infty$  to  $+\infty$  and over  $y_0$  from  $-L$  to  $L$  we find

$$U(x,0,0) = G\sigma \int_0^\infty \ln \left[ \frac{L + (L^2 + a_1^2)^{1/2}}{-L + (L^2 + a_1^2)^{1/2}} \cdot \frac{-L + (L^2 + a_2^2)^{1/2}}{L + (L^2 + a_2^2)^{1/2}} \right] dx_0 \quad , \quad (A2)$$

where

$$a_1^2 = (x - x_0)^2 + s^2 \quad \text{and} \quad a_2^2 = (x - x_0)^2 + d^2 \quad . \quad (A3)$$

In the limit  $L \rightarrow \infty$  (A2) becomes

$$\begin{aligned} U(x) &= G\sigma \int_0^\infty \ln \left( \frac{(x - x_0)^2 + d^2}{(x - x_0)^2 + s^2} \right) dx_0 \quad , \\ &= 2\pi G\sigma d \left\{ \frac{1}{2} \left( 1 - \frac{s}{d} \right) + \frac{1}{\pi} \left( \arctan \frac{x}{d} - \frac{s}{d} \arctan \frac{x}{s} \right) + \frac{x}{2\pi d} \ln \left( \frac{x^2 + d^2}{x^2 + s^2} \right) \right\} . \end{aligned} \quad (A4)$$

To first order, the geoid height  $N$  is  $U/g$ . It is noteworthy that the potential

for this model is undefined, on a flat earth, if the densities of the mass layers are not equal and opposite (the requirement of isostatic compensation). The slope of the potential, which is used in our fitting procedure, is

$$\frac{dU}{dx} = G\sigma \ln \left( \frac{x^2 + d^2}{x^2 + s^2} \right) \quad (A5)$$

#### ACKNOWLEDGMENTS

We thank Russell Agreen for providing many of the Seasat altimeter profiles and LeRoy Dorman for helpful suggestions. This work was supported by the NASA Geodynamics Program under grant NAG 5152.

## Appendix B: A Physical Fracture Zone Geoid Model

We have shown that the geoid height for the simple two layer model fits within the noise level of the observed geoid slope and can be used to estimate the overall geoid step. However, this simple model cannot be directly related to any physical properties of the oceanic lithosphere. In this appendix we derive a physically reasonable FZ geoid model that is also able to match the observed geoid profiles. We then relate the parameters of the physical model to the parameters of the two layer model, derived in Appendix A.

The physical model incorporates some simplifying assumptions about the state of stress and the thermal structure across a FZ. It consists of two isostatically compensated quarter spaces. Each has the thermal structure of a half space that has cooled from an initial constant mantle temperature  $T_m$  by conductive heat loss through the seafloor. The temperature at some time  $t$  after the lithosphere was formed is

$$T(z',t) = T_m \operatorname{erf}\left(\frac{z'}{2(\kappa t)^{1/2}}\right) \quad (\text{B-1})$$

where  $z'$  is the depth beneath the seafloor and  $\kappa$  is the thermal diffusivity. We'll assume that each of the quarter spaces is thermally and mechanically isolated from the other. Thus the temperature on the right side of the FZ shown in Figure 1 is  $T(z',t_1)$  and the temperature on the left side is  $T(z',t_2)$ . As each quarter space cools

its density increases linearly with decreasing temperature according to

$$\rho(z', t) = \rho_m (1 + \alpha(T_m - T(z', t))) \quad (\text{B-2})$$

where  $\rho_m$  is the mantle density and  $\alpha$  is the coefficient of thermal expansion. Each quarter space must subside to remain in local isostatic equilibrium and the seafloor depth increases with age as

$$D(t) = D_{\text{ref}} + \frac{2 \alpha \rho_m T_m}{(\rho_m - \rho_w)} (\kappa t / \pi)^{1/2} \quad (\text{B-3})$$

where  $D_{\text{ref}}$  is the ridge crest depth and  $\rho_w$  is the seawater density. The density versus depth structure on either side of the FZ is

$$\rho(z, t) = \begin{cases} \rho_m & z < D(t) \\ \rho_m \left( 1 + \alpha T_m \operatorname{erfc} \left( \frac{z - D(t)}{2(\kappa t)^{1/2}} \right) \right) & z > D(t) \end{cases} \quad (\text{B-4})$$

where  $z$  is the depth beneath the seasurface. Since we are interested in changes in gravitational potential across the FZ, we subtract the density-depth function on the left side  $\rho(z, t_2)$  from the density-depth function on the right side  $\rho(z, t_1)$ . The remaining density structure is



$$\Delta\rho(x,z,t_1,t_2) = H(x) \begin{cases} 0 & z < D(t_1) \\ \rho(z,t_1) - \rho_w & D(t_1) < z < D(t_2) \\ \rho(z,t_1) - \rho(z,t_2) & D(t_2) < z \end{cases} \quad (\text{B-5})$$

where  $H(x)$  is the Heaviside step function. This density-depth function has a large positive density contrast of  $2400 \text{ kg m}^{-3}$

between depths of  $D(t_1)$  and  $D(t_2)$ . In the simple two-layer model we approximated this sharp density contrast by a Delta function. Beneath  $D(t_2)$  the density contrast is negative and has a peak that broadens and increases in depth as the FZ ages. This negative compensating density does not resemble the negative Delta function used in the simple two-layer model. However, the two-layer model and the physical model produce similar geoids if the depth to the negative Delta function compensation is chosen properly.

The gravitational potential across the FZ is most easily calculated from

$$U(k) = \frac{2\pi G}{|k|} \int_0^{\infty} \Delta\rho(k,z) e^{-|k|z} dz \quad (\text{B-6})$$

where  $k$  is the wavenumber and

$$\Delta\rho(k,z) = \int_{-\infty}^{\infty} \Delta\rho(x,z) e^{-ikx} dx \quad . \quad (B-7)$$

Dorman (1975) has evaluated (B-7) for a step function horizontal density variation and has found

$$\Delta\rho(k,z) = \Delta\rho(z)/ik \quad . \quad (B-8)$$

After substituting (B-4) into (B-5), (B-5) into (B-8) and finally (B-8) into (B-6) we find

$$U(k,t_1,t_2) = \frac{-2\pi iG}{k|k|} \left[ \int_{D_1}^{D_2} (\rho_m - \rho_w) e^{-|k|z} dz + \alpha \rho_m T_m \int_{D_1}^{\infty} \operatorname{erfc}\left(\frac{z-D_1}{2(\kappa t_1)^{1/2}}\right) e^{-|k|z} dz - \alpha \rho_m T_m \int_{D_2}^{\infty} \operatorname{erfc}\left(\frac{z-D_2}{2(\kappa t_2)^{1/2}}\right) e^{-|k|z} dz \right] \quad (B-9)$$

where  $D_1 = D(t_1)$  and  $D_2 = D(t_2)$ . The first integration is trivial. To evaluate the second integral, we let  $z' = z - D_1$  and the second term in brackets becomes

$$\alpha \rho_m T_m e^{-|k|D_1} \int_0^{\infty} \operatorname{erfc}\left(\frac{z'}{2(\kappa t_1)^{1/2}}\right) e^{-|k|z'} dz' \quad (B-10)$$

The integral in (B-10) is the Laplace transform of  $\operatorname{erfc}(z')$ . The third integral in (B-9) is evaluated in a similar fashion. The potential, in the Fourier transform domain is

$$\begin{aligned}
U(k, t_1, t_2) = \frac{2\pi i G}{k |k|^2} & \left[ (\rho_m - \rho_w) (e^{-|k|D_2} - e^{-|k|D_1}) \right. \\
& + \alpha \rho_m T_m e^{-|k|D_2} \{1 - g(|k| (\kappa t_2)^{1/2})\} \\
& \left. - \alpha \rho_m T_m e^{-|k|D_1} \{1 - g(|k| (\kappa t_1)^{1/2})\} \right]
\end{aligned}
\tag{B-11}$$

where  $g(z) = e^{z^2} \operatorname{erfc}(z)$  . (B-12)

This solution can be compared with the Fourier transform of the potential for the two-layer model, derived in Appendix A . The density versus depth function for the model shown in Figure 1 is

$$\Delta \rho(z) = \sigma ( \delta(z-s) - \delta(z-d) ) . \tag{B-13}$$

Inserting (B-13) into (B-8), (B-8) into (B-6) and integrating over  $z$  we find

$$U_2(k) = \frac{2\pi i G \sigma}{k |k|} (e^{-|k|s} - e^{-|k|d}) \tag{B-14}$$

which is the Fourier transform of (A-4). To compare (B-11) with (B-14) we let  $s = (D_1 + D_2)/2$  and  $\Delta D = (D_2 - D_1)$  so that

$$D_1 = s - \Delta D/2 \text{ and } D_2 = s + \Delta D/2 . \tag{B-15}$$

After substituting (B-15) into (B-11) we find

$$U(k, t_1, t_2) = \frac{2\pi i G}{k |k|} e^{-|k|s} \left[ (\rho_m - \rho_w + \alpha \rho_m T_m) (e^{\Delta D'} - e^{-\Delta D'}) + \alpha \rho_m T_m e^{\Delta D'} g(|k| (\pi t_2)^{1/2}) - \alpha \rho_m T_m e^{-\Delta D'} g(|k| (\pi t_1)^{1/2}) \right] \quad (B-16)$$

where  $\Delta D' = |k| D/2$ . By expanding the first two exponentials containing  $\Delta D'$  in a Taylor series about 0, discarding the terms of order  $\Delta D'^2, \Delta D'^3 \dots$ , and comparing the remaining term with the first term in (B-14) we find

$$\sigma = (\rho_m - \rho_w + \alpha \rho_m T_m) (D_2 - D_1) \quad (B-17)$$

This rather unsurprising result shows the relationship between  $\sigma$ , the surface mass anomaly of the two-layer model, and the bathymetric step of the physical FZ model. A relationship between the other free parameter of the two-layer model  $d$ , the depth of the compensating layer, and the parameters of the physical model can only be obtained in the limit as  $|k| \rightarrow 0$ . For this specific case Crough (1979) has found

$$d - s = (\pi \kappa)^{1/2} \left\{ (t_2)^{1/2} + (t_1)^{1/2} \right\} / 2 \quad (B-18)$$

The two models predict the same overall geoid step when their parameters are related through equations (B-17) and (B-18). However, the shape of the geoid step, close to the FZ, is slightly different for the two models. Beyond a characteristic distance of  $(\kappa t)^{1/2}$ , where

$t$  is the age of the FZ, the two models have similar geoids; within a distance of  $(\kappa t)^{1/2}$  the two models have slightly different geoids. Using a typical value of thermal diffusivity, this characteristic distance is 5 km times  $(\text{age})^{1/2}$ , where age is in Myr.

Based upon this calculation it appears that the physical model should have been used to estimate the overall geoid step. The parameters  $\alpha$  and  $\kappa$  of the physical model could have been varied to match the geoid slope along each of the geoid tracks. However, we did not use this procedure for a number of reasons. First, the physical model does not account for the thermal and mechanical interactions across the FZ. Therefore the geoid predicted by this model cannot adequately represent the observed geoid in the vicinity of the FZ. Second, at greater ages, the physical model places a significant portion of the compensating mass at a depth greater than the thickness of the lithosphere (determined from depth-age modelling). Because of these two inadequacies of the physical model there is no advantage in using it instead of the simpler two-layer model as a means of estimating the overall geoid offset. Each model introduces a systematic bias in the estimate of the geoid step. We believe that this modelling bias is small.

## REFERENCES

- Atwater, T. and H.W. Menard, Magnetic lineations in the northeast Pacific, Earth Planet. Sci. Lett., 7, 445-450, 1970.
- Chapman, M.E., Geoid anomaly over mid-ocean ridges (abstract), EOS Trans. AGU, 58, 368, 1977.
- Chase, T.E., H.W. Menard, and J. Mammerickx, Topography of the North Pacific (chart TR-17): La Jolla, Institute of Marine Resources, Univ. of California, San Diego, 1971.
- Crough, S.T., Geoid anomalies across fracture zones and the thickness of the lithosphere, Earth Planet. Sci. Lett., 44, 224-230, 1979.
- Detrick, R.S., Jr., An analysis of geoid anomalies across the Mendocino fracture zone: Implications for thermal models of the lithosphere, J. Geophys. Res., in press, 1981.
- Dorman, L.M., The gravitational edge effect, J. Geophys. Res., 80, 2949-2950, 1975.
- Haxby, W.F., The mid-ocean ridge geoid anomaly (abstract), EOS Trans. AGU, 60, 391, 1979.
- Haxby, W.F. and D.L. Turcotte, On isostatic geoid anomalies, J. Geophys. Res., 83, 5473-5478, 1978.
- Hayes, D.E. and W.C. Pitman, Magnetic lineations in the North Pacific, Geol. Soc. America, Mem. 126, 291-314, 1970.
- Heestand, R.L. and S.T. Crough, The effect of hot spots on the oceanic age-depth relation, J. Geophys. Res., 86, 6107-6114, 1981.
- Jarvis, G.T. and W.R. Peltier, Flattening of ocean bathymetry profiles due to radiogenic heating in a convecting mantle, Nature, 285, 649-651, 1980.

- Larson, R.L. and C.G. Chase, Late Mesozoic evolution of the western Pacific Ocean, Geol. Soc. Amer. Bull., 83, 3627-3643, 1972.
- Larson, R.L. and W.C. Pitman, III, World-wide correlation of Mesozoic magnetic anomalies, and its implications, Geol. Soc. Amer. Bull., 83, 3645-3662, 1972.
- Lister, C.R.B. and E.E. Davis, Comments on 'Comparison of long-wavelength residual elevation and free air gravity anomalies in the North Atlantic and possible implications for the thickness of the lithospheric plate' by John G. Sclater, Lawrence A. Lawver, and Barry Parsons, J. Geophys. Res., 81, 4957-4959, 1976.
- Louden, K.E. and D.W. Forsyth, Thermal conduction across fracture zones and the gravitational edge effect, J. Geophys. Res., 81, 4869-4874, 1976.
- Mammerickx, J., Depth anomalies over Mesozoic crust in the Western Pacific, (preprint), 1981.
- Mammerickx, J. and S.M. Smith, Bathymetry of the Northeast Pacific, Geological Society of America, Map and Chart Series, in press, 1981.
- Marquardt, D.L., An algorithm for least-squares estimation of nonlinear parameters, J. Soc. Indust. Appl. Math., 2, 431-441, 1963.
- McKenzie, D.P., Some remarks on heat flow and gravity anomalies, J. Geophys. Res., 72, 6261-6273, 1967.
- Menard, H.W., Depth anomalies and the bobbing motion of drifting islands, J. Geophys. Res., 78, 5128-5137, 1973.
- Ness, G., S. Levi, and R. Couch, Marine magnetic anomaly timescales for the Cenozoic and late Cretaceous: A préces, critique, and synthesis, Rev. Geophys. Space Phys., 18, 753-770, 1980.

- Ockendon, J.R. and D.L. Turcotte, On the gravitational potential and field anomalies due to thin mass layers, Geophys. J. Roy. Astron. Soc., 48, 479-492, 1977.
- Oxburgh, E.R. and D.L. Turcotte, Mechanisms of continental drift, Rep. Prog. Phys., 41, 1249-1312, 1978.
- Parsons, B. and D.P. McKenzie, Mantle convection and the thermal structure of the plates, J. Geophys. Res., 83, 4485-4496, 1978.
- Parsons, B. and F.M. Richter, A relation between driving forces and geoid anomaly associated with mid-ocean ridges, Earth Planet. Sci. Lett., 51, 445-450, 1980.
- Parsons, B. and J.G. Sclater, An analysis of the variation of ocean floor bathymetry and heat flow with age, J. Geophys. Res., 82, 803-827, 1977.
- Richter, F.M. and B. Parsons, On the interaction of the two scales of convection in the mantle, J. Geophys. Res., 80, 2529-2541, 1975.
- Sandwell, D. and G. Schubert, Geoid height versus age for symmetric spreading ridges, J. Geophys. Res., 85, 7235-7241, 1980.
- Sandwell, D. and G. Schubert, Lithospheric flexure at fracture zones, J. Geophys. Res., submitted, 1981.
- Sandwell, D.T., G. Schubert, and R.V. Sailor, Geoid height across fracture zones (abstract), EOS Trans. AGU, 61, 1123, 1980.
- Schubert, G., C. Froidevaux, and D.A. Yuen, Oceanic lithosphere and asthenosphere: thermal and mechanical structure, J. Geophys. Res., 81, 3525-3540, 1976.
- Sclater, J.G., R.N. Anderson, and M.L. Bell, Elevation of ridges and evolution of the central eastern Pacific, J. Geophys. Res., 76, 7888-7915, 1971.



Sclater, J.G., C. Jaupart, and D. Galson, The heat flow through oceanic and continental crust and the heat loss of the earth, Rev. Geophys. Space Phys., 18, 269-311, 1980.

Sclater, J.G. and B. Parsons, Reply, J. Geophys. Res., 81, 4960-4964, 1976.

Turcotte, D.L. and E.R. Oxburgh, Finite amplitude convective cells and continental drift, J. Fluid Mech., 28, 24-42, 1967.

LITHOSPHERIC FLEXURE AT FRACTURE ZONES

David Sandwell and Gerald Schubert

Department of Earth & Space Sciences  
University of California  
Los Angeles, California 90024

July 15, 1981

## ABSTRACT

Bathymetric profiles across the Mendocino and Pioneer Fracture Zones (FZ's) are used to demonstrate the absence of vertical slip on the fossil fault planes. The scarp heights on these FZ's are constant with age and equal to the initial vertical offsets at the ridge - transform fault - FZ intersections. Because of the frozen-in scarp and the differential subsidence of lithosphere far from the FZ, the lithosphere bends in the vicinity of the FZ. This flexure results in a characteristic ridge-trough topographic FZ signature. The flexural amplitude, which is the difference between the scarp height and the overall change in depth across the FZ, increases with age. Good fits to the bathymetric profiles across the Mendocino and Pioneer FZ's are obtained by modelling the topography as the flexure of a thin elastic plate with an age-dependent effective elastic thickness. Results of the modelling indicate that the base of the elastic lithosphere is approximately defined by the 450°C isotherm. Maximum bending stresses at FZ's are on the order of 100 MPa, substantially less than the stresses encountered at subduction zones. Because the Mendocino and Pioneer FZ's are separated by less than a flexural wavelength they are elastically coupled.

## INTRODUCTION

Flexure of the oceanic lithosphere is commonly observed in the bathymetry across subduction zones and around islands and large seamounts (Turcotte, 1979). The trench and outer rise topography at a subduction zone is the flexural response of the elastic lithosphere to a vertical end load and bending moment applied at the trench axis (Gunn, 1937, 1947; Hanks, 1971; Watts and Talwani, 1974; Caldwell et al., 1976; Parsons and Molnar, 1976). The moat and outer rise topography surrounding many islands and seamounts is the flexural response of the elastic lithosphere to the isolated vertical load (Gunn, 1943; Walcott, 1970; Watts and Cochran, 1974; Watts, 1978). The wavelength of the flexural topography is a function of the effective elastic thickness  $h_e$  of the lithosphere, while the amplitude of the flexure depends on both  $h_e$  and the applied bending moment or vertical load.

Recent flexure studies of subducting oceanic lithosphere and lithosphere loaded by the Hawaiian-Emperor chain have shown that the effective elastic thickness of the lithosphere is approximately proportional to  $(\text{age})^{1/2}$  (Watts, 1978; Caldwell and Turcotte, 1979; McNutt, 1979; Watts et al., 1980; Bodine et al., 1981). This behavior basically reflects the age-dependent thermal structure of the lithosphere and the strong temperature-dependence of the creep processes which tend to relieve flexural stresses. To a first approximation, the uppermost portion of the lithosphere has a viscous relaxation time that is greater than the age of the lithosphere and it therefore exhibits elastic behavior; the lower portion of the lithosphere is hotter, less viscous, and relieves stresses on a much shorter time scale (Caldwell and Turcotte, 1979). The division between the upper elastic and lower viscous portions of the lithosphere occurs at a temperature between 300 and 600°C according to Watts et al. (1980), while Turcotte (1979) suggests a temperature of 700°C.

In this paper we demonstrate that lithospheric flexure also occurs at an oceanic fracture zone (FZ) as a consequence of the difference in subsidence rates on either side of the FZ and the permanence of the initial bathymetric step across the FZ. Figure 1 illustrates why this flexure occurs. Initially a FZ separates newly created lithosphere (0 Myr) from older lithosphere (20 Myr) (see A-A' on Fig. 1). As these two segments of lithosphere move away from the ridge crest from A-A' to B-B' the depth far from the FZ on the younger lithospheric segment increases at a higher rate than the depth far from the FZ on the older segment (Menard and Atwater, 1969; DeLong et al., 1977; Sibuet and Mascle, 1978). This effect is shown by the two subsidence curves in the middle of Fig. 1. By the time the two segments have evolved to B-B' the overall change in depth across the FZ,  $h_B$ , is less than the initial value  $h_A$ . We propose, however, that the FZ does not slip during its evolution. Therefore the height of the scarp at the fracture zone will remain at its initial value  $h_A$ . The lithosphere must flex to satisfy both of these requirements as shown in the lower portion of Fig. 1. The amplitude of this flexure  $\delta_B$  is the change in the differential subsidence from A to B, i.e.  $h_A - h_B$ . Further evolution from B to C increases the flexural amplitude to  $\delta_C$ . The shape of this flexural topography depends upon the effective elastic thickness  $h_e$  of the lithosphere. Since  $h_e$  is proportional to  $(\text{age})^{1/2}$ , the flexure is asymmetric about the FZ with the younger lithosphere flexing at a shorter wavelength than the older lithosphere.

The major objectives of this study are to demonstrate that lithospheric flexure occurs across the Pioneer and Mendocino FZ's and that this flexural topography is a primary topographic expression at these FZ's. This is accomplished by modelling the flexure and comparing the predicted depths with five bathymetric profiles crossing the two FZ's at different ages. The model for

Figure 1. Evolution of a FZ. Top; spreading ridges offset by a transform fault. The age offset across the FZ is  $t_B' - t_B$ . Center; the  $h$ 's are the differences in ocean floor depth between locations far to either side of the FZ. The initial height of the scarp at the FZ is  $h_A$ . If the FZ does not slip, the scarp height must remain constant. The constancy of scarp height and the decrease in  $h$  with age cause the lithosphere in the vicinity of the FZ to bend. The flexural amplitude  $\delta_B$  is the difference between  $h_A$  and  $h_B$ . Similarly  $\delta_C = h_A - h_C$ . Bottom; sketch of bathymetry along profiles A-A', B-B', and C-C' illustrating the lithospheric flexure described above.

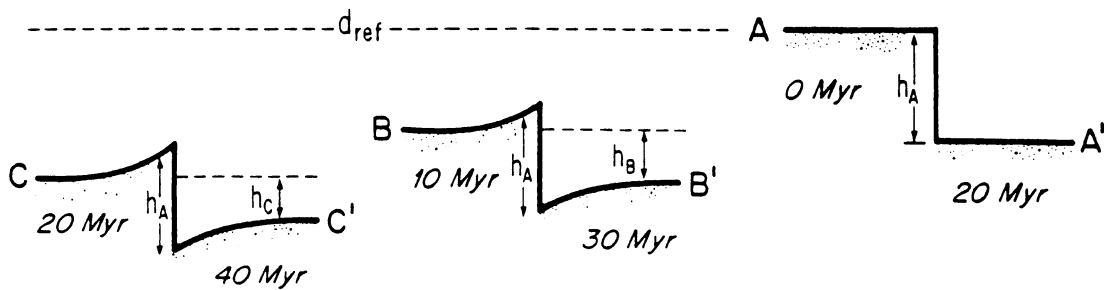
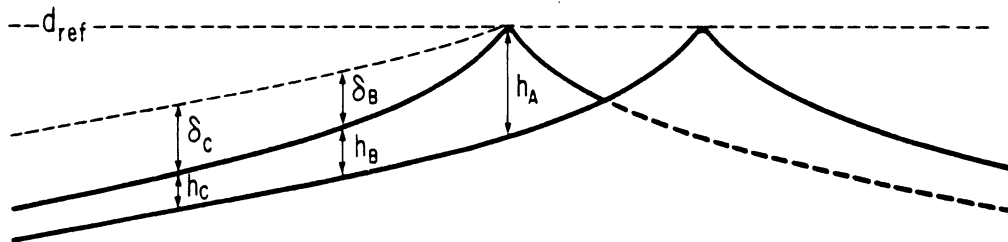
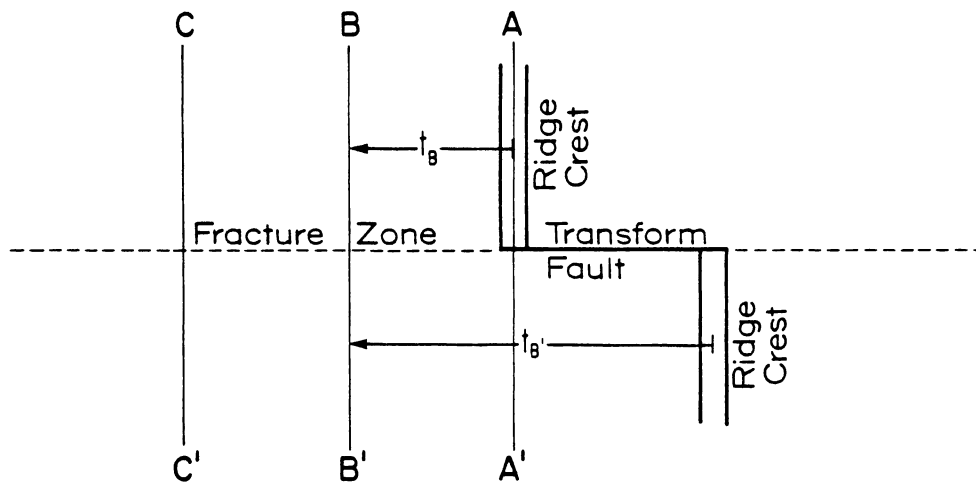


Figure 1

computing the flexure utilizes a thin elastic plate overlying an incompressible fluid half-space. The model also incorporates a temperature-dependent effective elastic thickness. The ages on each side of the FZ determine both the initial bathymetric step across the FZ and the vertical offset of distant ocean floor. Therefore the only adjustable model parameter is the stress relaxation temperature  $T_e$  which defines the base of the elastic layer. We will show that good fits between the observed and predicted bathymetric profiles are obtained by varying this single parameter. These good fits also confirm the absence of vertical slip on the fossil fault planes of the Mendocino and Pioneer FZ's.

The temperature dependence of  $h_e$  turns out to be an essential feature of the model; without it flexure could not reproduce the curvature in the bathymetric profiles. Therefore, this is independent evidence for the temperature dependence of  $h_e$ . The flexure models also yield estimates of the maximum bending stresses and average shear stresses in the lithosphere. We compare these with the magnitudes of the stresses caused by plate bending at ocean trenches. Finally, we calculate the flexure caused by horizontal conduction of heat across a FZ and demonstrate that it has a relatively small effect upon the bathymetry.

#### DATA

The Mendocino and Pioneer FZ's in the North Pacific were chosen to test our model of flexure at fracture zones primarily because they have a combined age offset of about 30 Myr and should therefore show large flexural amplitudes. The study region (Fig. 2) was limited to the area between the Juan de Fuca ridge and  $150^{\circ}\text{W}$  because it contains identified magnetic anomalies (Atwater and Menard,



Figure 2. Map of the northwest Pacific showing the locations of the five bathymetric profiles A - E crossing the Mendocino and Pioneer FZ's. The Mendocino FZ divides into north and south branches west of  $140^{\circ}\text{W}$ . Modified from Mammerickx (1981).

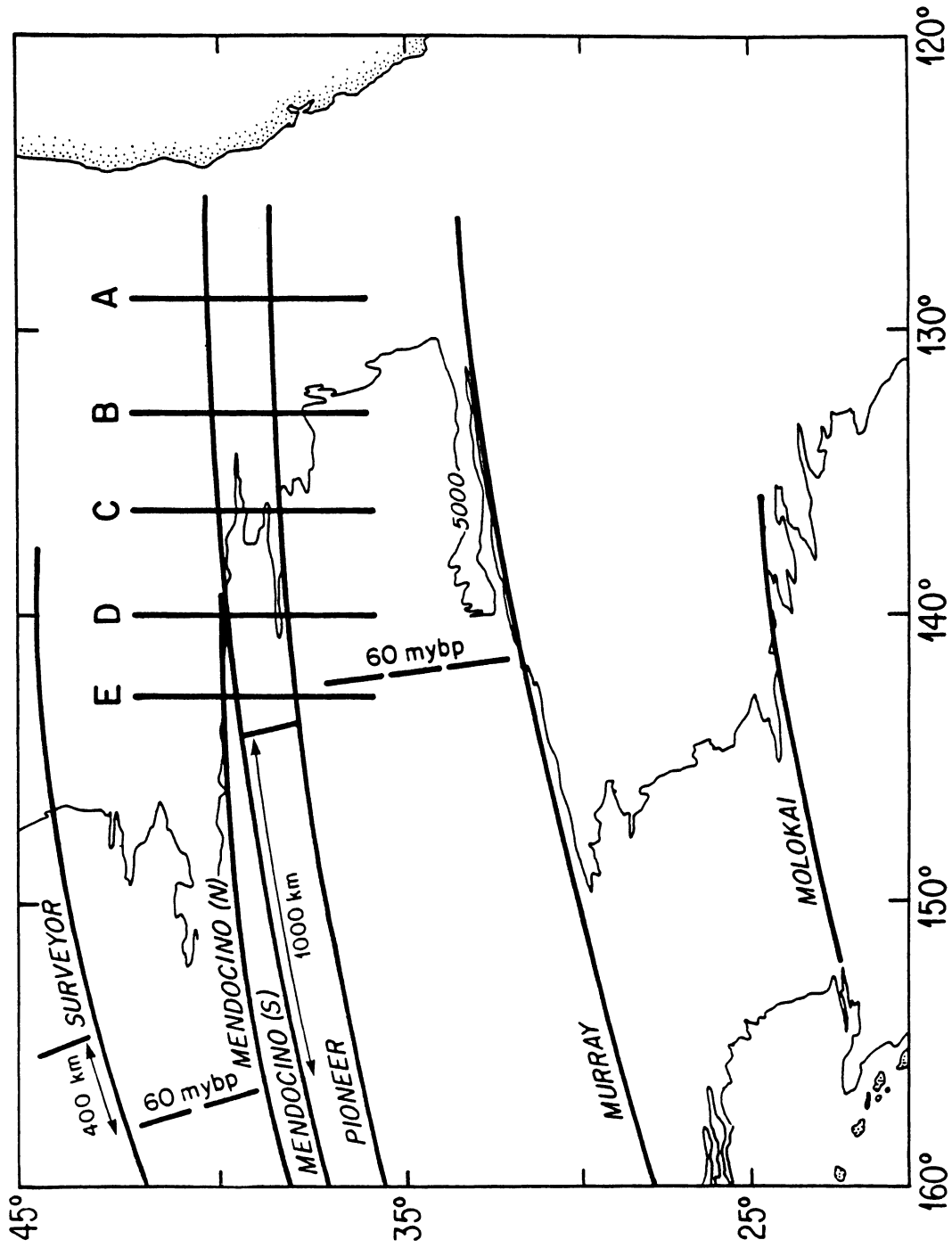


Figure 2

1970). These anomalies were dated by using the magnetic time scale of Ness et al. (1980). The Mendocino FZ has an age offset which varies between 30 Myr at 128°W and 25 Myr at 140°W. To the west of 140°W, the Mendocino divides and the age offset gradually shifts from the northern branch to the southern branch. However, only the total age offset across both FZ's is known since the lithosphere between these two FZ's does not contain identified magnetic anomalies. The Pioneer FZ runs subparallel to the Mendocino FZ and has an age offset which varies between 8 Myr at its eastern end and 4 Myr at 140°W.

Five N-S trending bathymetric profiles crossing both FZ's were chosen for this study and are shown in Fig. 2. A few other continuous N-S profiles are available; however these additional profiles lie within 100 km of the five we have chosen and they therefore contain redundant information. The depths along each of the profiles were obtained from the sounding charts used to construct the "Bathymetry of the Northeast Pacific" contour map (Mammerickx and Smith, 1981). The spacings between soundings varied from 1 to 2 minutes of latitude. Because of this rather coarse sampling the shortest wavelength topography is aliased, but the longer wavelength topographic features are unaffected.

The bathymetry along each of the profiles A - E in Fig. 2 is shown in Fig. 3 together with the ages of each lithospheric segment. The dashed lines are the bathymetric profiles predicted by the depth-age relation (equation (1) of the following section) and the parameter values in Table 1. The predicted depths are in approximate agreement with the data for locations more than 1° (111 km) away from each of the FZ's (marked by arrows in Fig. 3). However, in the vicinity of each FZ there are large systematic differences between the predicted and observed depths. In each case, the ocean floor is anomalously shallow on the younger side of the FZ, while on the older side it is generally

Figure 3. Relative depth as a function of latitude along profiles A - E. Profiles are offset in increments of 2.3 km. Dashed lines are depths predicted from (1). FZ's are marked by arrows. The Pioneer FZ appears on each profile at  $38^{\circ}$  -  $39^{\circ}$ N. The Mendocino FZ lies at  $\sim 40^{\circ}$ N. The Mendocino S. is well defined on profile E at  $39.6^{\circ}$ N. It is seen that (1) predicts the overall change in depth across a FZ, but not the scarp height.

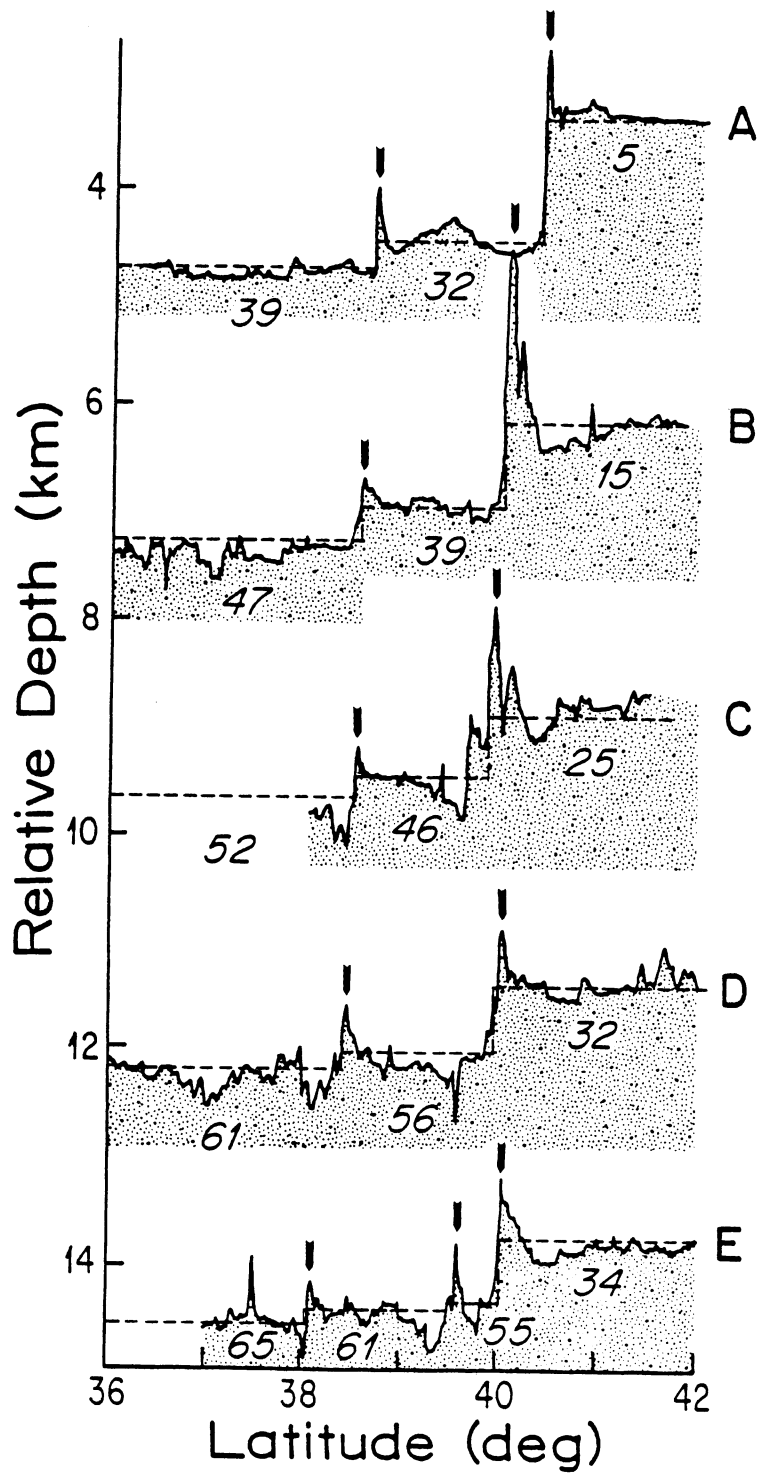


Figure 3

deeper than expected. We will show that the depth anomalies in Fig. 3 are a consequence of lithospheric flexure.

#### MODEL

As the oceanic lithosphere ages, it cools and subsides according to the depth-age relation (Davis and Lister, 1974; Parsons and Sclater, 1977; Oxburgh and Turcotte, 1978)

$$d(t) = d_{\text{ref}} + \frac{2\alpha\rho_m(T_m - T_s)}{(\rho_m - \rho_w)} \left(\frac{\kappa t}{\pi}\right)^{\frac{1}{2}}, \quad (1)$$

where the definitions of the parameters, and their values, are given in Table 1. Thus, the bathymetric step  $h_A$  across the youngest part of the FZ, section A-A' in Fig. 1, is given by

$$h_A = d(t_{A'}) - d(0) = \frac{2\alpha\rho_m(T_m - T_s)}{(\rho_m - \rho_w)} \left(\frac{\kappa t_{A'}}{\pi}\right)^{\frac{1}{2}}, \quad (2)$$

where  $t_{A'}$  is the age offset across the FZ and  $t_A = 0$ . This bathymetric step is assumed to be frozen-in on the fossil fault plane as the FZ ages. However, the overall change in depth across the FZ decreases with age; along section B-B' in Fig. 1 it is  $h_B$ , where

$$h_B = d(t_{B'}) - d(t_B) = \frac{2\alpha\rho_m(T_m - T_s)}{(\rho_m - \rho_w)} \left(\frac{\kappa}{\pi}\right)^{\frac{1}{2}} (t_{B'}^{\frac{1}{2}} - t_B^{\frac{1}{2}}) \quad (3)$$

and  $t_B$  and  $t_{B'}$  are the ages of the lithosphere at section B-B'. The amplitude of the flexure at B-B' is

$$\delta_B = h_A - h_B = \frac{2\alpha\rho_m(T_m - T_s)}{(\rho_m - \rho_w)} \left(\frac{\kappa}{\pi}\right)^{\frac{1}{2}} \left\{ (t_{B'} - t_B)^{\frac{1}{2}} + t_B^{\frac{1}{2}} - t_{B'}^{\frac{1}{2}} \right\} \quad (4)$$

where  $t_{A'} = t_{B'} - t_B$ . A contour plot of this flexural amplitude is shown in

TABLE 1. Definitions and Values of Parameters and Functions

Parameter	Definition	Value/Units	Reference
$\alpha$	thermal expansion coefficient	$3.1 \times 10^{-5} \text{ K}^{-1}$	1
$d_{\text{ref}}$	ridge crest depth	2500 m	1
$E$	Young's modulus	$6.5 \times 10^4 \text{ MPa}$	
$g$	acceleration of gravity	$9.82 \text{ m s}^{-2}$	
$\kappa$	thermal diffusivity	$8 \times 10^{-7} \text{ m}^2 \text{ s}^{-1}$	1
$\nu$	Poisson's ratio	0.25	
$\rho_m$	mantle density	$3330 \text{ kg m}^{-3}$	
$\rho_w$	seawater density	$1025 \text{ kg m}^{-3}$	
$T_e$	stress relaxation temperature	$450^\circ\text{C}$	2
$T_m$	mantle temperature	$1365^\circ\text{C}$	1
$T_s$	surface temperature	$0^\circ\text{C}$	

Function	Definition	Units
$d$	ocean floor depth	m
$\delta$	flexural amplitude	m
$D$	flexural rigidity	N m
$h$	overall change in depth across a fracture zone	m
$h_e$	effective elastic thickness	m
$\lambda$	flexural wavelength	m
$\sigma_{xx}$	bending stress	MPa
$\sigma_{xz}$	shear stress	MPa
$w$	flexural topography	m

<sup>1</sup>Parsons and Sclater (1977). <sup>2</sup>Watts et al. (1980).

Fig. 4 in terms of the age of the younger side of the FZ and the age offset. While flexural amplitude increases continuously with age, the rate of increase declines with age, and most of the amplitude is acquired while the FZ is young.

The wavelength of the flexure  $\lambda$  is given by

$$\lambda = 2\pi \left( \frac{4D}{g(\rho_m - \rho_w)} \right)^{1/4}, \quad (5)$$

where  $D$ , the flexural rigidity, is

$$D = \frac{Eh_e^3}{12(1 - \nu^2)} \quad (6)$$

The effective elastic thickness  $h_e$  is related to age  $t$  by (Caldwell and Turcotte, 1979)

$$h_e = 2(\kappa t)^{1/2} \operatorname{erfc}^{-1} \left( \frac{T_m - T_e}{T_m - T_s} \right) \quad (7)$$

where  $\operatorname{erfc}^{-1}$  is the inverse complimentary error function. Upon combining (5) - (7) we obtain

$$D = \frac{2E(\kappa t)^{3/2}}{3(1 - \nu^2)} \left\{ \operatorname{erfc}^{-1} \left( \frac{T_m - T_e}{T_m - T_s} \right) \right\}^3 \quad (8)$$

and

$$\lambda = 2\pi \left( \frac{8E}{3g(\rho_m - \rho_w)(1 - \nu^2)} \right)^{1/4} (\kappa t)^{3/8} \left\{ \operatorname{erfc}^{-1} \left( \frac{T_m - T_e}{T_m - T_s} \right) \right\}^{3/4} \quad (9)$$

The lithosphere on the younger side of the FZ flexes with a shorter wavelength than the lithosphere on the older side of the FZ because  $\lambda \propto t^{3/8}$ . In addition, the flexural wavelength on either side of the FZ increases as the FZ ages.



Figure 4. Contours of flexural amplitude  $\delta$  (calculated from (4)) as a function of the age offset across the FZ and the age on the younger side of the FZ. At constant age offset  $\delta$  increases most rapidly at young ages. Small age offset FZ's (e.g. 1 Myr) have flexural amplitudes of several hundred meters.

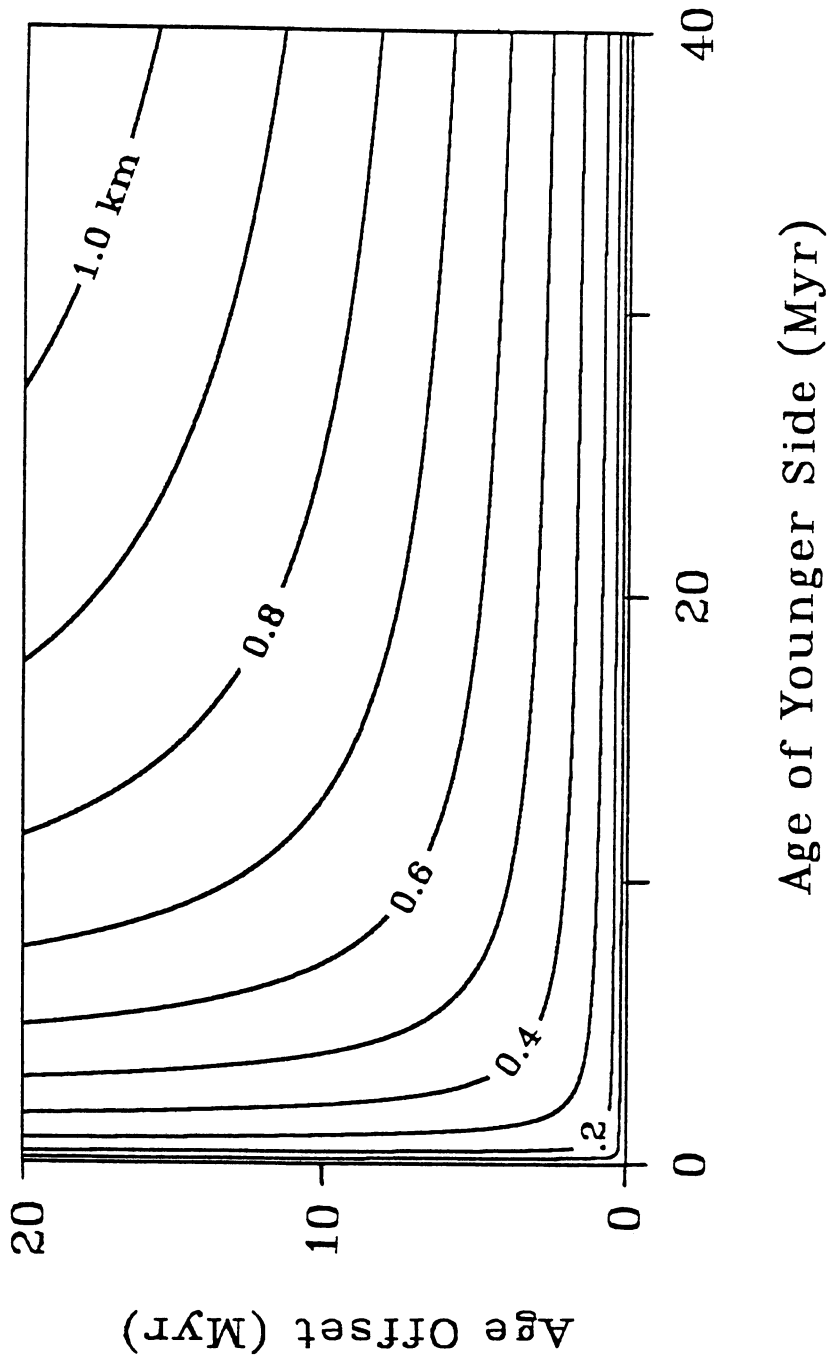


Figure 4

In calculating the flexural topography as a function of age along a FZ we have approximated the continuous time dependences of  $\delta$  and  $\lambda$  by using discrete 1 Myr time steps. Because the flexural problem is linear, the total flexural topography is the sum of the incremental contributions over all of the time steps up to the age of the FZ.

The separation distance between the Pioneer and Mendocino FZ's (150 - 220 km) is less than one flexural wavelength when the age of the lithosphere between the two FZ's is greater than about 10 Myr. This produces a coupling of the FZ's and requires that the flexural problem be formulated so as to explicitly include the interaction. We have actually modelled the most general case in which  $N + 1$  segments of lithosphere are separated by  $N$  FZ's. This configuration of FZ's is shown in Fig. 5 for the case  $N = 2$ . The  $i$ th segment of lithosphere has a flexural rigidity  $D_i$  that depends upon its age  $t_i$  according to (8). The  $i$ th FZ is located at  $x_i$  and the flexural topography between the  $i$ th and  $(i + 1)$ th FZ's is  $w_{i+1}(x)$ . The flexural amplitude at the  $i$ th FZ is  $\delta_i$ ; it is a function of the ages of the adjacent lithospheres and the duration of the time step since the previous increment of flexure.

The  $N + 1$  homogeneous differential equations governing the flexural topography are

$$\begin{aligned} D_1 \frac{d^4 w_1}{dx^4} + g(\rho_m - \rho_w) w_1 &= 0, & x < x_1, \\ D_i \frac{d^4 w_i}{dx^4} + g(\rho_m - \rho_w) w_i &= 0, & x_{i-1} < x < x_i, \\ D_{N+1} \frac{d^4 w_{N+1}}{dx^4} + g(\rho_m - \rho_w) w_{N+1} &= 0, & x_N < x. \end{aligned} \quad (10)$$

Their solutions are

Figure 5. Model used to calculate the flexural topography  $w(x)$  across multiple FZ's. Two FZ's are located at  $x_1$  and  $x_2$  and have flexural amplitudes  $\delta_1$  and  $\delta_2$ . The flexural rigidity is different for each segment of lithosphere.

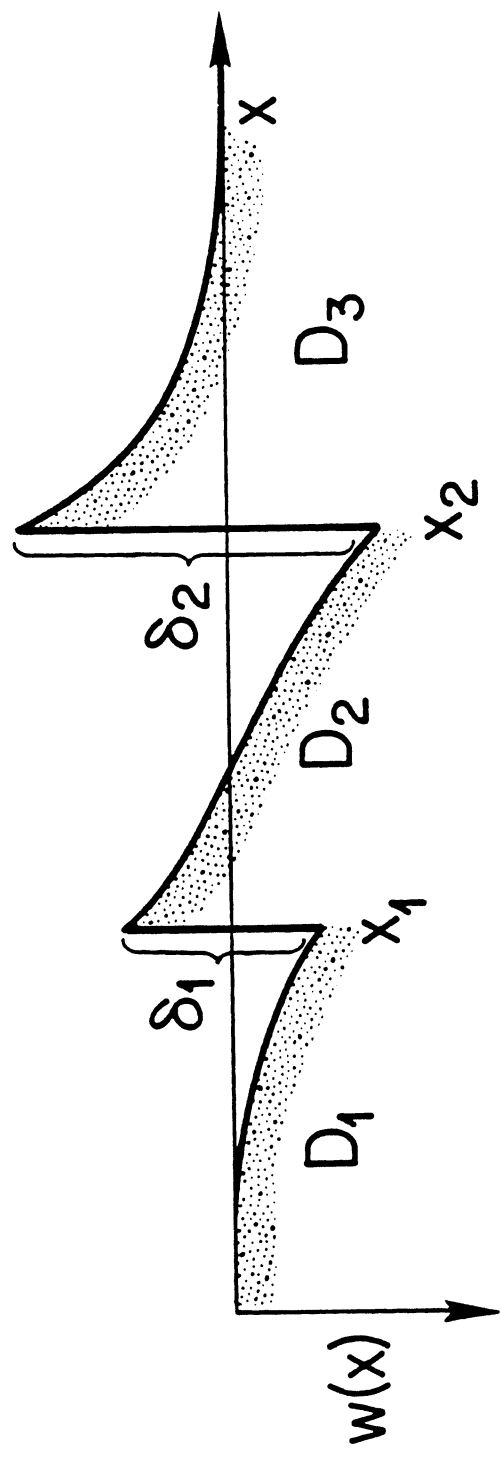


Figure 5

$$w_i(x) = e^{-\frac{2\pi x}{\lambda_i}} \left\{ A_i \sin \frac{2\pi x}{\lambda_i} + B_i \cos \frac{2\pi x}{\lambda_i} \right\} + e^{\frac{2\pi x}{\lambda_i}} \left\{ C_i \sin \frac{2\pi x}{\lambda_i} + D_i \cos \frac{2\pi x}{\lambda_i} \right\}, \quad (11)$$

for  $x_{i-1} < x < x_i$ , where  $\lambda_i$  is given by (9) with  $t = t_i$ . The coefficients  $A_i$ ,  $B_i$ ,  $C_i$ , and  $D_i$  are determined from the boundary conditions and matching conditions discussed below.

For  $N + 1$  lithospheric segments there are  $4(N + 1)$  coefficients to be determined. The boundary conditions require that the flexural topography must vanish as  $x \rightarrow \pm\infty$ . This condition is satisfied if the four coefficients  $A_1$ ,  $B_1$ ,  $C_{N+1}$ ,  $D_{N+1}$  are zero. The remaining  $4N$  coefficients are determined from 4 matching conditions at each of the  $N$  FZ's. At the  $i$ th FZ the displacement must be discontinuous by the amount  $\delta_i$ , while the slope, moment, and shear force must all be continuous. The matching conditions at  $x = x_i$  are therefore

$$w_i - w_{i+1} = \delta_i, \quad (12)$$

$$\frac{dw_i}{dx} - \frac{dw_{i+1}}{dx} = 0, \quad (13)$$

$$-D_i \frac{d^2 w_i}{dx^2} + D_{i+1} \frac{d^2 w_{i+1}}{dx^2} = 0, \quad (14)$$

$$-D_i \frac{d^3 w_i}{dx^3} + D_{i+1} \frac{d^3 w_{i+1}}{dx^3} = 0. \quad (15)$$

We have solved these  $4N$  equations by a method similar to the Thompson-Haskell technique (Haskell, 1953) used to determine the eigenfunctions and eigenfrequencies for Rayleigh and Love waves in a layered half-space.

Once the coefficients have been determined, the flexural topography can

be calculated from (11). Other quantities of interest are the maximum bending stresses  $\sigma_{xx}$  and the average shear stresses  $\sigma_{xz}$  in the elastic lithosphere. The maximum bending stress at the top of the  $i$ th lithospheric segment is

$$\sigma_{xx_i}(x) = \frac{-E h_e}{2(1 - \nu^2)} \frac{d^2 w_i}{dx^2}(x) = \frac{6M_i(x)}{h_e^2} \quad , \quad (16)$$

where  $M_i(x)$  is the bending moment

$$M_i(x) = -D_i \frac{d^2 w_i}{dx^2}(x) \quad . \quad (17)$$

The average shear stress  $\sigma_{xz}$  is the shear force divided by  $h_e$

$$\sigma_{xz_i}(x) = \frac{-D_i}{h_e} \frac{d^3 w_i}{dx^3}(x) \quad . \quad (18)$$

The total bathymetry across a FZ is found by calculating the flexural topography for each time step from zero to the age of the FZ, summing the flexure over all of the time steps, and finally adding this flexural topography along each lithospheric segment to the depths calculated from the depth-age relation.

## RESULTS

Figure 6 shows comparisons between model depths (dashed lines) and the five bathymetric profiles (solid lines). The values of the thermal parameters  $\alpha$ ,  $\kappa$  and  $T_m$  used in these model calculations are compatible with the depth-age and heat flow-age relations from the North Pacific (Parsons and Sclater, 1977).

Figure 6. Comparisons between theoretical bathymetric profiles computed from flexure models assuming no slip on the FZ's (dashed lines) and the observed bathymetric profiles A - E (solid lines). The asymmetric flexure predicted by the model across each FZ is a consequence of the increase in flexural wavelength with age according to (9). The apparent tilt in the bathymetry between the Pioneer and Mendocino FZ's occurs because the flexural wavelength is greater than their separation distance.



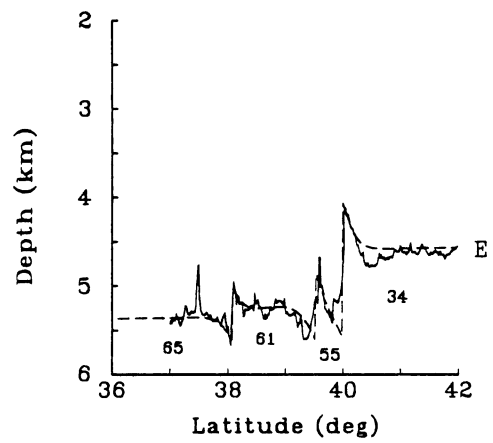
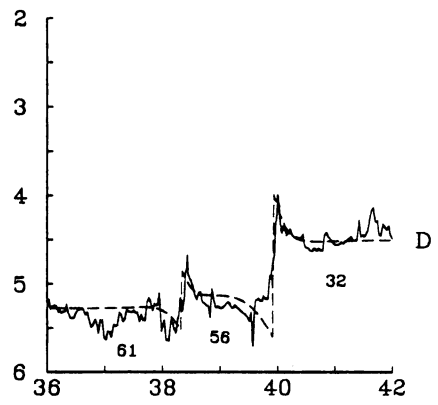
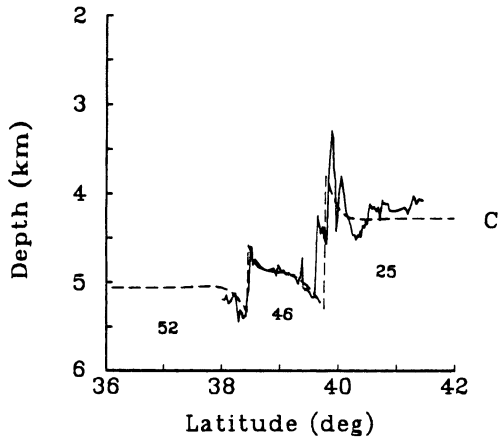
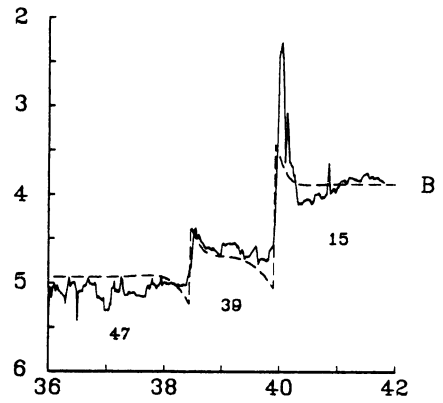
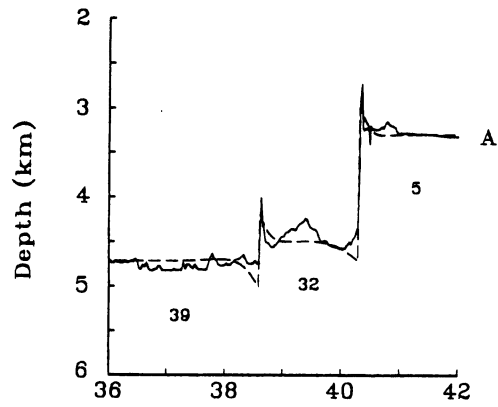


Figure 6

The value of the stress relaxation temperature  $T_e$  was adjusted until good fits were obtained for all five profiles. The models shown in Fig. 5 were calculated using  $T_e = 450^\circ\text{C}$  although reasonable fits were also obtained for values of  $T_e$  ranging from  $350^\circ\text{C}$  to  $600^\circ\text{C}$ .

The model predicts many of the features that appear in the observed profiles. In nearly every case the observed flexural amplitude is well matched by the model. This agreement indicates that these FZ's have not slipped significantly during their evolutions. The largest differences between the model and the data occur on the young side of the Mendocino FZ along profiles B and C. Equation (4) predicts only about 1/2 of the Mendocino scarp amplitude along profile B. The excess scarp amplitude may have been produced when the velocity vector of the Pacific plate was not parallel to the now subducted Mendocino transform fault (Menard and Atwater, 1969).

The asymmetry of the flexure about each FZ is a consequence of the increase in effective elastic thickness with age. This asymmetry is most apparent on profiles B - E, where the flexural wavelength on the young side of each FZ is shorter than the flexural wavelength on the older side. Initially, we modelled the flexure on these FZ's with a constant  $h_e$ . However, these models failed to fit the observed profiles since they could not reproduce the asymmetric flexure pattern. Thus, the flexure at these FZ's is independent evidence that  $h_e$  increases with age.

Probably the most pronounced flexural feature that appears on profiles B - E is the tilting (downward to the north) of the segment of lithosphere that lies between the Mendocino and Pioneer FZ's. This tilting occurs because the separation distance between the two FZ's is less than the flexural wavelength at the age when much of the flexure occurred. Thus, stresses are transmitted between the two FZ's and it is necessary to solve for the flexural topography

across both FZ's simultaneously.

Considering the good overall agreement between the observed bathymetry and the ocean floor depths predicted by the model, we believe that the characteristic ridge and trough topographic pattern at the Mendocino and Pioneer FZ's is the flexural response of the lithosphere to the differences in subsidence rates across the FZ's and the absence of slip on the FZ's. No vertical slip has taken place during the evolutions of these FZ's in spite of the large flexural amplitudes (about 1 km) that must be sustained by stresses transmitted across the fossil transform faults for periods of greater than 50 Myr.

The maximum bending stresses  $\sigma_{xx}$  and the average shear stresses  $\sigma_{xz}$  along each profile have been calculated from the flexure model using (16) and (18). The largest stresses occur along profile E and these are shown in Fig. 7. The locations of the three FZ's are also marked on this figure. Relative minima and maxima of  $\sigma_{xx}$  occur at points lying about 10 - 20 km to the south and north of each FZ, respectively. The largest maximum bending stress of -120 MPa occurs just south of the Mendocino S. FZ. The largest average shear stress of 28 MPa is found at the Menocino N. FZ. The maximum values of  $|\sigma_{xx}|$  and  $|\sigma_{xz}|$  attained along the other profiles are summarized in Table 2.

#### EFFECTS OF HORIZONTAL HEAT CONDUCTION

In this section we demonstrate that horizontal conduction of heat across the FZ has only a minor influence upon the bathymetry and that it is valid to neglect this effect in computing the model bathymetric profiles of Fig. 6. In writing the depth-age relation (1) we assumed that the thermal structure of the FZ is given by the half-space cooling model

Figure 7. Stresses along profile E. Top; maximum bending stress  $\sigma_{xx}$  at the top of the elastic layer. Arrows indicate locations of FZ's (P - Pioneer, MS - Mendocino S., MN - Mendocino N.). Bottom; average shear stress  $\sigma_{xz}$  within the elastic layer. Peaks occur at the three FZ's.

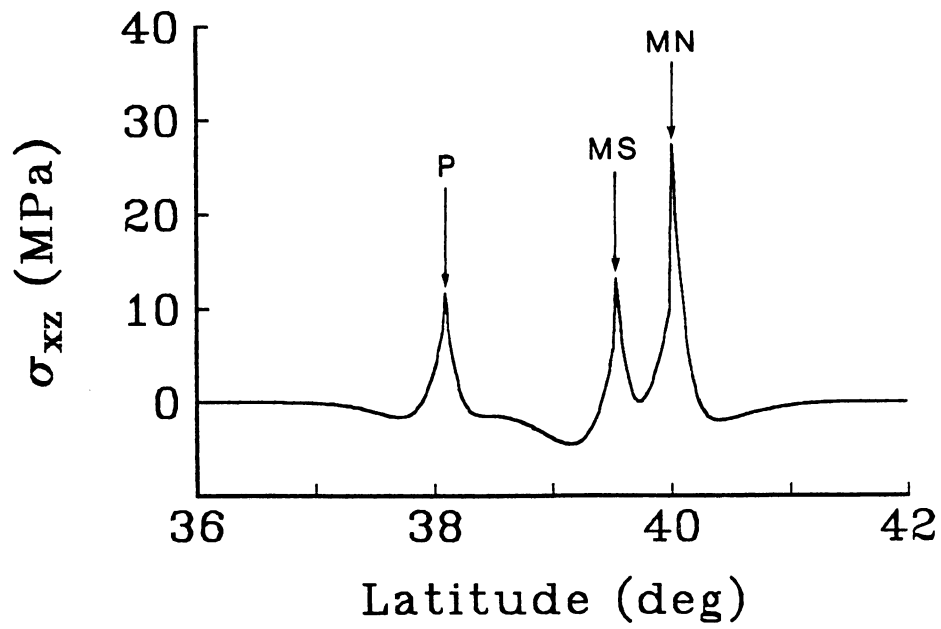
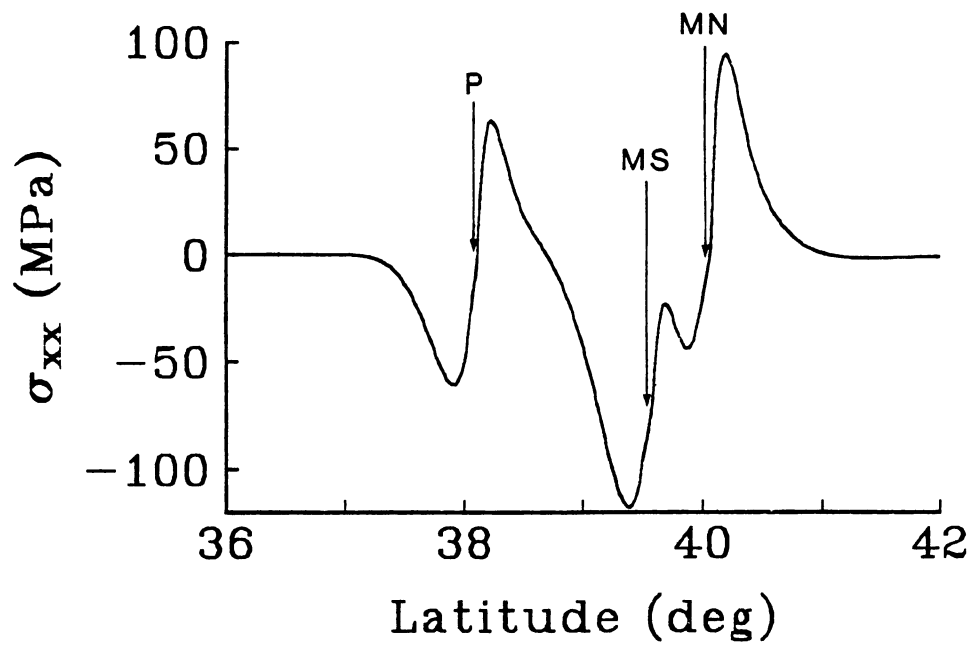


Figure 7

TABLE 2. Maximum Stresses (MPa)

Profile	Mendocino N.		Mendocino S.		Pioneer	
	$ \sigma_{xx} $	$ \sigma_{xz} $	$ \sigma_{xx} $	$ \sigma_{xz} $	$ \sigma_{xx} $	$ \sigma_{xz} $
A	70	20	-	-	72	13
B	88	28	-	-	76	18
C	92	29	-	-	67	16
D	98	30	-	-	68	14
E	95	28	122	14	60	13

In every case the maximum shear stress  $|\sigma_{xz}|$  occurs at the FZ. The maximum of  $|\sigma_{xx}|$  occurs 10 - 20 km north of each FZ except for the Mendocino S. on profile E where it occurs 20 km south of the FZ.

$$T(z,t) = (T_m - T_s) \operatorname{erf}\left(\frac{z}{2(\kappa t)^{1/2}}\right) + T_s \quad , \quad (19)$$

where  $z$  is the depth beneath the ocean floor and  $t$  is the age of the half-space. This gives a step change in temperature across the FZ as a consequence of the age offset. Actually, the temperature will vary in a continuous manner across the FZ because of horizontal heat conduction (Louden and Forsyth, 1976). The deviations in temperature from the step variation implied by (19) are responsible for buoyancy forces on the lithosphere which modify the flexural topography.

The two-dimensional temperature structure along B - B' in Fig. 1 is derived in Appendix A

$$T(x,z) = T_s + \frac{(T_m - T_s)}{2} \left\{ \operatorname{erfc}\left(\frac{x}{2(\kappa t_B)^{1/2}}\right) \operatorname{erf}\left(\frac{z}{2(\kappa t_B)^{1/2}}\right) + \operatorname{erfc}\left(\frac{-x}{2(\kappa t_B)^{1/2}}\right) \operatorname{erf}\left(\frac{z}{2(\kappa t_{B'})^{1/2}}\right) \right\} \quad , \quad (20)$$

The temperature due solely to horizontal heat conduction  $\Delta T(x,z)$  is found by constructing the step variation from (19) and subtracting it from (20)

$$\Delta T(x,z) = \frac{(T_m - T_s)}{2} \left\{ \left[ \operatorname{erfc}\left(\frac{-x}{2(\kappa t_B)^{1/2}}\right) - 2H(x) \right] \cdot \left[ \operatorname{erf}\left(\frac{z}{2(\kappa t_{B'})^{1/2}}\right) - \operatorname{erf}\left(\frac{z}{2(\kappa t_B)^{1/2}}\right) \right] \right\} \quad , \quad (21)$$

where  $H(x)$  is the Heaviside step function. The buoyancy forces arising from these temperature differences exert a pressure on the base of the lithosphere  $p(x)$  given by

$$p(x) = -g\alpha\rho_m \int_0^\infty \Delta T(x,z) dz \quad , \quad (22)$$

where  $\alpha$  is the coefficient of thermal expansion. Upon substituting (21) into (22) and performing the integration we find

$$p(x) = -g\alpha\rho_m (T_m - T_s) \left(\frac{\kappa}{\pi}\right)^{1/2} \left\{ (t_{B'})^{1/2} - (t_B)^{1/2} \right\} \left\{ 2H(x) - \operatorname{erfc}\left(\frac{-x}{2(\kappa t_B)^{1/2}}\right) \right\} \quad . \quad (23)$$

The pressure force is measured positive downward to be consistent with our sign convention for the flexural topography  $w$ .

The deflection of the lithosphere produced by this pressure is found by solving the equation for the thin elastic plate model (Turcotte, 1979)

$$D \frac{d^4 w}{dx^4} + g(\rho_m - \rho_w) w = p(x) \quad , \quad (24)$$

subject to the conditions that  $w$  and  $dw/dx$  approach zero as  $x$  tends to  $\pm\infty$ . To avoid the necessity of resorting to a numerical solution of (24), we will assume that  $D$  is constant across the FZ and has the value appropriate to the age of the lithosphere on the younger side of the FZ according to (8). This is a conservative assumption for the value of  $D$  since it actually overestimates the flexural topography caused by lateral heat conduction.

Equation (24) is most easily solved by taking its Fourier transform (Banks et al., 1977). We obtain

$$W(k) = \left( 1 + \frac{D|k|^4}{g(\rho_m - \rho_w)} \right)^{-1} \frac{2\alpha\rho_m(T_m - T_s)}{(\rho_m - \rho_w)} \left( \frac{x}{\pi} \right)^{\frac{1}{2}} \left( (t_B')^{\frac{1}{2}} - (t_B)^{\frac{1}{2}} \right) \cdot \frac{i}{k} \left[ 1 - \exp(-k^2 \kappa t_B) \right] \quad , \quad (25)$$

where  $k$  is the wavenumber and  $W(k)$  is the Fourier transform of  $w(x)$ . To obtain the topography  $w(x)$ , we invert (25) numerically using a fast Fourier transform procedure. The age dependence of  $D = D(t_B)$  is accounted for by applying (25) to discrete 1 Myr time intervals using the value of  $D$  appropriate to the interval and incrementing the plate deflection throughout the evolution of the FZ.

Figure 8 shows the topography due to horizontal heat conduction across a FZ with a 20 Myr age offset when the age of the younger side of the FZ is 5, 15, and 45 Myr. The magnitude of this flexural topography increases with the



Figure 8. Flexural topography associated with heat conduction across a FZ with a 20 Myr age offset. Ages of younger side are 5 Myr (solid line), 15 Myr (dashed line) and 45 Myr (dotted line). This topography broadens with age as heat diffuses across the FZ. The amplitude of this effect has been overestimated, especially on the older side of the FZ, since we used the flexural rigidity-age relation (8) of the younger side of the FZ in the theoretical calculation.

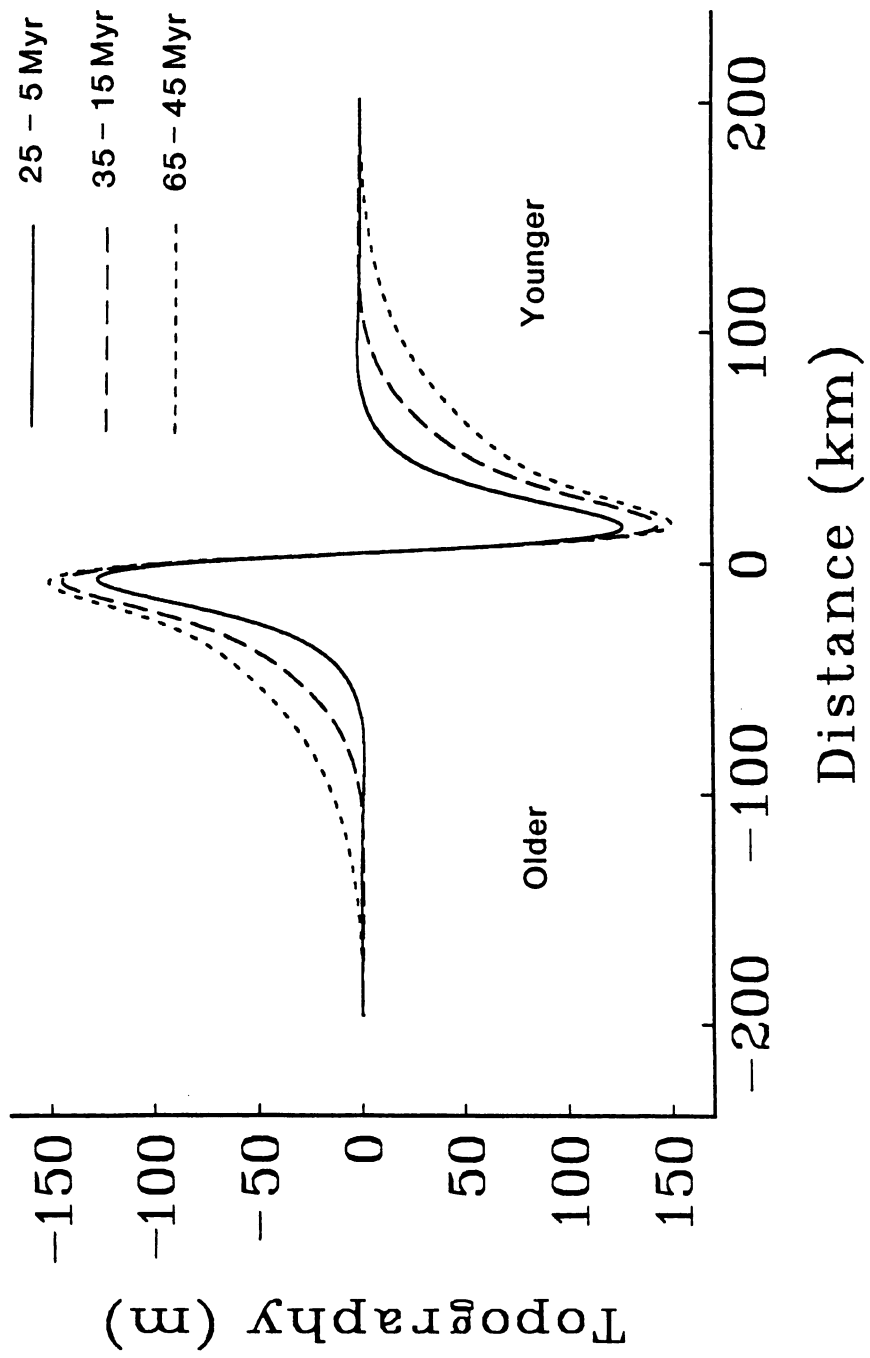


Figure 8

age of the FZ. The effects of horizontal heat conduction on the topography extend progressively farther from the FZ as it ages. We have seen in the model section that the flexural wavelength increases with age proportionately to  $t^{3/8}$ , while the thermal diffusion distance increases as  $t^{1/2}$ . Horizontal heat conduction does not change the flexural amplitude given by (4); it tends only to broaden the topographic profile. This is because the scarp height on the FZ is frozen-in and the differential subsidence far from the FZ is unaffected by heat conduction across the FZ. In agreement with this, the topography in Fig. 8 is zero both at  $x = 0$  and  $x = \pm\infty$ .

The amplitude of the topography in Fig. 8 is about 150 m. This is to be compared with the observed flexural amplitude of 500 m on profiles B - E in Fig. 6. It should be remembered that the topography of Fig. 8 significantly overestimates the effect of horizontal heat conduction on the older side of the FZ and may slightly overestimate it on the younger side because of our approximation to D. Therefore while flexure due to horizontal heat conduction is small it is not entirely negligible. In fact it may be responsible for the dips in the bathymetric profiles B - E on the north side of the Mendocino FZ (Fig. 6).

#### DISCUSSION AND CONCLUSIONS

Global, regional, and local seismicity studies indicate that FZ's do not slip over periods of time short enough to generate seismic disturbances. The majority of earthquakes with magnitudes greater than about 5 occur along plate boundaries including subduction zones, spreading centers and transform faults (Barazangi and Dorman, 1969). Large intraplate earthquakes rarely occur. A regional study of smaller intraplate earthquakes (magnitude greater than about 4) in the South Central Pacific showed that only one earthquake out of about one

hundred occurred at a FZ (Okal et al., 1980). Local studies of microseismicity at the intersections of transform faults, spreading ridges, and fracture zones demonstrate that while numerous microearthquakes occur along the transform faults and spreading ridges, the FZ's are seismically inactive (Reid, 1976; Francis et al., 1978; Forsyth and Rowlett, 1979; Rowlett, 1981).

Our study indicates that at least two major FZ's do not slip over a time scale of  $10^7$  yr, ruling out the possibility of aseismic slip on the FZ's. The models of the flexural topography across profiles A - E (Fig. 6) predict that the fossil transform faults must maintain shear stresses of up to 30 MPa. These stresses are more than twice as large as the stress drops derived from studies of major earthquakes (Brune, 1968). If a FZ were a zone of weakness then it should slip, like other faults, to relieve these large shear stresses. We conclude, therefore, that a FZ is not a zone of weakness; the fractured crust is only a remnant surface expression of past tectonic activity along the transform fault and spreading ridges. Beneath this fractured surface layer lies coherent oceanic lithosphere that is not significantly weaker than the surrounding lithosphere. This is not surprising when one considers the evolution of a FZ. The lithosphere on the younger side of the FZ is created by upwelling of hot mantle material along the ridge crest which terminates at the end of the transform fault (see Fig. 1). The material upwelling at this intersection cools rapidly because of its proximity to the older segment of lithosphere. Thus, the two segments of lithosphere fuse together at this intersection. The mechanical bond continues to increase in strength as the FZ ages. At depth, the FZ is not a structural boundary; instead it is a zone of large horizontal temperature gradients.

Our observation that the Pioneer and Mendocino FZ's have not slipped significantly during their evolutions has implications for FZ's with much

smaller age offsets and for FZ's situated on very old lithosphere. In both cases, the ridge and trough features predicted by our model should have sufficient amplitude to appear on large scale bathymetric charts with 100 or 200 m contour intervals.

Consider the older portions of the Mendocino FZ separating lithospheric segments of ages 135 Myr and 140 Myr (Mammerickx, 1981). The overall change in depth across this FZ is only 30 m according to the empirical depth-age relation of Parsons and Sclater (1977). If this were the only topographic expression of the FZ, then it would not be apparent on a bathymetric chart with a 100 m contour interval. However, the FZ is clearly delineated on the map of this region. Furthermore, the step in the bathymetry across a 500 km segment of this FZ lying between the Hawaiian-Emperor ridge and the Mapmaker Seamounts varies from 300 to 700 m (see Fig. 3 of Mammerickx, 1981). Our model predicts a step amplitude of 715 m along this portion of the Mendocino FZ. The agreement, although not perfect, indicates that this portion of the Mendocino FZ has not slipped significantly for over 130 Myr.

FZ's with very small age offsets should also be visible on bathymetric charts with a 100 m contour interval even when the overall change in ocean floor depth far from the FZ is less than 100 m. For example, (4) predicts that the bathymetric step across a FZ separating lithospheric segments with ages of 30 and 31 Myr is more than 300 m (see Fig. 2). The overall change in ocean floor depth far from the FZ is only 32 m in this case.

Fracture zones with both large and small age offsets can be traced for thousands of kilometers across the ocean floor. If FZ's slipped completely during their evolutions then their topographic expressions would diminish with age. However, the FZ topography persists on lithosphere with ages greater than 100 Myr. Some of this topography may be the result of fracturing in the transform fault environment. However, the major topographic expression (i.e.

the ridge and trough) is a consequence of the freezing in of the bathymetric step at the intersection of the transform fault with the ridge crest.

Lithospheric flexure at the Mendocino and Pioneer FZ's is qualitatively similar to the bending of the lithosphere at subduction zones and around large seamounts. The main difference is that the maximum bending stresses inferred from subduction zone and seamount studies are usually greater than 500 MPa, while the stresses at FZ's are substantially lower, about 100 MPa. Experimental and theoretical studies of lithospheric rheology indicate that the largest stresses inferred from purely elastic subduction zone models ( $\sim 10^3$  MPa) cannot be maintained (Kirby, 1980). Accordingly, flexure at subduction zones has been reinterpreted with more realistic elastic-plastic rheologies (Turcotte et al., 1978; McAdoo et al., 1978; Chapple and Forsyth, 1979; Forsyth, 1980; McNutt and Menard, 1981). In these models, the lithosphere behaves elastically until the yield stress is reached, at which point further increases in strain do not increase the stress (plastic behavior). Yield stress depends on temperature, overburden pressure, strain rate, and the sign of the stress (i.e. tension or compression). In contrast to the situation at subduction zones, the maximum bending stresses at FZ's are probably smaller than the yield stresses and purely elastic models of the bending should suffice. The most important rheological consideration for modelling of lithospheric flexure at FZ's is the increase of effective elastic thickness with age. Our attempts to match the observed flexural topography at FZ's with a constant  $h_e$  were not successful.

Our major conclusions are as follows:

- 1) There is no slip on the fossil fault planes of the Mendocino and Pioneer FZ's. The bathymetric steps on these FZ's are constant with age and equal to the initial vertical offsets at the ridge - transform fault - FZ intersections.

- 2) As a consequence of the frozen-in scarp and the differential subsidence of lithosphere far from the FZ, the lithosphere bends in the vicinity of the FZ. This flexure results in a characteristic ridge-trough topographic signature. The flexural amplitude, which is the difference between the scarp height and the overall change in depth across the FZ, increases with age.
- 3) Good fits to the bathymetric profiles across the Mendocino and Pioneer FZ's can be obtained by modelling the topography as the flexure of a thin elastic plate with an age-dependent effective elastic thickness.
- 4) Results of the modelling indicate that the base of the elastic lithosphere is approximately defined by the 450°C isotherm. Maximum bending stresses are on the order of 100 MPa, substantially less than the stresses encountered at subduction zones.
- 5) Because the separation of the Mendocino and Pioneer FZ's is less than a flexural wavelength there is elastic coupling between them.

APPENDIX A: TEMPERATURES IN THE VICINITY OF A FRACTURE ZONE

The two-dimensional thermal structure near a FZ is found by solving the time-dependent heat conduction equation

$$\frac{\partial^2 T}{\partial x^2} + \frac{\partial^2 T}{\partial z^2} = \frac{1}{\kappa} \frac{\partial T}{\partial t} \quad , \quad (A1)$$

where  $z$  is depth and  $x$  is distance from the fossil transform fault. The initial temperature distribution  $T(x, z, t_{A'})$  is that appropriate to the lithosphere lying beneath  $A - A'$  in Fig. 1 (Louden and Forsyth, 1976)

$$T(x, z, t_{A'}) = \begin{cases} T_m & , \quad x < 0 \\ T_s + (T_m - T_s) \operatorname{erf}\left(\frac{z}{2(\kappa t_{A'})^{1/2}}\right) & , \quad x > 0 \end{cases} \quad (A2)$$

The boundary condition is

$$T(x, 0, t) = T_s \quad . \quad (A3)$$

The solution to this problem for an arbitrary initial temperature distribution can be expressed as a two-dimensional convolution of the initial temperature with a line source Green's function

$$T'(x, z, t) = \int_0^\infty \int_{-\infty}^\infty T'(x_0, z_0, t_{A'}) G(x - x_0, z - z_0, t - t_{A'}) dx_0 dz_0 \quad , \quad (A4)$$

where  $T' \equiv T - T_s$  and the Green's function is (Carslaw and Jaeger, 1959)

$$G(x - x_0, z - z_0, t - t_{A'}) = \frac{1}{4\pi\kappa(t - t_{A'})} \left\{ \exp \left[ - \left( (x - x_0)^2 + (z - z_0)^2 \right) / 4\kappa(t - t_{A'}) \right] - \exp \left[ - \left( (x - x_0)^2 + (z + z_0)^2 \right) / 4\kappa(t - t_{A'}) \right] \right\} \quad . \quad (A5)$$



After inserting (A2) into (A4) and integrating over  $x_0$  and  $z_0$  we find

$$T'(x,z,t) = \frac{(T_m - T_s)}{2} \left[ \operatorname{erfc}\left(\frac{x}{2(\kappa(t - t_{A'}))^{1/2}}\right) \operatorname{erf}\left(\frac{z}{2(\kappa(t - t_{A'}))^{1/2}}\right) + \operatorname{erfc}\left(\frac{-x}{2(\kappa(t - t_{A'}))^{1/2}}\right) \operatorname{erf}\left(\frac{z}{2(\kappa t)^{1/2}}\right) \right], \quad (\text{A6})$$

where  $t - t_{A'}$  is the age of the lithosphere on the younger side of the FZ and  $t$  is the age on the older side. The actual temperature is obtained by adding  $T_s$  to  $T'$ .

#### ACKNOWLEDGMENTS

We thank Jacqueline Mammerickx for providing the bathymetric data. This research was supported by the NASA Geodynamics program under grant NAG 5152.

## Appendix B: A Method for Determining the Solution Coefficients

The general solution to the flexure problem where  $N+1$  segments of lithosphere are separated by  $N$  fracture zones is

$$w_i(x) = e^{-R_i x} (a_i \sin(R_i x) + b_i \cos(R_i x)) + e^{R_i x} (c_i \sin(R_i x) + d_i \cos(R_i x)) \quad (\text{B-1})$$

for  $x_i < x < x_{i+1}$ , where  $R_i = 2\pi/\lambda_i$ ,  $\lambda_i$  is the age dependent flexural wavelength, and  $x_i$  is the location of the  $i^{\text{th}}$  fracture zone.

The  $4N$  unknown coefficients are determined from the 4 matching conditions at each of the  $N$  FZ's (equations (12), (13), (14) and (15)). This appendix describes the details of this calculation. The notation is simplified by letting

$$\vec{\xi}_i = [a_i, b_i, c_i, d_i]^T \quad (\text{B-2})$$

and

$$\vec{f}(x) = [e^{-x} \sin(x), e^{-x} \cos(x), e^x \sin(x), e^x \cos(x)] \quad (\text{B-3})$$

Thus, the flexural topography is

$$w_i(x) = \vec{f}(R_i x) \cdot \vec{\xi}_i \quad (\text{B-4})$$

Similarly, the  $j^{\text{th}}$  derivative of  $w_i$  is

$$\frac{d^j w_i}{dx^j} = R_i^j ( \vec{\xi}_i \cdot \frac{d^j \vec{f}}{dx^j}(R_i x) ) \quad . \quad (B-5)$$

From  $\vec{f}$  and its first three derivatives, we form the following matrix

$$\begin{bmatrix} \vec{f}(x) \\ \vec{f}'(x) \\ \vec{f}''(x) \\ \vec{f}'''(x) \end{bmatrix} = \begin{bmatrix} e^{-x} \sin & , e^{-x} \cos & , e^x \sin & , e^x \cos \\ e^{-x}(\cos-\sin) & , -e^{-x}(\cos+\sin) & , e^x(\cos+\sin) & , e^x(\cos-\sin) \\ -2e^{-x} \cos & , 2e^{-x} \sin & , 2e^x \cos & , -2e^x \sin \\ 2e^{-x}(\cos+\sin) & , 2e^{-x}(\cos-\sin) & , 2e^x(\cos-\sin) & , -2e^x(\cos+\sin) \end{bmatrix} \quad (B-6)$$

where the primes denote differentiation with respect to  $x$  and the arguments of all of the sine and cosine functions are  $x$ . To simplify the notation further we'll define the  $\underline{\underline{F}}_i(R_i x)$  matrix as

$$\underline{\underline{F}}_i(R_i x) = \begin{bmatrix} \vec{f}(R_i x) \\ R_i \vec{f}'(R_i x) \\ -D_i R_i^2 \vec{f}''(R_i x) \\ -D_i R_i^3 \vec{f}'''(R_i x) \end{bmatrix} \quad (B-7)$$

where  $D_i$  is the flexural rigidity for the  $i^{\text{th}}$  segment of lithosphere. The right side of the matching conditions (12), (13), (14), and (15) is a vector  $\vec{\delta}_i = [ \delta_i, 0, 0, 0 ]^T$ , where  $\delta_i$  is the discontin-

unity in the topography across the  $i^{\text{th}}$  FZ as shown in Figure 5.

Consider two lithospheric segments that are offset at a single FZ. The matching conditions are

$$\left[ \underline{F}_1(R_1 x_1), \underline{F}_2(R_2 x_1) \right] \begin{bmatrix} \vec{\xi}_1 \\ \vec{\xi}_2 \end{bmatrix} = \left[ \vec{\delta}_1 \right] \quad . \quad (\text{B-8})$$

However, to satisfy the boundary conditions that  $w$  and its derivatives vanish as  $x \rightarrow \pm \infty$ , the coefficients  $a_1$ ,  $b_1$ ,  $c_2$ , and  $d_2$  must be zero. These boundary conditions are implemented by eliminating the first two and last two columns of the matrix containing the  $\underline{F}_i$  submatrices. We'll denote this operation by  $[ ]^{j-4}$ . Similarly, the first two and the last two elements of the vector containing the subvectors  $\vec{\xi}$  (denoted by  $[ ]^{i-4}$ ). Thus, the boundary conditions reduce (B-8) to a system of 4 equations in 4 unknowns.

When the model is composed of  $N$  fracture zones, separated by  $N+1$  lithospheric segments, the coefficients are determined from the solution of

$$\begin{bmatrix} \underline{F}_1(R_1 x_1), -\underline{F}_2(R_2 x_1), 0 & \dots & 0 & , & 0 \\ 0 & , \underline{F}_2(R_2 x_2), -\underline{F}_3(R_3 x_2), & \dots & 0 & , & 0 \\ \vdots & \vdots & \vdots & \vdots & \vdots & \vdots \\ \vdots & \vdots & \vdots & \vdots & \vdots & \vdots \\ 0 & , & 0 & , & 0 & \dots & \underline{F}_N(R_N x_N), -\underline{F}_{N+1}(R_{N+1} x_N) \end{bmatrix} \begin{bmatrix} \vec{\xi}_1 \\ \vec{\xi}_2 \\ \vdots \\ \vec{\xi}_N \end{bmatrix} =$$

$$\begin{bmatrix} \overset{\rightarrow}{\delta}_1 \\ \overset{\rightarrow}{\delta}_2 \\ \cdot \\ \cdot \\ \overset{\rightarrow}{\delta}_N \end{bmatrix} \quad (B-9)$$

which is a matrix problem of the form

$$\underline{\underline{A}} \underline{\Xi} = \underline{\Delta} \quad (B-10)$$

where  $\underline{\underline{A}}$  is an  $N \times N$  matrix,  $\underline{\Xi}$  is the  $N$ -element vector of unknown coefficients, and  $\underline{\Delta}$  is the  $N$ -vector of known coefficients. The solution is

$$\underline{\Xi} = \underline{\underline{A}}^{-1} \underline{\Delta} \quad (B-11)$$

In theory, the solution is unique. Considering the finite computer precision, however, the  $\underline{\underline{A}}$  matrix may be singular; in this case a unique solution does not exist. This occurs when the spacing between two adjacent FZ's is much greater than the flexural wavelength of the segment of lithosphere lying between them (i.e. the two FZ's are not elastically coupled). To avoid this numerical problem, the singular  $\underline{\underline{A}}$  matrix should be separated into two nonsingular matrices at the row and column corresponding to the segment of lithosphere that does not transmit significant flexural stresses.

## Appendix B: Time Dependence

In our model, the coefficients of the flexural topography are actually time dependent since the topographic discontinuity at each FZ increases with the age of the FZ according to (4) and the flexural wavelength is a function of the age of the lithosphere (equation (6)). To account for this time dependence, we have taken the time derivative of the flexure differential equation (10) and the matching conditions (12), (13), (14), and (15). We then solve for the flexural velocity  $v = \partial w / \partial t$  at 1 Myr time increments using the methods described in the first portion of this appendix. The flexural topography is the integral of the flexural velocity from zero to the age of the FZ

$$w(x,t) = \int_0^t v(x,t_0) dt_0 \quad . \quad (B-12)$$

In practice, (B-12) was evaluated using the trapezoidal integration scheme. A closer examination shows that we have not simply taken the derivatives of the differential equations and the matching conditions; we have also discarded a number of terms. The time derivative of (10) is actually

$$\frac{\partial D}{\partial t} \frac{\partial^4 w}{\partial x^4} + D \frac{\partial^5 w}{\partial t \partial x^4} + g(\rho_m - \rho_w) \frac{\partial w}{\partial t} \quad . \quad (B-13)$$

Similarly, the time derivatives of the matching conditions contain

additional terms with the factor  $\partial D/\partial t$ . These terms not only make the entire problem much more complex, but also introduce processes which are not characteristic of the earth. Consider a lithosphere that was flexed at time  $t_0$  by an amount  $w(t_0)$ . For the moment assume that the forces maintaining the flexure remain constant with time. There are two ways to increase the flexural rigidity. First, a flat unstressed elastic plate can be added to the base of the existing elastic layer. In this circumstance, the original flexural topography decreases because the second elastic layer must be stressed to conform to the curvature of the initial elastic layer. The final flexural topography is determined by solving (B-13), which contains the term that we have discarded. In the second method of increasing the flexural rigidity, an unstressed plate is added to the base of the initial elastic layer. This time, however, the second plate is formed so that it conforms to the curvature of the initial plate without being stressed. The original flexural topography  $w(t_0)$  remains unchanged although when an additional load is placed upon the lithosphere, it must flex both elastic layers. In our model, we assume that the flexural rigidity of the lithosphere increases with age as material continually "freezes" and conforms to the base of the existing elastic layer. Thus we discard the terms containing  $\partial D/\partial t$ .

## REFERENCES

- Atwater, T., and H.W. Menard, Magnetic lineations in the northeast Pacific, Earth Planet. Sci. Lett., 7, 445-450, 1970.
- Banks, R.J., R.L. Parker, and J.P. Huestis, Isostatic compensation on a continental scale: Local versus regional mechanisms, Geophys. J. Roy. Astron. Soc., 51, 431-452, 1977.
- Barazangi, M. and J. Dorman, World seismicity map of ESSA Coast and Geodetic Survey epicenter data for 1961-1967, Bull. Seism. Soc. Am., 59, 369-376, 1969.
- Bodine, J.H., M.S. Steckler, and A.B. Watts, Observations of flexure and the rheology of the oceanic lithosphere, J. Geophys. Res., 86, 3695-3707, 1981.
- Brune, J.M., Seismic moment, seismicity, and rate of slip along major fault zones, J. Geophys. Res., 73, 777-785, 1968.
- Caldwell, J.G., W.F. Haxby, D.E. Karig, and D.L. Turcotte, On the applicability of a universal elastic trench profile, Earth Planet. Sci. Lett., 31, 239-246, 1976.
- Caldwell, J.G., and D.L. Turcotte, Dependence of the thickness of the elastic oceanic lithosphere on age, J. Geophys. Res., 84, 7572-7576, 1979.
- Carslaw, H.S., and J.C. Jaeger, Conduction of Heat in Solids, 510 pp., Oxford University Press, New York, 1959.
- Chapple, W.M., and D.W. Forsyth, Earthquakes and bending of plates at trenches, J. Geophys. Res., 84, 6729-6749, 1979.
- Davis, E.E., and C.R.B. Lister, Fundamentals of ridgecrest topography, Earth Planet. Sci. Lett., 21, 405-413, 1974.
- DeLong, S.E., J.F. Dewey, and P.J. Fox, Displacement history of oceanic fracture zones, Geol., 5, 199-202, 1977.
- Forsyth, D.W., Comparison of mechanical models of the oceanic lithosphere, J. Geophys. Res., 85, 6364-6368, 1980.



- Forsyth, D., and H. Rowlett, Microearthquakes and recent faulting at the intersection of the Vema Fracture Zone and the Mid-Atlantic Ridge (abstract), EOS Trans. AGU, 60, 376, 1979.
- Francis, T.J.G., I.T. Porter, and R.C. Lilwall, Microearthquakes near the eastern end of the St. Paul's Fracture Zone, Geophys. J. Roy. Astron. Soc., 53, 201-217, 1978.
- Gunn, R., A quantitative study of mountain building on an unsymmetrical earth, J. Franklin Inst., 244, 19-53, 1937.
- Gunn, R., A quantitative study of isobaric equilibrium and gravity anomalies in the Hawaiian Islands, J. Franklin Inst., 236, 373-390, 1943.
- Gunn, R., Quantitative aspects of juxtaposed ocean deeps, mountain chains, and volcanic ranges, Geophys., 12, 238-255, 1947.
- Hanks, T.C., The Kuril Trench-Hokkaido rise system: Large shallow earthquakes and simple models of deformation, Geophys. J. Roy. Astron. Soc., 23, 173-189, 1971.
- Haskell, N.A., The dispersion of surface waves on multilayered media, Bull. Seism. Soc. Am., 43, 17-34, 1953.
- Kirby, S.H., Tectonic stresses in the lithosphere: Constraints provided by the experimental deformation of rocks, J. Geophys. Res., 85, 6353-6363, 1980.
- Louden, K.E., and D.W. Forsyth, Thermal conduction across fracture zones and the gravitational edge effect, J. Geophys. Res., 81, 4869-4874, 1976.
- Mammerickx, J., Depth anomalies over Mesozoic crust in the Western Pacific, (preprint), 1981.
- Mammerickx, J., and S.M. Smith, Bathymetry of the Northeast Pacific, Geol. Soc. of Am. Map and Chart Series, in press, 1981.
- McAdoo, D.C., J.G. Caldwell, and D.L. Turcotte, On the elastic-perfectly plastic

- bending of the lithosphere under generalized loading with application to the Kurile Trench, Geophys. J. Roy. Astron. Soc., 54, 11-26, 1978.
- McNutt, M., Compensation of oceanic topography: An application of the response function technique to the Surveyor area, J. Geophys. Res., 84, 7589-7598, 1979.
- McNutt, M.K., and H.W. Menard, Constraints on yield strength in the oceanic lithosphere derived from observations of flexure, (preprint), 1981.
- Menard, H.W., and T. Atwater, Origin of fracture zone topography, Nature, 222, 1037-1040, 1969.
- Ness, G., S. Levi, and R. Couch, Marine magnetic anomaly timescales for the Cenozoic and late Cretaceous: A précis, critique, and synthesis, Rev. Geophys. Space Phys., 18, 753-770, 1980.
- Okal, E.A., J. Talandier, K.A. Sverdrup, and T.H. Jordan, Seismicity and tectonic stresses in the south-central Pacific, J. Geophys. Res., 85, 6479-6495, 1980.
- Oxburgh, E.R., and D.L. Turcotte, Mechanisms of continental drift, Rep. Prog. Phys., 41, 1249-1312, 1978.
- Parsons, B., and P. Molnar, The origin of outer topographic rises associated with trenches, Geophys. J. Roy. Astron. Soc., 45, 707-712, 1976.
- Parsons, B., and J.G. Sclater, An analysis of the variation of ocean floor bathymetry and heat flow with age, J. Geophys. Res., 82, 803-827, 1977.
- Reid, I., The Rivera plate: A study of seismology and plate tectonics, Ph.D. thesis, 288 pp., Univ. of Calif., San Diego, 1976.
- Rowlett, I., Seismicity at intersections of spreading centers and transform faults, J. Geophys. Res., 86, 3815-3820, 1981.
- Sibuet, J.-Cl., and J. Mascle, Plate kinematic implications of Atlantic equatorial fracture zone trends, J. Geophys. Res., 83, 3401-3421, 1978.

- Turcotte, D.L., Flexure, Adv. in Geophys., 21, 51-86, 1979.
- Turcotte, D.L., D.C. McAdoo, and J.G. Caldwell, An elastic-perfectly plastic analysis of the bending of the lithosphere at a trench, Tectonophys., 47, 193-206, 1978.
- Walcott, R.I., Flexure of the lithosphere at Hawaii, Tectonophys., 9, 435-446, 1970.
- Watts, A.B., An analysis of isostasy in the world's oceans, 1. Hawaiian-Emperor seamount chain, J. Geophys. Res., 83, 5989-6004, 1978.
- Watts, A.B., J.H. Bodine, and M.S. Steckler, Observations of flexure and the state of stress in the oceanic lithosphere, J. Geophys. Res., 85, 6369-6376, 1980.
- Watts, A.B., and J.R. Cochran, Gravity anomalies and flexure of the lithosphere along the Hawaiian-Emperor seamount chain, Geophys. J. Roy. Astron. Soc., 38, 119-141, 1974.
- Watts, A.B., and M. Talwani, Gravity anomalies seaward of deep sea trenches and their tectonic implications, Geophys. J. Roy. Astron. Soc., 36, 57-90, 1974.

CHAPTER 3  
THERMAL SWELLS

## A Compensation Mechanism for the Central Pacific

D. T. SANDWELL AND K. A. POEHLS<sup>1</sup>

*Department of Earth and Space Sciences, University of California, Los Angeles, California 90024*

Geos 3 derived geoid heights and sea floor topography were averaged into 256 square areas (203 km on a side) for a region in the central Pacific containing a large portion of the Hawaiian Island chain. The whole region is about 500 m shallower than normal sea floor of the same age. The major portion of the depth anomaly is the Hawaiian swell. Data were analyzed using a two-dimensional fast Fourier transform. A transfer function was computed to determine the part of the observed geoid height that is coherent and in phase with the topography. A number of compensation models were tested against this function. Of these models no single physically reasonable model was found to have an acceptable fit. Accordingly, two models were introduced, one compensating short-wavelength topography at a shallow depth (14 km) and the other compensating the longer wavelengths by a deep mechanism. Acceptable deep compensation models include Airy-Heiskanen type compensation at depths between 40 and 80 km. Using the transition wavelength between the two models (1100 km), an estimate is made of the amplitude and shape of the heat anomaly needed to uplift the Hawaiian swell. The peak of the anomaly has an amplitude of  $530 \text{ mW m}^{-2}$  and is located 275 km east of Hawaii.

### INTRODUCTION

The Hawaiian ridge appears to be a midplate feature that is not related to the sea floor spreading process. The topography, surrounding the volcanic islands, is characterized by a broad swell of 1000 to 2000-km width upon which are superimposed several rises and deeps. The deeps and rises have been explained as the flexural response of the lithosphere to loading by the island chain [Walcott, 1970]. The origin of the Hawaiian swell has not yet been adequately explained.

Numerous origins for the Hawaiian swell and Hawaiian-Emperor seamount chain have appeared in the literature. These include propagating lithospheric cracks [McDougall, 1971], deep mantle plumes [Wilson, 1963], shallow mantle plumes or heating anomalies [Shaw and Jackson, 1973; Shaw, 1973] and asthenospheric bumps [Menard, 1973]. The most popular of these hypotheses are those dealing with the thermal anomalies. Recently, Detrick and Crough [1978] presented evidence showing that gouyots along the Hawaiian-Emperor chain have subsided at a rate higher than the rate predicted by the empirical depth-age relation. They invoked a lithospheric thinning mechanism to explain both the Hawaiian swell and the increased subsidence rate of gouyots along the swell. This idea is, of course, consistent with the presence of a thermal anomaly.

In this study we analyze a region in the central Pacific containing a large portion of the Hawaiian chain. Our aim is to determine an average compensation mechanism for the sea floor topography at wavelengths between 300 and 3000 km. To accomplish this, a transfer function between geoid height and topography is computed. A number of compensation models are tested, and an acceptable class of models is found. An acceptable model must meet the following criteria: the model must fit the data, it must be physically reasonable, and it should be consistent with other geophysical observations.

When working with geoid or gravity data, many compensation models can be found that fit within the uncertainties in the data. Because of this, the class of models must be narrowed by requiring that they be physically reasonable.

We test the simplest models first and either accept or reject them before moving on to more complex models. By using this method the unacceptable aspects of the rejected models are clearly pointed out.

The current compensation models for the central Pacific are divided into two classes. Investigators who have looked at the relationship between gravity and topography at the longer wavelengths ( $>1000$  km) have found that compensation occurs at depths between 50 and 120 km [Watts, 1976; Detrick and Crough, 1978; Crough, 1978]. Watts [1978] has shown that the shorter wavelength topography ( $<600$  km), across the Hawaiian Emperor island chain, is supported by the strength of the lithosphere. Upon closer inspection, it is clear that neither model fits the data over the whole wavelength spectrum.

The data presented here cover both of these wavelength regimes. We show that there is no single, physically reasonable, compensation mechanism that fits the data at all wavelengths. We then introduce a more complex model with two competing compensation mechanisms, one dominating at shorter wavelengths and the other at longer wavelengths. Using these results, we reconsider the lithospheric thinning hypothesis. By modeling the lithosphere as a thermal boundary layer an estimate is made for the heat flow necessary to uplift the Hawaiian swell. A major purpose of this study is to demonstrate why two compensation mechanisms are necessary and to determine at what wavelength the transition occurs.

### DATA

The area investigated in this study is outlined in Figure 1. The main tectonic features included in this region are the Musicians seamounts, the Hawaiian island chain, the Hawaiian swell, the Necker ridge, the eastern part of the mid-Pacific mountains, the northern end of the Line islands, and a number of fracture zones. For the analysis technique used below, it was assumed that all of these major topographic features have the same wavelength-dependent compensation mechanism. To focus upon the compensation mechanism for the Hawaiian swell, the size of the region was chosen small enough so that the swell was the dominant tectonic feature at the longer wavelengths and large enough so that the topography power spectrum reached its peak at a wavelength shorter than the side length of the region. For analysis purposes the

<sup>1</sup> Now at Dynamics Technology, Inc., Torrance, California 90503.  
Copyright © 1980 by the American Geophysical Union.

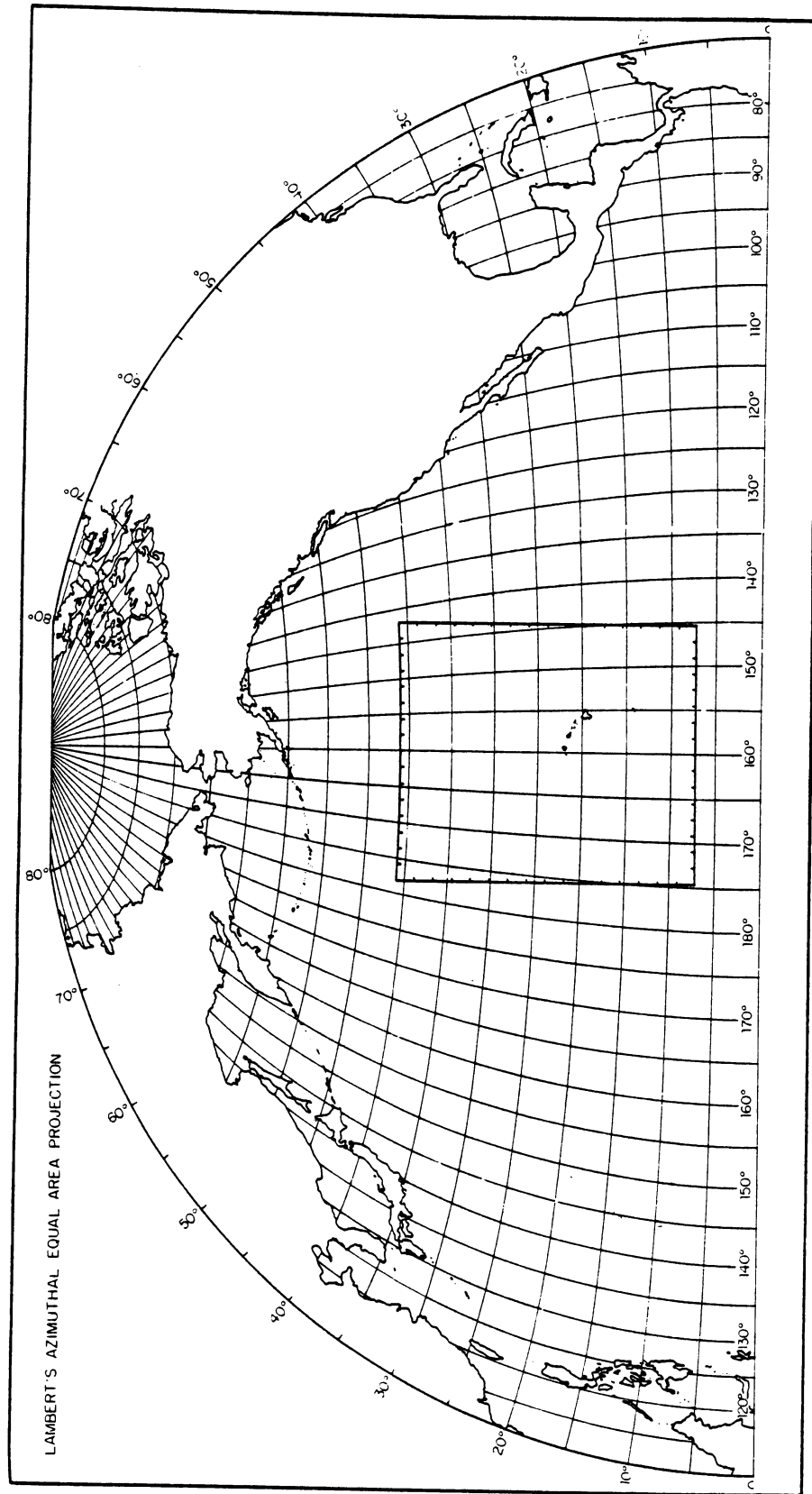


Fig. 1. Location map and outline of study area.

area was divided into 256 equal area squares with side length of 203 km (approximately  $2^\circ \times 2^\circ$ ). Geoid height and sea floor depth estimates for each square were obtained by graphically integrating over the area. A mean and best fitting plane were removed from each data set before a two-square taper was added to the perimeter.

**Bathymetry.** Sea floor bathymetry was taken from Chase *et al.* [1970] and was corrected for water velocity using Matthews tables [Matthews, 1939]. No sediment corrections were applied to the data because the sedimentary cover is regionally uniform [Ewing *et al.*, 1968] and the large averaging areas largely negate the influences of local accumulations. Figure 2 shows the results after averaging. The WNW striking island chain can clearly be seen. The deep and rise flanking the island chain do not show up after averaging because the box size is greater than the wavelength of these features. The Hawaiian swell shows up clearly with a strike similar to the island chain and a half width of about 1000 km. The swell is elongate on the north but drops sharply to the south at the southeast end of the chain. The mean depth of the region (5169 m) fits the empirical depth-age curve at about 60 m.y.; the magnetic age of the area is closer to 100 m.y.

**Geoid.** Sea surface heights measured by the Geos 3 altimeter were used in this study. The numerous individual satellite passes were processed in a way that minimized both orbital tracking errors and track crossing discrepancies [Brace, 1977]. The data were averaged into the same squares as the bathymetry (Figure 3). The dominant feature in the geoid is the long-wavelength high over the Hawaiian swell region with an amplitude of roughly 10 m. The central portion of this high has a feature elongated in the WNW direction. This feature probably reflects the part of the geoid produced by the island chain. The remainder of the high is roughly circular with a half width of about 1200 km in the N-S direction and about 1600 km in the E-W direction. The peak-to-trough amplitude in the E-W direction is about 12 m, and in the N-S direction it is only 10 m.

Geoid data were used in this analysis for a number of reasons. First, these data are best suited for studies at intermediate wavelengths. At the shorter wavelengths, geoid undulations have a low signal-to-noise ratio. At the longer

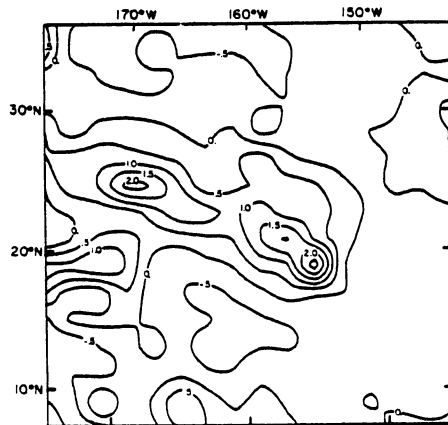


Fig. 2. Sea floor topography averaged into areas 203 km on a side with best-fitting plane removed. Map was made by contouring the digitized data. Contour units are in kilometers.

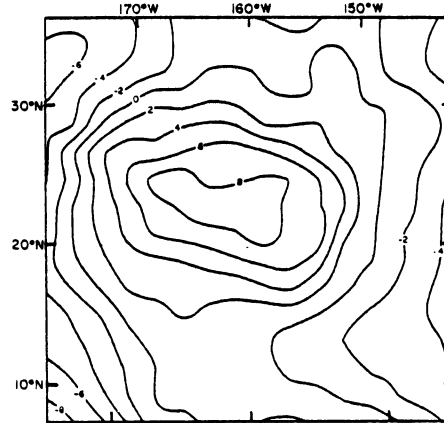


Fig. 3. Geoid heights (in meters) averaged into areas 203 km on a side with best fitting plane removed.

wavelengths (degree  $< 10$ ) the Geos 3 derived geoid may contain inaccuracies due to satellite tracking errors. The second reason these data were used is because Watts [1976] has used surface gravity data to infer the lithospheric and upper mantle density structure over a region roughly the same as that shown in Figure 1. Since the Geos 3 geoid and the surface gravity measurements are independent data sets, it is interesting to compare the results of the two analyses.

#### ESTIMATION OF THE TRANSFER FUNCTION

The transfer function is used to separate the observed geoid into two parts. Following the approach of Dorman and Lewis [1970], we write

$$N(\mathbf{k}) = Q(k)T(\mathbf{k}) + I(\mathbf{k}) \quad (1)$$

$N(\mathbf{k})$  is the two-dimensional Fourier transform of the geoid, and the quantity  $Q(k)T(\mathbf{k})$  is the part of the geoid that is linearly related to the Fourier transform of the topography  $T(\mathbf{k})$ .  $I(\mathbf{k})$  does not correlate, on the average, with the topography. By minimizing the sum of  $I(\mathbf{k})$  squared, the best estimate of the transfer function is

$$Q(k) = \text{Re} \left[ \frac{\langle NT^* \rangle}{\langle TT^* \rangle} \right] \quad (2)$$

The angle brackets denote averaging over an annulus in the wave number domain. In writing (2) it is assumed that the transfer function is linear, real, and isotropic. An estimate for the uncertainty in the transfer function is [McNutt, 1978]

$$\sigma^2(k) = \frac{1}{(2n-1)} \left[ \frac{\langle NN^* \rangle}{\langle TT^* \rangle} - Q^2 \right] \quad (3)$$

where  $n$  is the number of complex numbers within the averaging interval.

The Fourier transform of both the geoid and topography must be known in order to calculate the transfer function. To satisfy the sampling theorem, the short wavelengths were removed from each data set by averaging over equal area squares. The center of each box was assigned this average value. This averaging procedure introduces errors in the Fourier transform at short wavelengths but has a negligible effect upon the longer-wavelength part of the transform. Because of

TABLE 1. Estimates of the Transfer Function

Wave-length $\lambda$ , km	Transfer Function $Q$ , m/m $\times 10^{-3}$	Phase $\phi$	Coherence $\gamma^2$	Uncertainty $\sigma$ , m/m $\times 10^{-3}$	Transfer Function $Q$ , <sup>1</sup> mgal/km	Uncertainty $\sigma$ , mgal/km	Power Topography $TT^*$ , $m^2 \times 10^4$	Power Geoid $NN^*$ , $m^2$
3617	8.77	-6.1	0.270	7.28	14.9	12.4	1.72	5.98
2678	7.75	24.3	0.759	2.76	17.8	6.3	1.29	1.23
1860	4.93	-1.3	0.534	1.27	16.3	4.2	4.57	2.09
1314	3.54	11.3	0.309	1.08	16.6	5.0	3.52	1.48
935	0.25	69.9	0.011	1.02	1.7	6.6	1.36	0.66
669	0.82	-15.4	0.143	0.22	7.5	2.1	1.37	0.07
479	0.57	19.4	0.078	0.16	7.4	2.1	1.53	0.07
344	0.21	35.2	0.028	0.15	9.3	2.7	0.75	0.002

<sup>1</sup>The transfer function was converted from meters per meter to milligals per kilometer by multiplying by  $2\pi g/\lambda$ .

this averaging scheme the two shortest-wavelength estimates may be biased. A better method of removing the short wavelengths before taking the discrete Fourier transform is to use a smoother low-pass filter such as a Gaussian filter.

The results of the transfer function analysis are given in Table 1. About 40% of the power in the geoid is coherent and in phase with the topography. This part is shown in Figure 4. To facilitate comparison with past work, the transfer function was converted to a free air anomaly transfer function (Table 1) and a Bouguer anomaly transfer function (using density  $\rho_0$  of  $1800 \text{ kg m}^{-3}$ , Figure 5). If the region is isostatically compensated then the transfer function (Figure 5) approaches  $-2\pi G\rho_0$  as the wavelength goes to infinity and approaches zero as the wavelength goes to zero. The shape of the transfer function between these two extremes contains information about the compensation mechanism [Dorman and Lewis, 1972]. Figure 5 shows that the transfer function for the central Pacific makes an abrupt jump at a wavelength of about 1100 km.

COMPENSATION MODELS

It is well known that given the geoid height over the surface of the earth, the density anomalies causing the geoid undulations cannot be uniquely determined. This fact is clearly seen in the following equation, where the spherical harmonic coef-

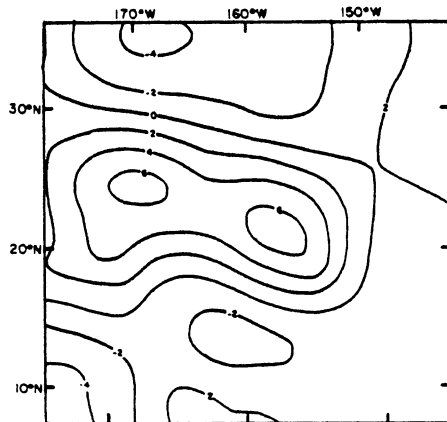


Fig. 4. The part of the observed geoid (in meters) that is coherent and phase with the topography.

ficients of the geoid  $N_{lm}$  are related to the coefficients of the density anomaly  $\Delta\rho_{lm}(r)$ :

$$N_{lm} = \frac{4\pi R^4}{M(2l+1)} \int_0^1 \mu^{l+2} \Delta\rho_{lm}(\mu R) d\mu \quad (4)$$

$R$  is the radius of the earth,  $\mu = r/R$  is the normalized radius, and  $M$  is the mass of the earth. Before (4) can be inverted, certain simplifying assumptions must be made about the earth. Lewis and Dorman [1970] observed that the relationship between Bouguer anomaly and topography in the wave number domain was nearly linear and isotropic. These observations led them to decompose the compensating density in the following way:

$$\Delta\rho_{lm}(r) = \rho(r, l) T_{lm} \quad (5)$$

Inserting (5) into (4) and dividing by the spherical harmonic coefficients of the topography  $T_{lm}$  we obtain

$$Q_l = \frac{4\pi R^4}{M(2l+1)} \int_0^1 \mu^{l+2} \rho(\mu R, l) d\mu \quad (6)$$

where  $Q_l$  is the transfer function and  $\rho(\mu R, l)$  is a Green function relating a point topographic load to its compensating density at some depth and degree. All local and regional compensation models can be represented by this Green function. These models include Pratt, Airy (to a linear approximation), and elastic plate models. For  $l = 0$ , equation (6) is just a statement of mass conservation. Notice that the function  $\rho(\mu R, l)$  is not a density but has units of mass per length to the fourth power and is a density per unit of topography.

INVERSION OF THE TRANSFER FUNCTION

Equation (6) is still not in a form with a unique inverse. To put it in this form, a compensation model must be introduced. The first model tested was the local compensation model. For this case, (6) reduces to a Fredholm integral equation of the first kind:

$$Q_l = \frac{4\pi R^4}{M(2l+1)} \int_0^1 \mu^{l+2} \rho(\mu R) d\mu \quad (7)$$

Inversion of this equation corresponds to downward continuation, which is a highly unstable process. Errors in the transfer function show up as wild oscillations in the compensation model unless the function is constrained to be smooth.

A spectral expansion technique was used to find a best fitting local compensation model [Parker, 1977]. The observed



transfer function was converted from  $Q(k)$  to  $Q_i$  so that a spherical geometry could be used for the inversion [Dorman and Lewis, 1970]. The compensation was constrained to be complete to a 7% uncertainty. Complete compensation is defined as

$$\rho_0 = -R \int_0^1 \rho(\mu R) d\mu \quad (8)$$

where  $\rho_0$  is the density of the topography relative to water ( $1800 \text{ kg m}^{-3}$ ). The spectral expansion technique uses a weighted sum of eigenfunctions to represent  $\rho(r)$ . By varying the number of eigenfunctions a trade-off is made between resolution of the model and misfit of the transfer function. Four eigenfunctions were used. The two-norm misfit between the observed and model transfer function is  $\chi^2 = 2.69$ . The model transfer function is plotted as a dashed line in Figure 5. It fits within the uncertainties in the data with an average misfit of 0.34 standard deviations.

The compensation model with associated uncertainties is plotted on Figure 6. One thousand kilometers was chosen as the maximum compensation depth. Starting from the surface, 126% of the compensation occurs less than 70 km, -92% of the compensation is between 70 km and 300 km, and the remaining 68% of the compensation is below 300 km. A -92% compensation in the upper mantle may seem physically unsatisfactory, but it is easy to see why this feature is necessary. A positive compensating density centered about a depth  $z_0$  causes the transfer function to be more positive at a wavelength of about  $2\pi z_0$ . Although the model has an acceptable fit to the data, we feel it should be rejected for two reasons. First, it is unlikely that these density contrasts could be maintained in the upper mantle for tens of millions of years. Second, positive compensating densities are not features of most compensation models, and there is no reasonable mechanism to explain them.

Since positive densities are physically undesirable, we proceed to see if there is a local compensation model, with only negative densities, that has an acceptable misfit. There are an infinite number of models within this class that could be

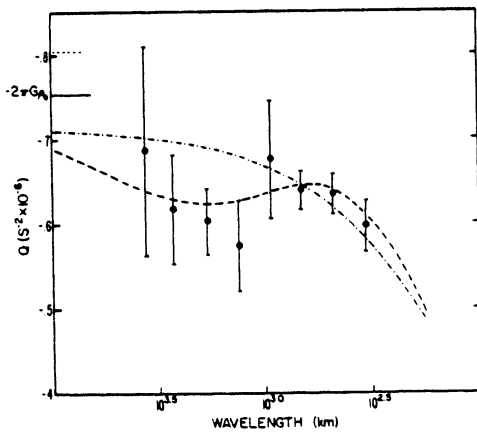


Fig. 5. Transfer function between Bouguer anomaly and topography. A density of  $1800 \text{ kg m}^{-3}$  was used to make the topographic correction. The dashed line is a model transfer function with positive and negative compensation; chain line is the best fitting model with only negative densities per unit topography.

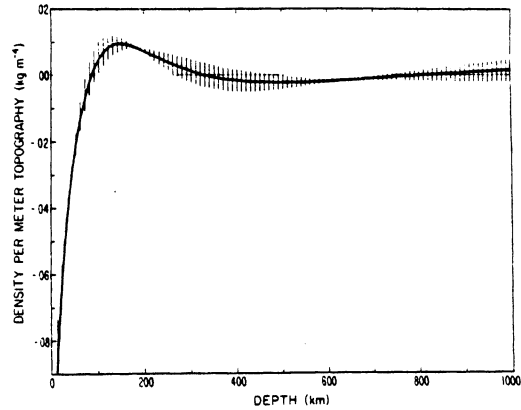


Fig. 6. Local compensation model represents the change in density per meter of topography. Uncertainties reflect the resolution of the model.

tested. For this reason the model with the smallest misfit must be found. The misfit of this model is used to calculate the probability that the observed transfer function deviates from the model by this misfit or larger. If the probability of this occurrence is low, then the model can be rejected at some confidence level. Since this model is the model with the smallest misfit, every other model of this type can also be rejected. This method of rejecting classes of models was used by Banks *et al.* [1977].

The best fitting, all negative model is most easily found by a linear programming algorithm. The details of solving the flat earth equivalent to (7) by a linear programming technique are described by Banks and Swan [1978]. For this inversion no constraint was placed upon the total amount of compensation. A maximum compensation depth of 1000 km was used. The best fitting model has all of its compensating density between the depths of 10 and 12.5 km. The compensation is 95% complete. The model transfer function is plotted as a chain line in Figure 5. The one-norm misfit is  $\gamma_m = 7.23$ . The fit to the data is good at the short wavelengths and is poor (more than one standard error) at wavelengths between 1000 and 2800 km.

From the misfit of the best fitting model the probability of exceeding this value with eight data is  $P(\gamma > \gamma_m, 8) = 0.285$ . The local compensation model with only negative densities can be rejected at the 72% confidence level.

Two classes of models were tested. The first was rejected because it requires an unphysical density structure in the upper mantle. The best fitting model from the second class is unacceptable because of its large misfit. Banks *et al.* [1977] reached this same conclusion when analyzing the transfer function for the continental United States. They interpreted this result as a need for a regional compensation mechanism. This model worked well for the continental U.S. data but is inappropriate for this case. For regional compensation, with positive density gradient,  $\partial Q/\partial k$  is greater than zero for all wave numbers. Our data requires  $\partial Q/\partial k$  to be less than zero over part of the wave number spectrum. What needs to be done is to reexamine the definition of local compensation to see if there is a more general class of models that can be tested.

Dorman and Lewis [1970] defined local compensation by stating that the compensating mass must lie directly beneath

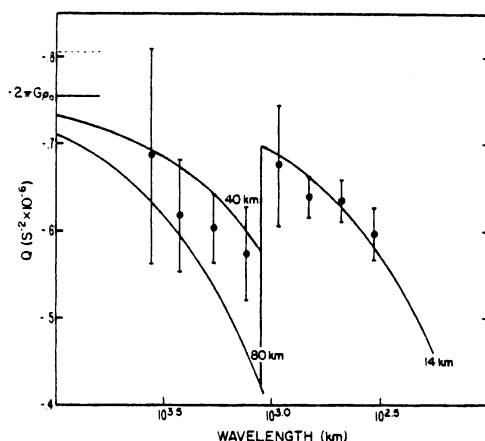


Fig. 7. Model transfer functions assuming linear, Airy-type compensation. Compensation depths are in kilometers. The vertical line corresponds to a wavelength of 1122 km.

the topographic load. Mathematically, they wrote

$$\Delta\rho(x', y', z') = \rho(z')t(x, y)\delta(x - x')\delta(y - y') \quad (9)$$

which relates the compensating density at the field point  $\Delta\rho(x', y', z')$  to the topographic load  $t(x, y)$  at the source point by a Green function of the form  $\rho(z)\delta(x - x')\delta(y - y')$ . Taking the Fourier transform of (9) in the  $x$  and  $y$  directions, we find

$$\Delta P(\mathbf{k}, z) = \rho(z)T(\mathbf{k}) \quad (10)$$

where capitals denote the Fourier transform of the function (e.g.  $\mathcal{F}_2[a(x, y, z)] = A(\mathbf{k}, z)$ ). The spherical equivalent of (10) was used to derive (7), and it encompasses both Pratt and Airy compensation models. The form of (9) implies that the local compensation mechanism is the same throughout the area. For the central Pacific this assumption is invalid. The data suggest that the shorter-wavelength topography is compensated at depths of 10–20 km, while the longer-wavelength loads are compensated much deeper. A way to fit the observed transfer function is to have one compensation mechanism  $\rho_1(z)$  for wavelengths greater than 1100 km and another mechanism  $\rho_2(z)$  for the shorter wavelengths. These ideas are represented by the following equation:

$$\Delta P(\mathbf{k}, z) = [\rho_1(z)H(k - k_0) + \rho_2(z)H(k_0 - k)]T(\mathbf{k}) \quad (11)$$

where  $H(k)$  is the Heavyside step function and  $k_0$  is some prescribed wave number. In the space domain, (11) represents a local compensation mechanism that is not constant throughout the region but varies horizontally, depending upon the spectral content of the topographic load.

This specific form of compensation was chosen because it allows acceptable fits to the data. Little or nothing is learned by determining the functions  $\rho_1(z)$  and  $\rho_2(z)$  with the best fitting transfer function. Figure 7 shows some examples of acceptable models. The solid lines are transfer functions for Airy compensation models with indicated compensation depths. For these models the compensation is complete. To calculate the longer-wavelength part of the transfer function, it is assumed that the lithosphere above the depth of compensation has a relative displacement equal to the long-wavelength topography. The density jump between the topographic density ( $2800 \text{ kg m}^{-3}$ ) and the lithospheric density

( $3300 \text{ kg m}^{-3}$ ) occurs at a depth of 14 km. Airy models with compensation depths between 40 and 80 km roughly bracket the uncertainties in the longer-wavelength data.

## DISCUSSION

We have found two negative density, local compensation models that fit the long- and short-wavelength parts of the observed transfer function. The data suggest that the division between the two should be placed at a wavelength of about 1100 km. For this model to be acceptable it must be shown that it is both physically reasonable and consistent with other geophysical observations. Since there is no mathematical model that will relate a mantle heat anomaly to both surface volcanism and swell formation, the physical reasonability of the proposed model cannot be clearly demonstrated. The best we can do is show that the model is not unreasonable. To do this, we present a very simple view of the tectonics in the area.

It is generally believed that the Hawaiian swell and the Hawaiian-Emperor seamount chain are the surface manifestations of the Pacific plate moving over a hot spot or mantle plume [Wilson, 1963]. By some poorly understood interaction between the plume and the moving plate a linear island chain is formed on the surface of the plate. The islands are composed of relatively young material and overlie a mature lithosphere. The compensation for the islands occurs at relatively shallow depths and is the result of volcanic loading [Watts, 1978]. For the swell the process is reversed. The broad swell in the topography is a result of its compensation. The two types of tectonic features are not separable in the space domain. Fortunately, partial separation is possible in the wave number domain. The separation is not complete because individual islands may contain a long-wavelength component. The observed transfer function has a rather abrupt jump at about 1100 km. This implies that either the swell dominates the amplitude spectrum for wavelengths greater than 1100 km or the long-wavelength part of individual islands has a deep compensation. There is no definite physical model that will explain a step in the observed transfer function, but a step is consistent with a very simplified picture of the tectonics in the central Pacific. It is also the most complex form of compensation that can be resolved by the data.

If the correct compensation model was chosen, then the results indicate that the deep compensating body contains very little power at wavelengths shorter than 1100 km. This sets a lower limit on the wavelengths of the heat source and/or pressure causing the swell.

If lithospheric reheating is the source of the swell compensation, then there is a simple way to estimate the strength and extent of the heat source from the topography. To derive this expression, a number of assumption must be made: (1) the lithosphere acts as a thermal boundary layer, (2) density anomalies result from thermal expansion, and (3) the lithosphere is isostatically supported. By requiring energy conservation and imposing these assumptions the following equation can be derived:

$$\frac{\partial d}{\partial t} + \mathbf{v} \cdot \nabla d = \frac{-\alpha}{C_p(\rho_m - \rho_w)}(q_\infty - q_s) \quad (12)$$

where  $d$  is the ocean depth,  $\mathbf{v}$  is the velocity vector of the plate relative to the heat anomaly [Minster and Jordan, 1978],  $\alpha$  is the coefficient of thermal expansion ( $3.5 \times 10^{-5} \text{ }^\circ\text{C}^{-1}$ ),  $C_p$  is the heat capacity ( $1050 \text{ J kg}^{-1} \text{ }^\circ\text{C}^{-1}$ ),  $\rho_m$  is the lithospheric den-

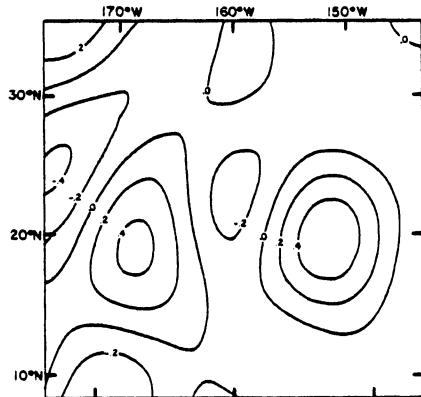


Fig. 8. Contour map of  $q_{\infty} - q_s$  in watts per square meter.

sity ( $3300 \text{ kg m}^{-3}$ ),  $\rho_m$  is the density of seawater ( $1025 \text{ kg m}^{-3}$ ),  $q_{\infty}$  is the heat flow into the base of the lithosphere, and  $q_s$  is the surface heat flow. This equation was derived in a one-dimensional form by Parsons and McKenzie [1978]. If  $\partial d/\partial t = 0$  and  $v$  is constant in time, then  $q_{\infty} - q_s$  can be determined. From the transfer function analysis we found that the longer-wavelength ( $\lambda > 1100 \text{ km}$ ) topography was compensated by a deep mechanism. Using only this part of the topography in (12), an estimate is made of the amplitude and shape of the heat anomaly needed to uplift the Hawaiian swell.

Figure 8 shows a contour map of  $q_{\infty} - q_s$ . As expected, a nearly circular heat anomaly is needed to uplift the swell. There are many other features on the map that are unexpected and indicate a failure of this model. This model predicts that the longer-wavelength topography associated with the mid-Pacific mountains is currently being uplifted by a large heat anomaly. This is clearly incorrect. Many of the other longer-wavelength features away from the southeast end of the Hawaiian swell may have originated differently and at an earlier time than the swell. Since the time-dependent term was neglected in (12), the results are only valid for tectonic features with ages less than the time since the heat anomaly or velocity vector has changed significantly.

Detrick and Crough [1978] estimated that 40 times the normal surface heat flux is necessary to match the uplift rate at the S-E end of the swell. Using topographic wavelengths greater than 1100 km, we find a peak of  $530 \text{ mW m}^{-2}$  (13 heat flux units), and an average of  $400 \text{ mW m}^{-2}$  is needed. Using wavelength greater than 800 km, a peak of  $550 \text{ mW m}^{-2}$  is required. The width of the heat anomaly parallel to the velocity vector is about 1000 km, corresponding to a total heating time of 11 m.y. In writing (12) no heat transfer process was specified. Crough [1978] found that to fit the island subsidence data, the surface heat flux must rise from  $45 \text{ mW m}^{-2}$  to a peak of  $70 \text{ mW m}^{-2}$  over a time interval of 5 m.y. This implies that much of the heat needed to uplift the swell must be placed in the lithosphere at depths of about 40 km. Transferring the required amount of heat from the upper mantle to relatively shallow depths over an 11-m.y. period is a major problem with the lithospheric thinning hypothesis. We agree with Detrick and Crough [1978] that this mechanism cannot be conductive transport but must be some sort of rapid intrusion process.

As an alternative to the lithospheric reheating model, the

Hawaiian swell could be supported by pressure exerted on the base of the lithosphere. This implies that a rising plume of material is supporting the swell. The compensation for this type of model is the low-density material in the rising plume at depths greater than 80 km. The mass deficiency in the plume is somewhat greater than the mass excess in the swell, since the low-density material must maintain both the flow pattern and the swell. For certain convection models the transfer function will look very similar to our observed transfer function [McKenzie, 1977].

By obtaining more longer-wavelength estimates of the transfer function we do not believe it will be possible to discriminate between the two models. The island subsidence data seem to indicate that the lithospheric thinning hypothesis is correct because it is difficult to conceive of a convection pattern that could support the islands along the Hawaiian-Emperor chain in the observed fashion.

#### CONCLUSIONS

Geoid heights and sea floor topography from the central Pacific were used to calculate a linear, isotropic transfer function in the wave number domain. A number of compensation models were tested to determine a class of acceptable models. A local compensation model with positive and negative compensating densities has a statistically good fit to the data. It was found to be unacceptable because it required a physically unreasonable density structure. The next model tested was constrained to have only negative compensating densities. The best fitting model is Airy compensation at a depth of 11 km. This model was also rejected because of a poor fit to the observed transfer function at wavelengths between 1000 and 3000 km. Since the Hawaiian swell has most of its power in this wavelength band, a local compensation model was proposed with compensation depending upon wave number. The shorter-wavelength data were insufficient to discriminate between local and regional compensation models. An Airy model with a 14-km depth of compensation fit within the uncertainties in the data. At the longer wavelengths, Airy compensation with depths between 40 and 80 km bracket the data. Some convection models [McKenzie, 1977] are consistent with the long-wavelength part of the observed transfer function. If the lithospheric thinning hypothesis is correct, then a heating anomaly with radius of about 600 km and a peak of  $530 \text{ mW m}^{-2}$  is required to fit the longer-wavelength ( $\lambda > 1100 \text{ km}$ ) topography.

*Acknowledgements.* We thank William Kaula and Leroy Dorman for their helpful suggestions and encouragement. Also the critical comments of the reviewers enabled us to make many beneficial changes in the original manuscript. This work was supported by NASA contract grant NGL 05-007-002 at the Department of Earth and Space Sciences, UCLA.

#### REFERENCES

- Banks, R. J., and C. J. Swan. The isostatic compensation of east Africa, *Proc. Roy. Soc. London*, 364, 331-352, 1978.
- Banks, R. J., R. L. Parker, and S. P. Huestis. Isostatic compensation on a continental scale: Local versus regional mechanisms, *Geophys. J. Roy. Astron. Soc.*, 51, 431-452, 1977.
- Brace, K. L. Preliminary ocean-area geoid from Geos-3 satellite radar altimetry, report, Def. Mapp. Agency, Aerosp. Center, St. Louis Air Force Station, Mo., 1977.
- Chase, T. E., H. W. Menard, and J. Mamerickx. Bathymetry of the north Pacific, report, Inst. of Marine Resour., La Jolla, Calif., 1970.
- Crough, S. T. Thermal origin of mid-plate hot-spot swells, *Geophys. J. Roy. Astron. Soc.*, 55, 451-469, 1978.

- Detrick, R. S., and S. T. Crough, Island subsidence, hot spots, and lithospheric thinning, *J. Geophys. Res.*, **83**, 1236-1244, 1978.
- Dorman, L. M., and B. T. R. Lewis, Experimental isostasy, 1, Theory of the determination of the earth's isostatic response to a concentrated load, *J. Geophys. Res.*, **75**, 3357-3365, 1970.
- Dorman, L. M., and B. T. R. Lewis, Experimental isostasy, 3, Inversion of the isostatic Green function and lateral density changes, *J. Geophys. Res.*, **77**, 3068-3077, 1972.
- Ewing, J., M. Ewing, T. Actken, and W. J. Ludwig, North Pacific sediment layers measures by seismic profiling, in *The Crust and Upper Mantle of the Pacific Area*, *Geophys. Monogr. Ser.*, vol. 12, edited by L. Knopoff et al., AGU, Washington, D. C., 1968.
- Lewis, B. T. R., and L. M. Dorman, Experimental isostasy, 2, An isostatic model for the U.S.A. derived from gravity and topographic data, *J. Geophys. Res.*, **75**, 3367-3386, 1970.
- Matthews, C. J., Tables of the velocity of sound in pure water and sea water for use in echo-sounding and sound-ranging, *Rep. H.D. 282*, 52 pp., Hydrogr. Dep., Admiralty Office, London, 1939.
- McDougall, I., Volcanic island chains and seafloor spreading, *Nature*, **231**, 141-144, 1971.
- McKenzie, D. P., Surface deformation, gravity anomalies and convection, *Geophys. J. Roy. Astron. Soc.*, **48**, 211-238, 1977.
- McNutt, M. K., Continental and oceanic isostasy, Ph.D. thesis, 192 pp., Univ. of Calif., San Diego, 1978.
- Menard, H. W., Depth anomalies and the bobbing motion of drifting islands, *J. Geophys. Res.*, **78**, 5128-5138, 1973.
- Minster, J. B., and T. H. Jordan, Present-day plate motions, *J. Geophys. Res.*, **83**, 5331-5350, 1978.
- Parker, R. L., Understanding inverse theory, *Rev. Earth Planet. Sci.*, **5**, 35-64, 1977.
- Parsons, B., and D. P. McKenzie, Mantle convection and the thermal structure of the plates, *J. Geophys. Res.*, **83**, 4485-4495, 1978.
- Shaw, H. R., Mantle convection and volcanic periodicity in the Pacific: Evidence from Hawaii, *Geol. Soc. Amer. Bull.*, **84**, 1505-1526, 1973.
- Shaw, H. R., and E. D. Jackson, Linear island chains in the Pacific: Result of thermal plumes or gravitational anchors?, *J. Geophys. Res.*, **78**, 8634-8652, 1973.
- Walcott, R. I., Flexure of the lithosphere at Hawaii, *Tectonophysics*, **9**, 435-446, 1970.
- Watts, A. B., Gravity and bathymetry in the central Pacific Ocean, *J. Geophys. Res.*, **81**, 1533-1553, 1976.
- Watts, A. B., An analysis of isostasy in the world's oceans, 1, Hawaiian-Emperor seamount chain, *J. Geophys. Res.*, **83**, 5989-6003, 1978.
- Wilson, J. T., Evidence from islands on the spreading of ocean flows, *Nature*, **197**, 536-538, 1963.

(Received December 8, 1978;  
revised September 17, 1979;  
accepted January 14, 1980.)

## Appendix A. Derivation of Equation 12

In this appendix we present a derivation of equation 12. This equation provides a model-independent method for estimating the difference between the heat flow into the base of the lithosphere  $q_\ell$  and the surface heat flow  $q_s$  by using observed bathymetric data. As was stated previously, (12) is based upon three major assumptions which are: 1) The lithosphere is a thermal boundary layer. 2) Density anomalies are linearly related to temperature by the coefficient of thermal expansion  $\alpha$ . 3) The lithosphere is in local isostatic equilibrium.

Consider a lithosphere, with a thickness  $\ell$  and infinite horizontal dimensions, moving across the mantle at a velocity  $\vec{v} = (v_x, v_y)$ . Let  $T(x, y, z, t)$  be the temperature of the lithosphere which satisfies boundary conditions at the top and the base of the lithosphere ( $z$  is measured positive downward). This temperature can be decomposed into a steady-state reference geotherm  $T_{\text{ref}}(z)$  and a temperature perturbation  $\theta(x, y, z, t)$ . The temperature perturbation must satisfy the energy conservation equation

$$\rho_m C_p \left( \frac{\partial \theta}{\partial t} + \vec{v} \cdot \nabla \theta \right) = k \nabla^2 \theta \quad (\text{A-1})$$

where  $\rho_m$  is the mantle density,  $C_p$  is the heat capacity, and  $k$  is the thermal conductivity. The temperature perturbation also must

satisfy the boundary conditions

$$\theta(x,y,D,t) = 0 \quad (\text{A-2})$$

$$\theta(x,y,D+l,t) = 0 \quad (\text{A-3})$$

where  $D(x,y,t)$  is the seafloor depth; the seafloor lies beneath a water layer with density  $\rho_w$ . Equation (A-1) is simplified by using the boundary layer approximation

$$\frac{\delta^2 \theta}{\delta x^2} \sim \frac{\delta^2 \theta}{\delta y^2} \ll \frac{\delta^2 \theta}{\delta z^2} \quad (\text{A-4})$$

and (A-1) becomes

$$\rho_m C_p \left( \frac{\delta \theta}{\delta t} + v_x \frac{\delta \theta}{\delta x} + v_y \frac{\delta \theta}{\delta y} \right) = k \frac{\delta^2 \theta}{\delta z^2} \quad (\text{A-5})$$

After integrating (A-5) over  $z$  from  $D$  to  $l$  we find

$$\rho_m C_p \int_D^l \left( \frac{\delta \theta}{\delta t} + v_x \frac{\delta \theta}{\delta x} + v_y \frac{\delta \theta}{\delta y} \right) dz = k \frac{\delta \theta}{\delta z} \Big|_D^l \quad (\text{A-6})$$

Using assumptions 2 and 3 we find the seafloor depth is

$$D(x,y,t) = D_{\text{ref}} + \frac{\alpha \rho_m}{(\rho_m - \rho_w)} \int_D^l \left( T_{\text{ref}}(z) - \theta(x,y,z,t) \right) dz \quad (\text{A-7})$$

After differentiating (A-7) with respect to  $x$ ,  $y$ , and  $t$  and summing the three derivatives we find

$$\frac{\delta D}{\delta t} + v_x \frac{\delta D}{\delta x} + v_y \frac{\delta D}{\delta y} = \frac{-\alpha \rho_m}{(\rho_m - \rho_w)} \int_D^{\ell} \left( \frac{\delta \theta}{\delta t} + v_x \frac{\delta \theta}{\delta x} + v_y \frac{\delta \theta}{\delta y} \right) dz \quad (A-8)$$

The integrals and integrands of (A-6) and (A-8) are identical. By eliminating the integrals from these two equations we arrive at the final result

$$\frac{\delta D}{\delta t} + v_x \frac{\delta D}{\delta x} + v_y \frac{\delta D}{\delta y} = \frac{\alpha}{C_p (\rho_m - \rho_w)} \left( q_s(x, y, t) - q_l(x, y, t) \right) \quad (A-9)$$

Notice this equation does not contain the thermal conductivity and in fact no vertical heat transfer process has been specified. The only requirement is that heat does not transfer horizontally, in a reference frame moving with the lithosphere.

# Thermal Isostasy: Response of a Moving Lithosphere to a Distributed Heat Source

DAVID T. SANDWELL

*Department of Earth and Space Sciences, University of California at Los Angeles  
Los Angeles, California 90024*

Spreading ridges and hot spot swells are identified by their high surface heat flow, shallow seafloor, and high geopotential. To understand these and other thermotectonic features, the oceanic lithosphere is modeled as a thermomechanical boundary layer moving through a three-dimensional, time-independent heat source. The heat source mimics the heat advection associated with a spreading ridge or hot spot without introducing the nonlinearities of these flow processes. The Fourier transforms of three Green's functions (response functions), which relate the three observable fields to their common heat source, are determined analytically. Each of these response functions is highly anisotropic because the lithosphere is moving with respect to the source. However, the ratio of the gravity response function to the topography response function (i.e., gravity/topography transfer function) is nearly isotropic and has a maximum lying between the flexural wavelength and  $2\pi$  times the thickness of the thermal boundary layer. The response functions are most useful for determining the surface heat flow, seafloor topography, and geopotential for complex lithospheric thermal structures. In practice, these three observables are calculated by multiplying the Fourier transform of the heat source by the appropriate response function and inverse transforming the products. Almost any time-independent thermotectonic feature can be modeled using this technique. Included in this report are examples of spreading ridges and thermal swells, although more complex geometries such as ridges offset by transform faults and RRR-type triple junctions can also be modeled. Because forward modeling is both linear and computationally simple, the inverse of this technique could be used to infer some basic characteristics of the heat source directly from the observed fields.

## 1. INTRODUCTION

The thermal and mechanical properties of the oceanic lithosphere have been largely determined by modeling seafloor depth, surface heat flow, and geopotential. Intrinsic thermal properties such as coefficient of thermal expansion, thermal diffusivity, and mantle temperature are inferred by modeling the observed age dependence of depth, heat flow, and geoid height [Sclater and Francheteau, 1970; Sclater *et al.*, 1975; Parsons and Sclater, 1977; Sandwell and Schubert, 1980]. According to the lithospheric cooling models [Turcotte and Oxburgh, 1967; McKenzie, 1967; Parker and Oldenburg, 1973; Haxby and Turcotte, 1978] significant variations in these observable fields occur over distances greater than the thickness of the thermal boundary layer. This indicates that lithospheric thermal properties are most sensitive to the longer wavelength variations in the observable fields. On the other hand, the rheology of the lithosphere is most strongly reflected in topography and free-air gravity anomaly at wavelengths near the flexural wavelength [Walcott, 1970; McKenzie and Bowin, 1976; Watts, 1978; Caldwell and Turcotte, 1979; Chapple and Forsyth, 1979; McNutt, 1979]. The combination of these studies, at long and short wavelengths, demonstrates that the oceanic lithosphere is a thermomechanical boundary layer. The thermal boundary layer (TBL) develops and increases in thickness as a consequence of conductive heat loss. A mechanical boundary layer develops concurrently with the TBL because creep processes are highly dependent upon temperature [Kirby, 1980]. To a first approximation, the uppermost portion of the lithosphere, between depths of 10 and 40 km, has a viscous relaxation time that is greater than the age of the lithosphere and can maintain the large bending stresses ( $\sim 50$  MPa) associated with lithospheric flexure. Between the base of

this elastic layer and the lithosphere-asthenosphere boundary, lies material with a plastic rheology that flows when it is subjected to the larger flexural stresses but is rigid enough to maintain the smaller, thermally induced stresses that support the difference in elevation between ridge crests and ocean basins [Turcotte and Oxburgh, 1976; Kirby, 1980; Lambeck and Nakiboglu, 1980]. The asthenosphere, which readily flows over geologic time, lies beneath this plastic layer.

In this study we develop a combined thermomechanical model for the oceanic lithosphere that is based upon the successful aspects of the longer-wavelength lithospheric cooling models and the shorter-wavelength flexure models. Our major purpose is to calculate the observables (surface heat flow, seafloor topography, and geopotential) for three-dimensional thermotectonic features without resorting to numerical methods (i.e., finite difference or finite element techniques).

The addition of a third dimension makes it possible to model features such as hot spot swells, offset spreading ridges, and RRR (ridge-ridge-ridge) type triple junctions. However, to maintain mathematical simplicity and linearity in the model, a number of physical processes are neglected or approximated. First, we assume that the flexural rigidity is not temperature dependent. This assumption is valid as long as the temperatures of the upper third of the lithosphere do not change significantly across the region being modeled. Second, we assume that perturbations to the observable fields result from thermal anomalies within the lithosphere. This assumption cannot be justified, since small-scale convection beneath a mature lithosphere has an effect upon both the seafloor topography and the geopotential [McKenzie, 1977; Kaula, 1980]. However, it is difficult to estimate these effects since the thermal and mechanical properties of the mantle are not well constrained [Hager and O'Connell, 1981]. In this model we consider only the lithospheric



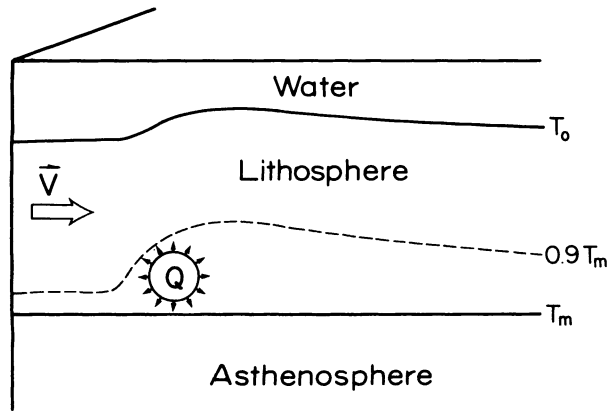


Fig. 1. As the lithosphere passes through a distributed heat source, at a velocity  $v$  it is heated, causing thermal expansion. The increase in surface heat flow far downstream from the source lowers the temperature perturbation, and the swell begins to subside. The base of the lithosphere, defined by the  $T_m$  isotherm, remains at a depth  $l$ .

contribution to the observable fields and assume that any portions of the observed fields that are incompatible with this model are, indeed, associated with mantle flow.

Heat advection from the upper mantle to the lithosphere is simulated by embedding a stationary time-independent heat source within the moving lithosphere. Clearly, this situation is physically unreasonable since the heat source will be swept downstream by the moving lithosphere. As an alternative, the source could be distributed along the base of the lithosphere. However, for velocities greater than a few millimeters per year, a basal heat source does not significantly alter the lithospheric thermal structure because downstream heat advection dominates vertical heat diffusion [Birch, 1975; Gass *et al.*, 1978; Pollack *et al.*, 1981]. To produce the rapid uplift rate at the southeast end of the Hawaiian swell, heat must be advected into the lower two thirds of the lithosphere [Detrick and Crough, 1978]. Instead of modeling this flow process, we have bypassed the problem by introducing a heat source within the moving lithosphere. This heat source representation not only retains linearity in the thermomechanical model but also allows creation of lithospheric thermal structures that are identical to the more reasonable flow models. In fact, any imaginable time-independent thermal structure can be created by a suitable heat source.

Perhaps that most severe restriction of the model is the assumption of a time-independent heat source, since it is evident that major plates have changed velocity, both amplitude and direction [Menard and Atwater, 1968]. The Hawaiian-Emperor seamount chain reflects the direction change of the Pacific plate with respect to the Hawaiian hot spot. For the past 40 m.y., however, this relative velocity has remained constant; to a first approximation, our proposed model may be applied. The heat source response is linear, so the effects of time variations in velocity, which are equivalent to space-time variations in heat source strength, could be approximated by superposition of a number of time-independent models. Alternatively, the problem could be reformulated with a time-dependent source. We have not added this fourth dimension, however, since time-dependent effects are not well constrained by the observations.

In section 2 we present a linear thermomechanical model

for the oceanic lithosphere and develop analytic expressions for the Fourier transforms of three Green's functions (i.e., response functions) that relate the three observable fields to a lithosphere moving through a distributed heat source. Each of the observable fields is a three-dimensional convolution of the heat source with the appropriate Green's function. In the Fourier transform domain the convolution is just a multiplication, and the problem is naturally divided into a source function and a response function. The forms of these solutions lend themselves to three commonly used modeling techniques: transfer function modeling, forward modeling, and inverse modeling. Examples of each of these techniques are presented in sections 3, 4, and 5, respectively, to demonstrate the capabilities and limitations of the model. In section 3 we compare the gravity/topography transfer function for this thermal compensation model to the transfer functions for Airy and regional compensation models. Forward models of symmetrically spreading ridges and hot spot swells are presented in section 4. Finally, in section 5 we discuss the application of the response functions to the inverse problem, which is to infer basic characteristics of the heat source directly from the observables.

## 2. RESPONSE OF A MOVING PLATE TO A DISTRIBUTED HEAT SOURCE

The thermomechanical model consists of a plate of thickness  $l$  moving at a constant velocity  $v$  through a three-dimensional, time-independent heat source, as shown in Figure 1. Far upstream from the source (i.e.,  $v$  direction) the surface heat flow, seafloor topography, and gravitational potential are all zero. As the lithosphere passes through the source, its temperature increases. This produces a local increase in the observable fields. The amplitude and geometry of the field perturbations depend not only upon the shape and extent of the heat source but also upon the rheology and thermal properties of the lithosphere.

These properties and the boundary conditions are shown in Figure 2. The top of the lithosphere is maintained at a temperature of  $T_0$ , while the base of the lithosphere, at a depth  $l$ , has a temperature  $T_m$ . The intrinsic thermal properties  $\alpha$ ,  $\kappa$ , and  $C_p$  (see Table 1 for definitions and values of these parameters) are assumed to remain constant throughout the lithosphere. Figure 2b shows the rheology of our model lithosphere. The uppermost layer behaves like a thin

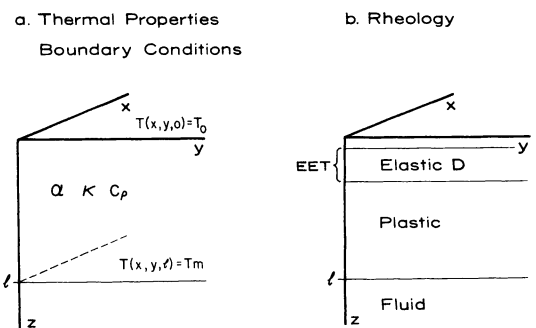


Fig. 2. (a) Intrinsic thermal properties and thermal boundary conditions. The temperature at the seafloor is  $T_0$  and at the base of the lithosphere is  $T_m$ . The thermal properties  $\alpha$ ,  $\kappa$ , and  $C_p$  are constant throughout the lithosphere. (b) The lithosphere has an elastic layer with a flexural rigidity of  $D$  and a plastic layer that extends to the base of the TBL.

elastic plate with a flexural rigidity of  $D$ . Beneath it lies a plastic layer that can support stresses arising from thermal buoyancy but cannot support the larger deviatoric stresses associated with lithospheric flexure. The asthenosphere lies at depths greater than  $l$  and behaves as an incompressible, inviscid fluid. The mechanical boundary conditions are the vertical seafloor displacement  $w(x)$  and its derivatives must vanish as  $|x| \rightarrow \infty$ . In the absence of a heat source, the temperature increases linearly with increasing depth from a value of  $T_0$  at  $z = 0$  to  $T_m$  at  $z = l$ . As the lithosphere passes through the source, it heats up; maximum temperatures are attained on the downstream edge of the source. Away from the upper and lower boundaries the temperatures are constrained only by the heat source and could rise above  $T_m$  or fall below  $T_0$  if the source is not designed properly.

Expressions relating the surface observables and the temperature perturbation to an arbitrary heat source are derived in Appendix A. The solution proceeds in a straightforward manner. The temperature perturbation is found by solving the inhomogeneous heat conduction equation for a plate moving through a heat source. The surface heat flow is the thermal conductivity multiplied by the surface temperature gradient. Downstream from the source lies a low-density, buoyant region that exerts an upward force upon the base of the elastic layer. The vertical seafloor deflection is determined by solving the biharmonic equation for a thin elastic plate overlying a fluid half space where the inhomogeneous pressure term is the integral over depth of the thermal buoyancy force. The combination of the mass excess contained in the seafloor swell and the mass deficit supporting the swell perturbs the gravitational potential. Well-known Greens' functions exist for each of the differential equations (i.e., the diffusion equation, the biharmonic equation, and Poisson's equation). Thus, the observable fields could be calculated by multiple, three-dimensional convolutions over these Green's functions. However, many of the integrals can only be performed numerically. To avoid this time-consuming procedure, each of the Green's functions is Fourier-transformed in the  $x$  and  $y$  directions. This reduces the multiple  $x$  and  $y$  convolutions to multiplications. The remaining vertical convolution integrals are all simple enough to be evaluated analytically.

A flat earth approximation is used throughout the derivation. The error introduced in the gravitational potential by this approximation can be estimated from the ratio of the spherical upward continuation kernel to the flat earth up-

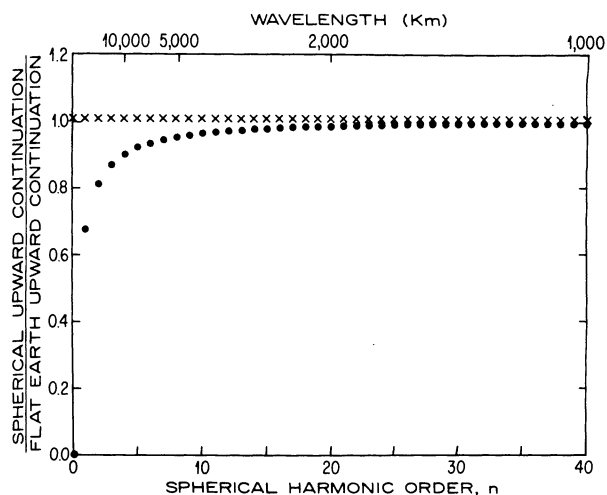


Fig. 3. The ratio of the spherical upward continuation kernel to the flat earth upward continuation kernel for topography that is isostatically compensated at a depth of 100 km is plotted (solid circles) against spherical harmonic order  $n$ . The same ratio with the factor  $2n/(2n + 1)$  removed is shown as crosses.

ward continuation kernel for isostatically compensated topography [see Jeffreys, 1976, p. 237]:

$$\left( \frac{2n}{2n + 1} \right) \left( \frac{1 - (1 - h/a)^n}{1 - \exp(-nh/a)} \right) \quad (1)$$

where  $n$  is the spherical harmonic degree,  $a$  is the radius of the earth, and  $h$  is the depth of compensation. This ratio is shown in Figure 3 (solid circles) for  $h = 100$  km. Most of the difference between the two upward continuation kernels comes from the factor  $2n/(2n + 1)$  [Dorman and Lewis, 1970]. The crosses on Figure 3 show this ratio with the factor omitted. This 'isostatic earth-flattening factor' was included in the derivation of the gravitational potential and substantially reduces the error associated with the flat earth approximation.

The two-dimensional Fourier transforms of the temperature perturbation  $T(\mathbf{k}, z)$ , the surface heat flow  $Q(\mathbf{k})$ , the seafloor topography  $W(\mathbf{k})$ , and the gravitational potential  $U(\mathbf{k}, z)$  are equal to the vertical convolution of the heat source  $q(\mathbf{k}, z)$  with their respective response functions. These convolution integrals are given in equations (A11), (A14), (A19), and (A29) of Appendix A. Calculating the temperature perturbation and the observables from these equations requires a considerable amount of computation. For an arbitrary source, one must first take its Fourier transform at each depth, perform the vertical convolution, and take the inverse Fourier transform of the result. Computation time is vastly decreased if the heat source can be separated into horizontal and vertical components as follows:

$$q(\mathbf{x}, z) = q(\mathbf{x}) f(z) \quad (2)$$

and if the vertical convolution of  $f(z)$  with each of the response functions can be performed analytically.

The most useful source function decreases linearly with depth between either the seafloor and the base of the lithosphere or a depth  $z_1$  and the base of the lithosphere:

$$\begin{aligned} f(z) &= 0 & z < z_1 \\ f(z) &= 1 - z & z_1 < z < l \end{aligned} \quad (3)$$

TABLE 1. Definitions and Values of Parameters

Parameter	Definition	Value/Units
$a$	mean earth radius	6371 km
$\alpha$	thermal expansion coefficient	$3.1 \times 10^{-5} \text{ } ^\circ\text{C}^{-1}$
$D$	flexural rigidity	$7 \times 10^{22} \text{ N m}$
$C_p$	heat capacity	$1172 \text{ J kg}^{-1} \text{ } ^\circ\text{C}^{-1}$
$g$	acceleration of gravity	$9.82 \text{ m s}^{-2}$
$G$	gravitational constant	$6.67 \times 10^{-11} \text{ N m}^2 \text{ kg}^{-2}$
$\kappa$	thermal diffusivity	$8 \times 10^{-7} \text{ m}^2 \text{ s}^{-1}$
$l$	lithospheric thickness	128 km
$\rho_m$	mantle density	$3330 \text{ kg m}^{-3}$
$\rho_w$	water density	$1025 \text{ kg m}^{-3}$
$s$	mean seafloor depth	5 km
$T_m$	mantle temperature	$1365 \text{ } ^\circ\text{C}$
$T_0$	seafloor temperature	$0^\circ\text{C}$

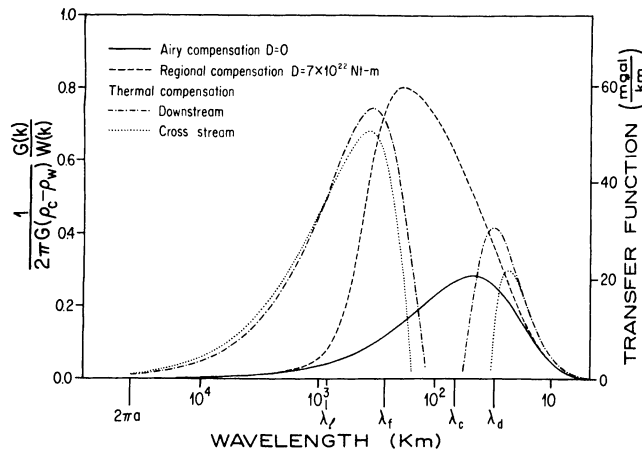


Fig. 4. Gravity/topography transfer functions for Airy compensation (solid line), regional compensation (dashed line), and thermal compensation (dashed-dotted line for downstream, dotted line for cross-stream). The five important length scales are  $\lambda_d = 31$  km ( $2\pi \times$  ocean depth),  $\lambda_c = 69$  km ( $2\pi \times$  depth to Moho),  $\lambda_f = 263$  km (flexural wavelength),  $\lambda_r = 804$  km ( $2\pi \times$  depth to the asthenosphere), and  $2\pi a$ , where  $a$  is the radius of the earth.

As shown in the following sections, this particular depth variation can be used to construct a spreading ridge model or a lithospheric thinning model. Consider a thinning model. Far upstream from the source, the temperature increases linearly with depth. The lower portion of the lithosphere, between depths of  $z_1$  and  $l$ , can be thinned (raised to a temperature approaching  $T_m$ ) by a source that decreases linearly with depth according to (3). Equation (3) is also simple enough to be analytically convolved with each of the response functions. These convolutions are carried out in Appendix B. The results are given in equations (B2), (B3), (B4), and (B5), where the temperature and the observables  $O_i(\mathbf{k})$  are related to the source  $q(\mathbf{k})$  by multiplication with the appropriate response function  $K_i'(\mathbf{k})$ :

$$O_i(\mathbf{k}) = q(\mathbf{k}) K_i'(\mathbf{k}) \quad (4)$$

The index  $i$  is equal to 0 for temperature, 1 for heat flow, 2 for topography, and 3 for potential. By performing these convolutions analytically the modeling procedure is reduced to two, two-dimensional Fourier transforms that can be calculated rapidly using the FFT algorithm (fast Fourier transform). For example, the geoid height over a lithosphere moving at velocity  $v$  through a source that varies with depth like (3) is calculated by taking the two-dimensional FFT of the source, multiplying by  $K_3'(\mathbf{k})$ , and inverse transforming the result.

In theory, this procedure is relatively simple. However, in practice, problems arise because the heat source must be represented on a grid with a finite number of points. To avoid aliasing the digital Fourier transform of the source, the spacing between grid points must be less than one half the shortest wavelength contained in the source. The width of the grid in the cross-stream direction must be at least twice the source width or the flexural wavelength, whichever is larger. In the downstream direction, the grid length must be  $\gg l^2 v / \kappa$  so that the inverse FFT is not aliased by incomplete sampling in wave number space; we have used a grid length of  $4 \times 10^4$  km in our models. This great length is required because it takes about one billion years for a heat pulse, within a 128-km-thick lithosphere, to decay to less than 1%

of its initial value. Indeed, it is numerically impossible to calculate models when the plate thickness approaches infinity, since the grid must contain an infinite number of points in the downstream direction (L. M. Dorman, personal communication, 1980). However, if the shortest wavelength contained in the heat source is  $>1$  km and the lithospheric thickness is  $<1000$  km, then the modeling procedure is extremely fast.

Before presenting forward model calculations, it is useful to look at the ratio of the gravity response function (B6) to the topography response function (B5) in the wave number domain, since this ratio is independent of the horizontal heat source variations.

### 3. GRAVITY/TOPOGRAPHY AND GEOID/TOPOGRAPHY TRANSFER FUNCTIONS

Transfer functions or admittance functions have been used to determine the strength of the lithosphere. Since gravitational potential is nearly linearly related to topography in wave number space [Lewis and Dorman, 1970; McNutt, 1979], the ratio of the Fourier transform of the potential to the Fourier transform of the topography contains information about the topographic compensation mechanism (e.g., local, regional, or thermal). The flexural rigidity of the elastic portion of the lithosphere has been estimated by fitting the observed transfer function to the transfer function predicted by the elastic plate model. The implicit assumption in transfer function modeling is that the perturbation to the gravitational potential is caused by a topographic load on the earth's surface [Dorman and Lewis, 1970]. In this case the source is the topographic load, the transmitter is the elastic plate model, and the receiver is the gravitational potential. However, for thermotectonic features such as spreading ridges and broad swells in the seafloor, the ultimate source of the gravitational potential is not the topographic load but is instead the thermal anomaly within the lithosphere. Therefore, it is not strictly legitimate to calculate the potential/topography transfer function for this model, and the quotient  $U(\mathbf{k})/W(\mathbf{k})$  will not always be well behaved. Despite this difficulty, it is useful to compare this thermomechanical transfer function  $R_T(\mathbf{k})$  with transfer functions for other types of compensation and also with observed transfer functions. Horizontal variations in the heat source are eliminated by taking the ratio of  $U(\mathbf{k})$  to  $W(\mathbf{k})$ . This yields

$$R_T(\mathbf{k}) = K_3'(\mathbf{k})/K_2'(\mathbf{k}) \quad (5)$$

where  $K_2'$  and  $K_3'$  are given in (B5) and (B6), respectively.

A comparison of this thermal transfer function with the elastic plate transfer function demonstrates that the two compensation mechanisms are partially separated in wave number space. Figure 4 shows normalized gravity/topography transfer functions for the elastic plate model with flexural rigidities of zero, which corresponds to Airy-Heiskanen compensation (solid line), and  $7 \times 10^{22}$  N m, a typical value for oceanic lithosphere (Watts [1978]; dashed line). The important length scales for the elastic plate model are reflected in the transfer function. For wavelengths less than  $\lambda_d$  ( $2\pi \times$  ocean depth) the portion of the gravity field caused by undulations in the seafloor-water interface is attenuated by upward continuation. Similarly,  $\lambda_c$  ( $2\pi \times$  depth to the crust-mantle interface) marks the shortest wavelength where the gravity field from Moho undulations can still be ob-

served. Accordingly, Airy-compensated topography has a transfer function peak lying between  $\lambda_d$  and  $\lambda_c$ . A larger value of flexural rigidity introduces another length scale, the flexural wavelength  $\lambda_f$ , which is related to the flexural rigidity by

$$\lambda_f = 2\pi \left[ \frac{D}{g(\rho_m - \rho_w)} \right]^{1/4} \quad (6)$$

For wavelengths much less than  $\lambda_f$  the topography is strongly reflected in the gravity field, and therefore it appears 'uncompensated' (regionally compensated is a better term). The real part of the thermal transfer function for the downstream (dashed-dotted line) and cross-stream (dotted line) directions are also shown on Figure 4. The imaginary part of the downstream transfer function is only about 1% of the real part, while the cross-stream transfer function is purely real. This transfer function corresponds to a lithosphere that has been thinned from an initial depth of 128 km to a final depth of 40 km, using (3) for the vertical heat source variation. The main peak in the thermal transfer function occurs between  $\lambda_l$  ( $2\pi \times$  depth to the asthenosphere) and  $\lambda_f$  (for this case  $D = 7 \times 10^{22}$  N m). Looking from  $\lambda_f$  toward shorter wavelengths, the transfer function first becomes negative, then positive, and finally approaches zero. This rapid decline in the transfer function at the flexural wavelength occurs because the strength of the elastic layer does not allow the seafloor to flex under the thermal buoyancy force, and therefore the positive gravity field caused by the attenuated seafloor swell is not as strong as the negative field from the low-density root. At wavelengths less than  $\lambda_f$ , the strange behavior of the transfer function should be ignored, since for any reasonable heat source (i.e., one that does not melt the lithosphere anywhere) both the gravity and topography are too small to be observed.

The geoid height/topography transfer functions for these same models are shown in Figure 5. These geoid/topography transfer functions are enhanced at the longer wavelengths with respect to the gravity/topography transfer functions. The 'isostatic earth flattening factor'  $2n/(2n + 1)$  forces the transfer functions to approach two thirds its maximum value as the wavelength approaches  $2\pi \times$  radius of the earth.

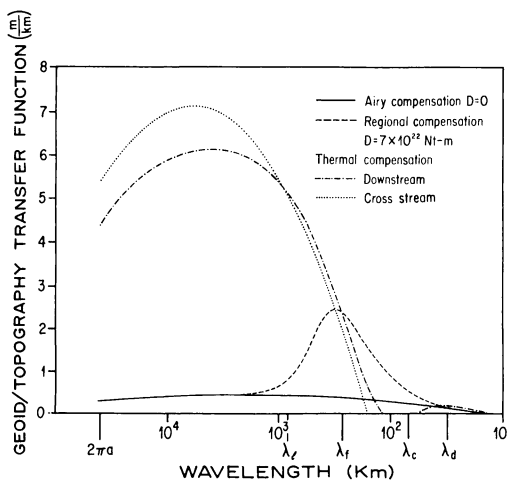


Fig. 5. Geoid/topography transfer functions for the same three models as shown in Figure 4. The thermal transfer function dominates the mechanical transfer function when  $\lambda > \lambda_f$ .

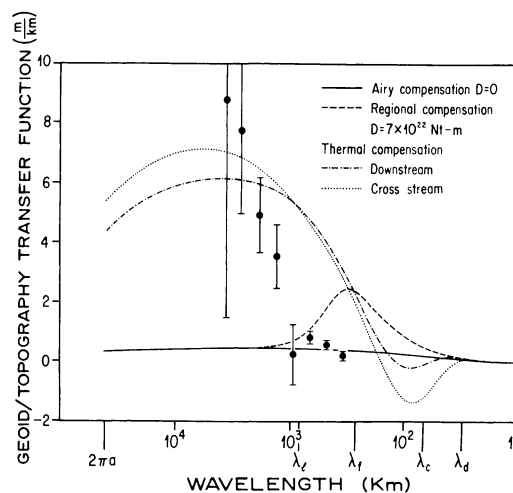


Fig. 6. Data points are estimates of the geoid/topography transfer function for a region in the central Pacific containing the Hawaiian swell. For wavelengths greater than 1100 km the data lie closest to the thermal transfer function, while at shorter wavelengths the topography appears to be Airy compensated.

Without this factor it would remain constant, as predicted by the Ockendon-Turcotte approximation [Ockendon and Turcotte, 1977].

A comparison of Figures 4 and 5 reveals the relative sensitivity of the free-air gravity data and geoid height data to various forms of compensation. For example, 1 km of thermally compensated topography with a wavelength of 3000 km will produce 10 mGal of gravity anomaly and 7 m of geoid height. At longer wavelengths, however, the gravity field diminishes, while the geoid amplitude remains relatively constant. At the other end of the spectrum, where  $\lambda < \lambda_f$ , the gravity anomaly is more sensitive to the mechanically compensated topography than the geoid height when measurement errors are considered [Chapman and Talwani, 1979]. Finally, near the flexural wavelength, the thermal transfer function  $R_T(\mathbf{k})$  and the mechanical transfer function  $R_M(\mathbf{k})$  must overlap. This region of overlap can lead to some difficulties when interpreting observed gravity/topography or geoid/topography transfer functions.

Sandwell and Poehls [1980] have calculated the geoid/topography transfer function for a region in the Central Pacific. The major topographic features included in this region are the Hawaiian swell, the Hawaiian Island chain, the Necker ridge, the northern end of the Line Islands, the Mid-Pacific mountains, and a number of fracture zones. Transfer function estimates and one standard deviation uncertainties are shown on Figure 6 along with the thermal and mechanical transfer functions from Figure 5. At wavelengths greater than 1100 km the data roughly follow the thermal compensation model, while at shorter wavelengths the data lie closer to the Airy compensation model. At intermediate wavelengths, however, the behavior of the observed transfer function can be understood by considering that some fraction of the topography is mechanically supported  $W_M(\mathbf{k})$ , while the remaining topography is thermally supported  $W_T(\mathbf{k})$ . The observed transfer function could be reproduced from a mixture of  $R_M$  and  $R_T$ :

$$R = R_M[W_M/(W_M + W_T)] + R_T[W_T/(W_M + W_T)] \quad (7)$$

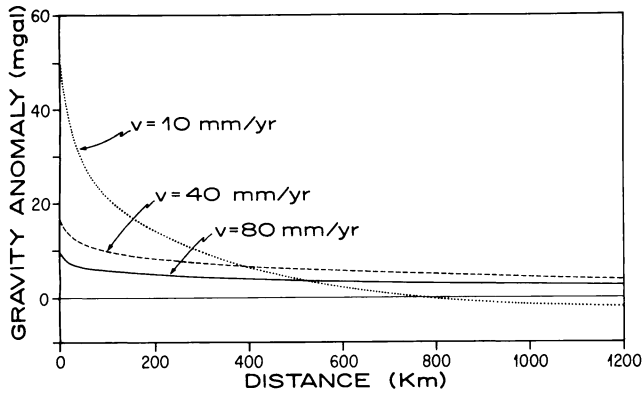


Fig. 7. Gravity anomaly versus distance from the ridge axis for half-spreading velocities of 10, 40, and 80 mm/yr.

There are an infinite number of ways to partition the topography amplitude spectrum between  $W_M$  and  $W_T$ . Sandwell and Poehls [1980] assumed that all of the topography with wavelengths greater than 1100 km was thermally compensated, while the remainder was Airy compensated. For this partitioning, the transfer function follows  $R_M$  for  $\lambda < 1100$  km and follows  $R_T$  for  $\lambda > 1100$  km. A more reasonable partitioning could be used to fit the data more precisely. Considering the uncertainty in the observed transfer function, a step function partitioning suffices.

The thermal compensation model provides a direct link between potential/topography transfer functions and a thermal perturbation within the lithosphere. However, to estimate the amplitudes of the observable quantities (i.e., heat flow, topography, free-air gravity, geoid height), it is best to look at the space domain response of the lithosphere to thermal perturbations of varying geometry. This is done in the next section, where we present forward model calculations for spreading ridge models and lithospheric thinning models.

#### 4. FORWARD MODELS

##### Lithospheric Cooling Models

Lithospheric cooling models are presented here to demonstrate the utility of the heat source formulation and also to check our results against previously published results (i.e., depth and heat flow model, McKenzie [1967]; free-air gravity model, Sclater and Francheteau [1970], Lambeck [1972], and Oldenburg [1975]; geoid height model, Sandwell and Schubert [1980] and Parsons and Richter [1980]). To simulate the thermal structure of lithosphere leaving a spreading center at a velocity  $v_x$ , the initial linear temperature gradient is perturbed to a constant temperature with depth. This is accomplished by placing a heat source at the ridge crest that is infinite in the  $y$  direction, delta function like in the  $x$  direction (in practice, a narrow Gaussian function was used to avoid aliasing the FFT of the source) and decreases linearly with depth according to (3) with  $z_1 = 0$ . This heat source geometry produces only half of a spreading ridge. The other half is obtained by using only the real part of the complex response functions (i.e., forcing symmetry). The depth-age and heat flow-age relations are identical to those already published for the late spreading model (Parsons and Sclater [1977]; North Atlantic model) and therefore are not presented. The gravity anomaly versus distance from the ridge appears in Figure 7 for half-spreading rates of 10, 40,

and 80 mm/yr. The amplitude of the gravity anomaly is nearly inversely proportional to the spreading velocity and correlates better with distance from the ridge axis than it does with seafloor age. On the other hand, the geoid height-age relation is nearly independent of spreading velocity, as shown in Figure 8. Thus, correlations of geoid height with age are useful in characterizing the actual thermal structure of a cooling lithosphere [Haxby and Turcotte, 1978; Sandwell and Schubert, 1980].

In our model, the heat source used to recreate the thermal structure of the plate spreading model has an infinite heat/volume supplied directly beneath the ridge axis. This delta function heat source (in  $x$  direction) produces a singularity in the surface heat flow and also causes the gravity anomaly to have a very sharp peak over the ridge. The response function technique allows a variable width heat source. A more reasonable width of 10 km [Sleep and Rosendahl, 1979] removes 10 mGal from the gravity peak for  $v_x = 10$  mm/yr and at the same time lowers the ridge crest heat flow singularity to a finite value of  $475 \text{ mW m}^{-2}$ . Since the choice of the heat source geometry is totally arbitrary, more exotic spreading ridge models can be created.

As the lithosphere moves from the spreading ridge, it cools and thickens with age. If the growth of the TBL is uninterrupted by additional sources of heat, then the lithosphere and, consequently, the seafloor depth continue to increase as  $(\text{age})^{1/2}$ , assuming that  $\alpha$  and  $\kappa$  are constant throughout the lithosphere. However, in both the Atlantic and Pacific oceans the average depth-age relation begins to flatten from the prediction of the TBL model at about 70 m.y. [Sclater et al., 1971; Parsons and Sclater, 1977]. In the next section we assume that this flattening is caused by heat transfer from the upper mantle to the base of the lithosphere. We then use our model to predict the shapes and amplitudes of the observable fields for various heat source geometries.

##### Lithospheric Reheating Models

The flattening of the depth-age relation can be explained by the plate cooling model [McKenzie, 1967] which as a constant temperature at the base of the lithosphere. According to this model, the lower temperature boundary condition is maintained by mantle-to-lithosphere heat transfer that

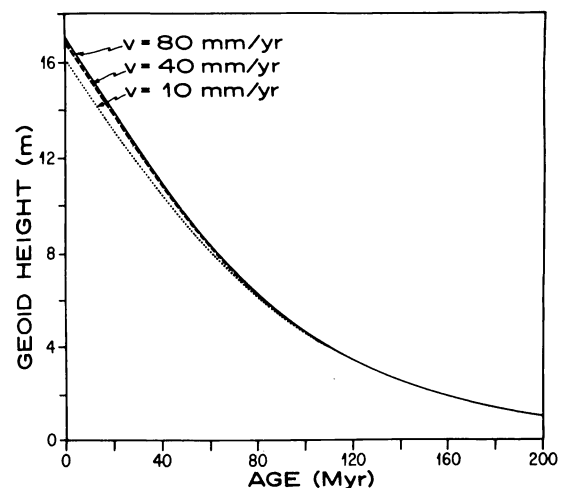


Fig. 8. Geoid height versus age for three spreading velocities. The geoid-age relation is nearly independent of spreading velocity for this cooling model.

increases monotonically with age. This age-dependent heat input has been modeled by a number of physical mechanisms including convective instability at the base of the lithosphere [Parsons and McKenzie, 1978] and an increase in shear heating with age as the lithosphere-asthenosphere boundary cools and becomes more viscous [Schubert *et al.*, 1976]. One must ask, however, is the heat input really age dependent? Surely, this cannot be determined from the depth-age relation, since by correlating depth with age, much of the information about spacial variations of depth is lost; this is especially true for the depth variations along isochrons. The space domain deviations of the depth, heat flow, and geoid from the predictions of the TBL model (i.e., residual depth, residual heat flow, and residual geoid anomalies) may, however, provide this information.

Residual depth maps have been computed for a large part of the world's oceans [Menard, 1973; Sclater *et al.*, 1975; Cochran and Talwani, 1977; Menard and Dorman, 1977; Mammerickx, 1981]. Thermal perturbations with characteristic wavelengths near 1000 km appear as topographic swells on residual depth maps (e.g., Bermuda swell, Hawaiian swell, Cape-Verde swell, Cook-Austral swell, etc.). These swells are also associated with an increase in geoid height [Crough, 1978] and an increase in heat flow [Detrick *et al.*, 1981]. Furthermore, hot spot swells are not preferentially located on older lithosphere. Indeed, if seafloor that has passed over a hot spot is excluded from the depth-age correlation, then depths increase as the (age)<sup>1/2</sup> out to 90 m.y. [Heestand and Crough, 1981]. Hot spots provide an age-independent heat input and are partially responsible for the flattening of the depth-age relation.

In this section we simulate the effects of lithospheric reheating. Rather than focus on a particular reheating model such as small-scale convection, shear heating, or mantle plumes, we suggest dividing the off-ridge heat transfer according to its characteristic wavelength. The amplitudes of the observable fields are strongly dependent upon this wavelength. Forward modeling of various width heat sources provides a method for estimating the amplitudes of the surface observables and more importantly a means of determining which type of observable is best suited for studying thermal perturbations within a given wavelength band.

The responses of a moving lithosphere to thermal perturbations of three different characteristic wavelengths are shown in Figure 9. In these models, the lithosphere is thinned, using (3), to a depth of 40 km as it passes through a heat source at a velocity of 40 mm/yr. The source we have chosen varies as a Gaussian in both horizontal directions:

$$q(x) = \left( \frac{\rho_m C_p v_x T_m f}{(2\pi)^{1/2} \sigma} \right) \exp \left( \frac{-(x^2 + y^2)}{2\sigma^2} \right) \quad (8)$$

where  $2\sigma$  is the source half width and  $f$  is a number  $< 1$  (temperatures may rise about  $T_m$  if  $f > 1$ ). The source half widths for Figures 9a, 9b, and 9c are 2000, 200, and 60 km, respectively, and are outlined by circles. For comparison purposes,  $f$  was chosen so the maximum topographic swell produced by each of the three sources was 1.1 km when the lithospheric flexural rigidity was zero (local compensation). The maximum heat input per area for each of the sources is given in Table 2. To calculate the models shown in Figure 9, a typical value of flexural rigidity was used ( $7 \times 10^{22}$  N m).

The top row in Figures 9a, 9b, and 9c shows the contours of temperature perturbation at a depth of 64 km. In each case the isotherms are swept downstream by the moving lithosphere. The maximum temperature is attained at a distance of  $1\sigma$  to  $2\sigma$  downstream from the heat source maximum. Contours of surface heat flow appear in the second row. The heat flow maxima are 19, 16, and 12 mW m and are displaced in time from the source peak by 32, 21, and 16 m.y. for Figures 9a, 9b, and 9c, respectively. The heat flow peak for the shortest-wavelength source has a relatively lower amplitude because a portion of the heat is conducted horizontally away from the source. The topography for the long- and intermediate-wavelength heat sources reaches a maximum of  $\sim 1$  km at a distance of about  $1\sigma$  downstream from the source peak. The smallest source, however, produces a maximum swell in the topography of less than 0.7 km and has a width that is much greater than the source half width. This relatively low amplitude accompanied by an increase in response wavelength occurs because the lithosphere does not bend readily at wavelengths shorter than its flexural wavelength.

The final two rows in Figures 9a, 9b, and 9c show contours of geoid height and free-air gravity anomaly. The peak response of the gravity field to the broadest heat source is only 8 mGal. Furthermore, the ratio of gravity to topography in the space domain is not constant but varies from 7 to 0 mGal/km. On the other hand, the geoid height closely resembles the topography and has a peak amplitude of 6.5 m. The intermediate-wavelength heat source produces a relatively large gravity anomaly (38 mGal) and 5.1 m of geoid height. The narrowest heat source (Figure 9c) produces a maximum gravity anomaly of 28 mGal, while the geoid height peak for this case is rather low (2.4 m). The effects of flexure are apparent in the intermediate- and short-wavelength gravity fields (the zero contour deviates from the others) but are absent in the geoid height contours.

The peak responses of the observables, heat flow, topography, gravity anomaly, and geoid height, are summarized in Table 2 for each of the three sources. A number of conclusions can be drawn about the observability of thermal perturbations in the lithosphere from these calculations.

1. A thermal perturbation with a characteristic wavelength much less than the flexural wavelength will be difficult to observe on maps of residual depth, residual geoid height, or residual gravity anomaly since the nonthermally compensated topography dominates at these wavelengths.

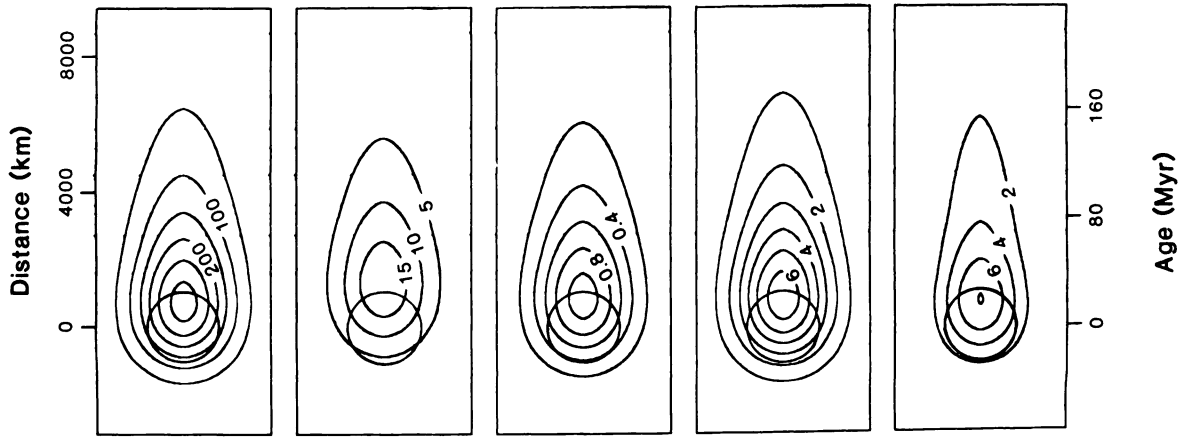
2. Thermal perturbations with characteristic wavelengths greater than  $\lambda_f$  (400 to 2000 km) have been observed in all of the data types and provide a basis for this lithospheric reheating model.

3. The longest-wavelength source ( $2\sigma = 2000$  km) is reflected in the topography, heat flow, and geoid height but is absent in the gravity anomaly. Therefore, long-wavelength off-ridge lithospheric reheating will be observed on residual depth, residual heat flow, and possibly residual geoid height maps if reheating exists at this scale.

With the forward problem solved, the next step is to determine the class of acceptable heat sources that are compatible with the observed fields. As we have shown, the fields are linearly related to the source; thus, linear inverse theory can be used for this problem. These ideas are discussed in the next section.

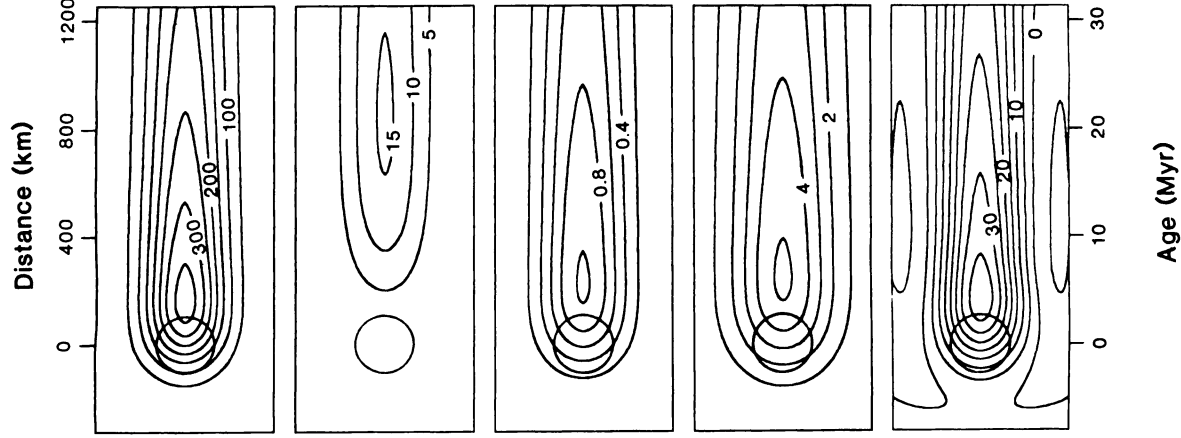
**a**

$2\sigma = 2000$  km



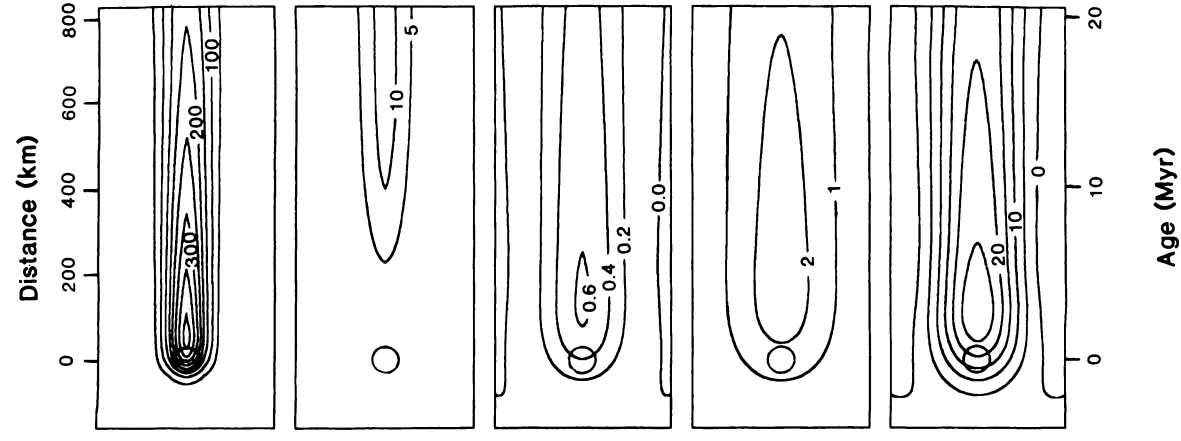
**b**

$2\sigma = 200$  km



**c**

$2\sigma = 60$  km



## 5. INVERSION OF OBSERVABLES FOR HEAT SOURCES

The proposed thermomechanical model for the oceanic lithosphere incorporates many assumptions and approximations. We have assumed that the intrinsic thermal and mechanical properties such as  $\alpha$ ,  $\kappa$ ,  $C_p$ , and  $D$  are independent of temperature or pressure. Moreover, we assume that their values are accurately known from previous studies. The most severe model approximation is that the heat source is time independent. It is evident that plates change speed and direction on a time scale that is about equal to the time it takes a heat pulse to diffuse through the lithosphere. Indeed, this approximation limits the application of the model to the few regions where the thermal structure is steady state. Considering that little is known about lithospheric heating or reheating mechanisms, this approximate model may be useful.

For the moment, we assume that the model is a correct representation of the lithosphere. The solution to the forward problem shows that the vertical variation in the heat source  $q(z_0)$  is related to the observables  $O_i$  by a linear transformation:

$$O_i(\mathbf{k}) = \int_0^1 q(\mathbf{k}, z_0) K_i(\mathbf{k}, z_0) dz_0 \quad (9)$$

where  $i = 1, 2, 3$ . The  $i = 1$  subscript corresponds to the heat flow,  $i = 2$  corresponds to the topography, and  $i = 3$  is the gravitational potential (see Appendix A, equations (A14), (A19), and (A29)). The inverse problem is to determine the three-dimensional variations in the heat source from the observations. Although the problem is linear, it is clearly nonunique for two reasons. First, (9) maps the function  $q(z_0)$ , which resides in an infinite dimensional space, into a three-dimensional data vector, and therefore the mapping is not one to one. Second, observations are made at only a finite number of points. Therefore, even if the data are errorless, the source cannot be uniquely defined. The problem is also unstable since the kernels of (9) are of the upward continuation type. It is impossible to determine the actual source function. However, the data may reveal its basic characteristics [Parker, 1977].

The first step in the problem is to minimize the class of acceptable solutions by applying a priori assumptions or constraints. For instance, the heat source should not oscillate from positive to negative in depth. Thus, a source that is responsible for a positive topographic swell should be positive and should not be composed of a large positive source overlying a smaller negative source. The class of acceptable models can be further restricted by requiring that the temperature of the lithosphere does not exceed the melting temperature. These constraints will greatly limit the class of acceptable heat source models.

Considering both the data inaccuracies and the inherent nonuniqueness of the inverse problem, it is probably best to either assume that the horizontal location of the source is known and invert for the depth dependence or assume that

TABLE 2. Peak Responses of the Lithosphere to Gaussian Heat Sources

	Half Width of Source		
	2000 km	200 km	60 km
Maximum source strength, $\text{W m}^{-2}$	0.043	0.269	0.948
Temperature at 64-km depth, $^{\circ}\text{C}$	320	375	423
Surface heat flow, $\text{mW m}^{-2}$	18.8	15.9	12.1
Seafloor topography, km	1.10	1.02	0.63
Geoid height, m	6.5	5.1	2.4
Gravity anomaly, mGal	8.0	37.8	28.3

the depth dependence is known and solve for the horizontal variations. To solve either of these problems, the vertical and horizontal source variations must be decoupled:

$$q(\mathbf{k}, z_0) = q(\mathbf{k})f(z_0) \quad (10)$$

where  $q(\mathbf{k})$  contains all of the horizontal variations and  $f(z_0)$  is a function that depends on depth only. The second case, where  $f(z_0)$  is known, could be used to locate off-ridge heat sources that are not associated with some obvious tectonic feature such as a linear island chain. With  $f(z_0)$  known, the solution to (9) is just

$$q(\mathbf{k}) = O_i(\mathbf{k}) \left[ \int_0^1 f(z_0) K_i(\mathbf{k}, z_0) dz_0 \right]^{-1} \quad (11)$$

The three types of data can be used to estimate the uncertainties in  $q(\mathbf{k})$ ; call them  $\sigma_q(\mathbf{k})$ . Both the horizontal variations in the source and its uncertainties can be mapped back into the space domain with the inverse Fourier transform. The spectral division in (11), however, is an unstable procedure since the denominator approaches zero at large wave numbers. Observational errors will appear as wild oscillations in the source function. To avoid these problems, spectral deconvolution techniques should be used [Oldenburg, 1981].

For a spreading ridge the horizontal location of the source is fairly well known since it coincides with the axial valley of the ridge crest. Equation (9) can be used to solve for the vertical dependence of the source. In this case, (9) becomes

$$O_i(\mathbf{k})/q(\mathbf{k}) = \int_0^1 f(z_0) K_i(\mathbf{k}, z_0) dz_0 \quad (12)$$

where  $q(\mathbf{k})$  is the Fourier transform of the ridge crest location. Each type of datum exists at only a finite number of wave numbers, say  $N$ . If  $i$  denotes the data type and  $j$  denotes a particular wave number  $\mathbf{k}$ , then (12) becomes

$$O_{ij}' = \int_0^1 f(z_0) K_{ij}(z_0) dz_0 \quad (13)$$

where  $O_{ij}' = O_{ij}/q_j$  and  $K_{ij}(z_0)$  is the  $i$  kernel at the  $j$  wave number. The form of (13) is ideally suited for numerical inversion using the Backus-Gilbert [Backus and Gilbert, 1968] or spectral expansion [Parker, 1977] inversion techniques. Like other types of linear inverse problems there is a trade-off between model resolution and data misfit.

## 6. CONCLUSIONS

1. A stationary, time-independent heat source, within a moving lithosphere, has been used to represent the upper

Fig. 9. (opposite) The responses of the lithosphere moving at a velocity of 40 mm/yr toward the right over Gaussian heat sources with half widths of (a), 2000 km, (b) 200 km, and (c) 60 km. From top to bottom the boxes contain contours of temperature perturbation, surface heat flow, seafloor topography, free-air gravity anomaly and geoid height. The peak in each of the observable fields lies on the downstream side of the source.



mantle heat transfer processes associated with material upwelling at a spreading center and lithospheric thinning over a hot spot. Using this heat source representation along with a linear thermomechanical model for the oceanic lithosphere, we have derived analytic expressions, in the Fourier transform domain, relating the three-dimensional heat source to fields that can be observed on the earth's surface (i.e., surface heat flow, seafloor topography, and geopotential). The linearity and computational simplicity of the model lends itself to transfer function modeling, forward modeling, and inverse modeling.

2. The results from gravity/topography transfer function modeling demonstrate that the thermal compensation model transfer function peaks at a wavelength greater than the flexural wavelength; the transfer function peak for the regional compensation model occurs at a wavelength less than  $\lambda_f$ . This indicates that off-ridge thermotectonic features can be distinguished from off-ridge, regionally compensated topography on the basis of the gravity/topography transfer function. However, if a region of seafloor topography has a mixed compensation mechanism such as the Hawaiian swell and the Hawaiian-Emperor seamount chain, then near the flexural wavelength, the observed transfer function is difficult to interpret.

3. The utility of the heat source formulation was demonstrated by reproducing the thermal structure and observables for a plate cooling model. The heat flow–age and depth–age relations are in agreement with previous studies. Furthermore, we have shown that for typical spreading velocities, geoid height is almost entirely dependent upon age and agrees with geoid height relations derived using the Ockendon-Turcotte approximation.

4. The amplitudes of the surface observables for a mature lithosphere moving through a Gaussian heat source are dependent upon the width of the source. A very narrow source (half width of 60 km) does not appear strongly in the observable fields because the flexural rigidity of the lithosphere suppresses the signal. The geoid height is greatest over a broad source (half width of 2000 km), while the free-air gravity anomaly is most sensitive to an intermediate width source (half width of 200 km).

5. The relationship between the heat source and the observables is linear. Therefore, it is possible to invert directly for the class of sources that are consistent with the data by using linear inverse theory. The class can be narrowed by applying physically reasonable constraints. The three data types are each sensitive to different aspects of the heat source and should be used simultaneously in the inversion to enhance the source resolution. The inverse problem will divide the observed fields into a part that is associated with the lithosphere and a part that comes from deeper within the earth and hopefully will provide a characteristic wavelength for the off-ridge thermal perturbations.

#### APPENDIX A: THERMOMECHANICAL RESPONSE OF A MOVING PLATE TO A DISTRIBUTED HEAT SOURCE

In this section we derive analytic expressions relating quantities that can be observed on the surface of the earth (i.e., surface heat flow, topography, geoid height, and free-air gravity anomaly) to a thermal perturbation within the lithosphere. The geometry of the problem is shown in Figure 1. The observable fields are perturbed as a plate of constant

thickness  $l$  passes through a heat source  $q(x, y, z)$  at a velocity  $\mathbf{v}$ . The temperature at the plate's surface is constant  $T(x, y, 0) = T_0$  and at its base is  $T(x, y, l) = T_m$ . The assumed rheology and mechanical boundary conditions are described in section 2. The solution is obtained through a number of separate steps.

1. Solve the inhomogeneous time-independent heat conduction equation.
2. Differentiate the temperature with respect to  $z$  to determine the surface heat flow.
3. Integrate the thermally induced density perturbations to find the vertical stress on the elastic layer.
4. Solve the inhomogeneous biharmonic equation for the surface deflection.
5. Calculate the disturbing potential for the thermally compensated topography.

Each of these problems has been solved separately (for 1 and 2, see *Carslaw and Jaeger* [1959, p. 266] and *Birch* [1975]; for 3 and 4, see *Banks et al.* [1977] and *Dorman and Lewis* [1974]; for 5, see *Parker* [1972]). Space domain convolutions could be used to link these separate problems, but many of the convolution integrals must be performed numerically and require large amounts of computer time for even the simplest heat source geometries. Fourier transformation of all of the equations in the  $\hat{x}$  and  $\hat{y}$  directions reduces the space domain convolutions to wave number domain multiplications. The convolutions in the  $\hat{z}$  direction are simple enough to be evaluated analytically.

From the outset, the homogeneous solution to the heat conduction problem is subtracted from the thermal structure, since this solution corresponds to the infinite wavelength case. All length scales are nondimensionalized by the lithospheric thickness  $l$ . Throughout the derivation the following notation is used:

$$\mathbf{x} = (x, y)$$

$$\mathbf{k} = (k_x, k_y)$$

$$\nabla_h = \frac{\partial}{\partial x} + \frac{\partial}{\partial y}$$

The two-dimensional Fourier transform and inverse transform are defined as

$$T(\mathbf{k}, z) = \int_{-\infty}^{\infty} \int_{-\infty}^{\infty} t(\mathbf{x}, z) e^{i\mathbf{k} \cdot \mathbf{x}} d^2\mathbf{x}$$

$$t(\mathbf{x}, z) = \frac{1}{(2\pi)^2} \int_{-\infty}^{\infty} \int_{-\infty}^{\infty} T(\mathbf{k}, z) e^{-i\mathbf{k} \cdot \mathbf{x}} d^2\mathbf{k}$$

or in shorthand notation,

$$T(\mathbf{k}, z) = \mathcal{F}_2 [t(\mathbf{x}, z)]$$

$$t(\mathbf{x}, z) = \mathcal{F}_2^{-1} [T(\mathbf{k}, z)]$$

#### Temperature

The temperature perturbation  $t(\mathbf{x}, z)$  is found by solving

$$l \mathbf{v} \cdot \nabla_h t(\mathbf{x}, z) - \kappa \nabla_h^2 t(\mathbf{x}, z) - \kappa \frac{\partial^2 t(\mathbf{x}, z)}{\partial z^2} = \frac{l^2 q(\mathbf{x}, z)}{\rho_m C_p} \quad (\text{A1})$$

subject to the boundary conditions

$$t(\mathbf{x}, 0) = 0 \quad (\text{A2})$$

$$t(\mathbf{x}, 1) = 0 \quad (\text{A3})$$

where  $\kappa$  is the thermal diffusivity,  $\rho_m$  is the density, and  $C_p$  is the heat capacity. The boundary conditions are maintained if an infinite number of heat sources and sinks are suitably placed above and below the plate. Consider a source  $q(\mathbf{x}, z) = q(\mathbf{x}) \delta(z - z_0)$ . By adding positive images at  $z_0 + 2m$  and negative images at  $-z_0 + 2m$ , where  $m$  is any integer, the new source becomes

$$q(\mathbf{x}, z) = q(\mathbf{x}) \sum_{m=-\infty}^{\infty} [\delta(z - z_0 - 2m) - \delta(z + z_0 - 2m)] \quad (\text{A4})$$

and the boundary conditions are satisfied. With this source, (A1) becomes

$$\frac{l}{\kappa} \mathbf{v} \cdot \nabla_h t - \nabla_h^2 t - \frac{\partial^2 t}{\partial z^2} = \frac{l^2 q(\mathbf{x})}{\kappa \rho_m C_p} \sum_{m=-\infty}^{\infty} [\delta(z - z_0 - 2m) - \delta(z + z_0 - 2m)] \quad (\text{A5})$$

Fourier transformation of (A5) in the  $\hat{x}$ ,  $\hat{y}$ , and  $\hat{z}$  directions yields

$$\left[ \left( \frac{-il}{\kappa} \mathbf{v} \cdot \mathbf{k} + \mathbf{k} \cdot \mathbf{k} \right) + k_z^2 \right] T(\mathbf{k}, k_z) = \frac{l^2 q(\mathbf{k})}{\kappa \rho_m C_p} \left[ (e^{ik_z z_0} - e^{-ik_z z_0}) \sum_{m=-\infty}^{\infty} e^{ik_z 2m} \right] \quad (\text{A6})$$

where  $q(\mathbf{k})$  is the Fourier transform of  $q(\mathbf{x})$ . Let

$$p^2 = \mathbf{k} \cdot \mathbf{k} - \frac{il}{\kappa} \mathbf{v} \cdot \mathbf{k} \quad (\text{A7})$$

Next we solve (A6) for  $T(\mathbf{k}, k_z)$  and take its inverse Fourier transform in the  $k_z$  direction only:

$$T(\mathbf{k}, z) = \frac{l^2 q(\mathbf{k})}{2\pi \kappa \rho_m C_p} \sum_{m=-\infty}^{\infty} \int_{-\infty}^{\infty} \exp [ik_z(z_0 - z + 2m)] - \exp [-ik_z(z_0 + z - 2m)] [(k_z + ip)(k_z - ip)]^{-1} dk_z \quad (\text{A8})$$

This integral is performed by calculus of residues. The poles lie at  $\pm ip$  and never intersect the real axis except when  $|\mathbf{k}| = 0$ , which corresponds to the homogeneous solution. The path of integration is chosen so that temperature is zero far from the heat source (i.e.,  $\text{Re}(p) > 0$ ). However, the  $m = 0$  term must be treated separately, since the path of integration depends on  $\text{sgn}(z - z_0)$ . After this integration, (A8) becomes

$$T(\mathbf{k}, z) = \frac{l^2 q(\mathbf{k})}{2\kappa \rho_m C_p p} \left[ e^{-p|z_0 - z|} - e^{-p(z_0 + z)} + (e^{-p(z - z_0)} + e^{p(z - z_0)} - e^{-p(z_0 + z)} - e^{p(z_0 + z)}) \sum_{m=1}^{\infty} e^{-2pm} \right] \quad (\text{A9})$$

Since the root  $\text{Re}(p) > 0$  was chosen for the contour integration, it is easily shown, from the binomial theorem, that

$$\sum_{m=1}^{\infty} e^{-2pm} = \frac{e^{-2p}}{(1 - e^{-2p})} \quad (\text{A10})$$

A vertical superposition of heat sources leads to

$$T(\mathbf{k}, z) = \int_0^1 q(\mathbf{k}, z_0) K_0(\mathbf{k}, z, z_0) dz_0 \quad (\text{A11})$$

where the temperature response function is

$$K_0(\mathbf{k}, z, z_0) = \frac{l^2}{2\kappa \rho_m C_p p} \left[ e^{-p|z_0 - z|} - e^{-p(z_0 + z)} + (e^{-p(z - z_0)} + e^{p(z - z_0)} - e^{-p(z_0 + z)} - e^{p(z_0 + z)}) \frac{e^{-2p}}{(1 - e^{-2p})} \right] \quad (\text{A12})$$

The locations of the source and its images are clear from the structure of (A12). The first two exponentials correspond to the source at  $z = z_0$  and a sink at  $z = -z_0$ . The following terms contain all of the other image sources.

#### Surface Heat Flow

The surface heat flow is the thermal conductivity ( $\kappa \rho_m C_p$ ) multiplied by the surface temperature gradient:

$$Q(\mathbf{k}) = \frac{\kappa \rho_m C_p}{l} \frac{\partial T(\mathbf{k}, z)}{\partial z} \Big|_0 \quad (\text{A13})$$

Inserting (A11) into (A13), we find that

$$Q(\mathbf{k}) = \int_0^1 q(\mathbf{k}, z_0) K_1(\mathbf{k}, z_0) dz_0 \quad (\text{A14})$$

where the surface heatflow response function is

$$K_1(\mathbf{k}, z_0) = l \left[ e^{-pz_0} + (e^{-pz_0} - e^{pz_0}) \frac{e^{-2p}}{(1 - e^{-2p})} \right] \quad (\text{A15})$$

#### Vertical Stress From the Thermal Anomaly

Let  $\rho(\mathbf{k}, z) = -\alpha \rho_m T(\mathbf{k}, z)$  be the thermally induced density perturbation. The vertical pressure is

$$P(\mathbf{k}) = \alpha \rho_m l g \int_0^1 T(\mathbf{k}, z) dz \quad (\text{A16})$$

where  $g$  is the gravitational acceleration and  $T(\mathbf{k}, z)$  is given in (A11).

#### Flexural Response of the Elastic Layer

The equation for the static equilibrium of a thin elastic plate subject to a vertical load is

$$\frac{D}{l^4} \nabla_h^4 w(\mathbf{x}) + \Delta \rho g w(\mathbf{x}) = P(\mathbf{x}) \quad (\text{A17})$$

where  $w(\mathbf{x})$  is the deflection of the seafloor in the  $-z$  direction,  $D$  is the flexural rigidity,  $\Delta\rho$  is the density difference across the earth's surface (e.g.,  $\Delta\rho = \rho_m - \rho_w$  for seafloor deformation,  $\rho_w$  is the seawater density), and  $\rho(\mathbf{x})$  is the pressure. By taking the two-dimensional Fourier transform of (A17), inserting (A16), and solving for  $W(k)$ , we find that

$$W(\mathbf{k}) = \left(1 + \frac{D|\mathbf{k}|^4}{l^4 g(\rho_m - \rho_w)}\right)^{-1} \frac{\alpha\rho_m l}{(\rho_m - \rho_w)} \int_0^1 \int_0^1 q(\mathbf{k}, z_0) K_0(\mathbf{k}, z, z_0) dz dz_0 \quad (\text{A18})$$

After integrating  $K_0$  over  $z$ , the surface deformation is

$$W(\mathbf{k}) = \int_0^1 q(\mathbf{k}, z_0) K_2(\mathbf{k}, z_0) dz_0 \quad (\text{A19})$$

where the topography response function is

$$K_2(\mathbf{k}, z_0) = \left(1 + \frac{D|\mathbf{k}|^4}{l^4 g(\rho_m - \rho_w)}\right)^{-1} \frac{\alpha l^3}{2\kappa(\rho_m - \rho_w)C_p p^2} \left[2 - 2e^{-p z_0} + e^{-p(1+z_0)} - e^{-p(1-z_0)} + (2 - e^{-p} - e^p)(e^{p z_0} - e^{-p z_0}) \frac{e^{-2p}}{(1 - e^{-2p})}\right] \quad (\text{A20})$$

### Disturbing Potential

The gravitational potential of a region of density  $\rho(\mathbf{x}, z)$  that has been deflected vertically by an amount  $w(\mathbf{x})$  is [Parker, 1972]

$$U(\mathbf{k}, -s) = 2\pi G l \sum_{m=0}^{\infty} \frac{1}{m!} \left(\frac{|\mathbf{k}|}{l}\right)^{m-1} \int_0^1 \mathcal{F}_2[w^m(\mathbf{x}) \rho(\mathbf{x}, z)] e^{-|\mathbf{k}|(z+s)} dz \quad (\text{A21})$$

where  $-s$  is the location of the observation plane and  $G$  is the gravitational constant. For our model  $\rho(\mathbf{x}, z)$  is the sum of the linear density gradient, which corresponds to the homogeneous temperatures gradient, and the density associated with the thermal perturbation

$$\rho(\mathbf{x}, z) = \rho_m - \rho_w + \alpha\rho_m T_m(1 - z) - \alpha\rho_m t(\mathbf{x}, z) \quad (\text{A22})$$

By inserting (A11) into (A22) and (A22) into (A21), discarding the terms containing  $\alpha^2$ ,  $\alpha^3$ ,  $\dots$ , and integrating over  $z$  we find that the potential is

$$U = U_w + U_p \quad (\text{A23})$$

The first term on the right is the potential caused by the deformation of the homogeneous density structure. The second term is the potential for the thermally induced density anomaly. As discussed in section 2, the factor

$$\frac{2n}{2n+1} = \frac{2a|\mathbf{k}|}{2a|\mathbf{k}|+l} \quad (\text{A24})$$

is included to partially correct for the earth's sphericity. The first term in (A23) is

$$U_w(\mathbf{k}, -s) = \int_0^1 q(\mathbf{k}, z_0) K_w(\mathbf{k}, -s, z_0) dz_0 \quad (\text{A25})$$

where

$$K_w(\mathbf{k}, -s, z_0) = \left(1 + \frac{D|\mathbf{k}|^4}{l^4 g(\rho_m - \rho_w)}\right)^{-1} \frac{2\pi G \alpha l^4 \alpha e^{-|\mathbf{k}|s}}{\kappa C_p p^2 (2a|\mathbf{k}|+l)} \left\{1 + \frac{\alpha\rho_m T_m}{(\rho_m - \rho_w)} \left[1 + \frac{1}{|\mathbf{k}|} (e^{-|\mathbf{k}|} - 1)\right]\right\} \left[2 - 2e^{-p z_0} + e^{-p(1+z_0)} - e^{-p(1-z_0)} + (2 - e^{-p} - e^p) (e^{p z_0} - e^{-p z_0}) \frac{e^{-2p}}{(1 - e^{-2p})}\right] \quad (\text{A26})$$

There are two cases to be considered when  $U_p(\mathbf{k}, s)$  is calculated: the downstream case, where  $p \neq |\mathbf{k}|$ , and the cross-stream case, where  $p = |\mathbf{k}|$ . The thermally induced part of the potential is

$$U_p(\mathbf{k}, -s) = \int_0^1 q(\mathbf{k}, z_0) K_p(\mathbf{k}, -s, z_0) dz_0 \quad (\text{A27})$$

where

$$K_p(\mathbf{k}, -s, z_0) = \frac{-2\pi G \alpha l^4 \alpha e^{-|\mathbf{k}|s}}{\kappa C_p (2a|\mathbf{k}|+l)p} \left\{\frac{2p}{p^2 - |\mathbf{k}|^2} (e^{-|\mathbf{k}|z_0} - e^{-p z_0}) + (e^{p z_0} - e^{-p z_0}) \left[\frac{2p}{p^2 - |\mathbf{k}|^2} - \frac{e^{-(p+|\mathbf{k}|)}}{p+|\mathbf{k}|} - \frac{e^{-(p-|\mathbf{k}|)}}{p-|\mathbf{k}|}\right] \cdot \left(\frac{e^{-2p}}{1 - e^{-2p}}\right) - \frac{e^{-(p+|\mathbf{k}|)}}{p+|\mathbf{k}|}\right\} \quad p \neq |\mathbf{k}| \quad (\text{A28a})$$

$$K_p(\mathbf{k}, -s, z_0) = \frac{-2\pi G \alpha l^4 \alpha e^{-|\mathbf{k}|s}}{\kappa C_p (2a|\mathbf{k}|+l)\mathbf{k}} \left\{z_0 e^{-|\mathbf{k}|z_0} - (e^{|\mathbf{k}|z_0} - e^{-|\mathbf{k}|z_0}) \cdot \left[\frac{e^{-2|\mathbf{k}|}}{2|\mathbf{k}|} + \left(1 + \frac{1}{2|\mathbf{k}|} (e^{-2|\mathbf{k}|} - 1)\right) \cdot \frac{e^{-2|\mathbf{k}|}}{(1 - e^{-2|\mathbf{k}|})}\right]\right\} \quad p = |\mathbf{k}| \quad (\text{A28b})$$

The total disturbing potential is a vertical convolution of the heat source with the potential response function:

$$U(\mathbf{k}, -s) = \int_0^1 q(\mathbf{k}, z_0) K_3(\mathbf{k}, -s, z_0) dz_0 \quad (\text{A29})$$

where  $K_3$  is

$$K_3 = K_w + K_p \quad (\text{A30})$$

APPENDIX B: RESPONSE FUNCTIONS FOR  
LITHOSPHERIC THINNING

The computation time for a model is substantially reduced if the vertical variation in the heat source is decoupled from the horizontal variation as shown in equation (2). Perhaps the most useful vertical source variation decreases linearly with depth between  $z_1$  and 1 (see section 2, equation (3)) since this source can be convolved with the four response functions. Furthermore, this source function can be used to construct a spreading ridge model or a lithospheric-thinning model. In this appendix the vertical convolution integrals (A11), (A14), (A25), and (A29) are carried out analytically using the vertical source function (3). This procedure is mathematically simple since the most difficult integrands are of the form  $z^2 e^{-pz}$ ; however, it involves a considerable amount of algebra. The results of these convolutions are given below. Temperature perturbation for the depth range  $z_1 < z < 1$  is

$$T(\mathbf{k}, z) = q(\mathbf{k}) K_0'(\mathbf{k}, z) \quad (\text{B1})$$

where the temperature response function is

$$K_0'(\mathbf{k}, z) = \frac{l^2}{2\kappa\rho_m C_p p^2} \left\{ 2(1-z) - (1-z_1) e^{-pz} (e^{pz_1} + e^{-pz_1} + \frac{e^{-pz}}{p} (e^{-pz_1} - e^{pz_1} - e^{-p}) + \frac{e^{-p(1-z)}}{p} + \frac{e^{-2p}(e^{pz} - e^{-pz})}{(1-e^{-2p})} \left[ (1-z_1)(e^{pz_1} + e^{-pz_1}) + \frac{1}{p} (e^{pz_1} - e^{-pz_1} - e^p + e^{-p}) \right] \right\} \quad (\text{B2})$$

Similarly, the surface heat flow is  $q(\mathbf{k})$  multiplied by the response function

$$K_1'(\mathbf{k}) = \frac{l}{p} \left\{ (1-z_1) \left[ e^{-pz_1} + \frac{e^{-2p}(e^{pz_1} + e^{-pz_1})}{(1-e^{-2p})} \right] + \frac{1}{p} \left[ (e^{-p} - e^{-pz_1}) + \frac{e^{-2p}}{(1-e^{-2p})} \cdot (e^{pz_1} - e^{-pz_1} - e^p + e^{-p}) \right] \right\} \quad (\text{B3})$$

The topography response function is

$$K_2'(\mathbf{k}) = \frac{\alpha l^3}{2\kappa(\rho_m - \rho_w) C_p p^3} \left( 1 + \frac{D|\mathbf{k}|^4}{g(\rho_m - \rho_w)} \right)^{-1} \cdot \left\{ (1-z_1) \left[ p(1-z_1) - 2e^{-pz_1} + (e^{pz_1} + e^{-pz_1}) \cdot \left( e^{-p} - \frac{e^{-2p}}{(1-e^{-2p})} (2 - e^p - e^{-p}) \right) \right] + \frac{1}{p} \left[ 2(e^{-pz_1} - e^{-p}) + (e^{pz_1} - e^{-pz_1} - e^p + e^{-p}) \right] \right\}$$

$$\cdot \left( e^{-p} - \frac{e^{-2p}}{(1-e^{-2p})} (2 - e^p - e^{-p}) \right) \left. \right\} \quad (\text{B4})$$

Again the potential response function is the sum of two terms:

$$K_3'(\mathbf{k}) = K_w'(\mathbf{k}) + K_p'(\mathbf{k}) \quad (\text{B5})$$

where the contribution from the topography is

$$K_w'(\mathbf{k}) = \frac{4\pi G \alpha l (\rho_m - \rho_w) l e^{-|\mathbf{k}|l}}{2a|\mathbf{k}| + l} \left\{ 1 + \frac{\alpha \rho_m T_m}{(\rho_m - \rho_w)} \cdot \left[ 1 + \frac{1}{|\mathbf{k}|} (e^{-|\mathbf{k}|} - 1) \right] \right\} K_2'(\mathbf{k}) \quad (\text{B6})$$

and the contribution from the thinned portion of the lithosphere is

$$K_p'(\mathbf{k}) = \frac{-2\pi G \alpha l^4 e^{-|\mathbf{k}|l}}{(2a|\mathbf{k}| + l) \kappa C_p p} \left\{ \frac{2p}{p^2 - |\mathbf{k}|^2} \left[ (1-z_1) \left( \frac{e^{-|\mathbf{k}|z_1}}{|\mathbf{k}|} - \frac{e^{-pz_1}}{p} \right) + \frac{1}{|\mathbf{k}|^2} (e^{-|\mathbf{k}|} - e^{-|\mathbf{k}|z_1}) - \frac{1}{p^2} (e^{-p} - e^{-pz_1}) \right] + \frac{1}{p} \left[ \left( \frac{e^{-(p+|\mathbf{k}|)}}{p+|\mathbf{k}|} - \left( \frac{2p}{p^2 - |\mathbf{k}|^2} - \frac{e^{-(p+|\mathbf{k}|)}}{p+|\mathbf{k}|} - \frac{e^{(p-|\mathbf{k}|)}}{p-|\mathbf{k}|} \right) \cdot \frac{e^{-2p}}{(1-e^{-2p})} \right) \left( (1-z_1)(e^{pz_1} + e^{-pz_1}) + \frac{1}{p} (e^{pz_1} - e^{-pz_1} - e^p + e^{-p}) \right) \right] \right\} \quad (\text{B7})$$

when  $p \neq |\mathbf{k}|$ , and is

$$K_p'(\mathbf{k}) = \frac{-2\pi G \alpha l^4 e^{-|\mathbf{k}|l}}{(2a|\mathbf{k}| + l) \kappa C_p |\mathbf{k}|^2} \left\{ z_1(1-z_1) e^{-|\mathbf{k}|z_1} + \frac{1}{|\mathbf{k}|} (e^{-|\mathbf{k}|} + (1-2z_1) e^{-|\mathbf{k}|z_1}) + \frac{2}{|\mathbf{k}|^2} (e^{-|\mathbf{k}|} - e^{-|\mathbf{k}|z_1}) + \left[ \frac{e^{-2|\mathbf{k}|}}{2|\mathbf{k}|} + \left( 1 + \frac{1}{2|\mathbf{k}|} (e^{-2|\mathbf{k}|} - 1) \right) \frac{e^{-2|\mathbf{k}|}}{(1-e^{-2|\mathbf{k}|})} \right] \cdot \left[ (1-z_1)(e^{|\mathbf{k}|z_1} + e^{-|\mathbf{k}|z_1}) + \frac{1}{|\mathbf{k}|} (e^{|\mathbf{k}|z_1} - e^{-|\mathbf{k}|z_1} - e^{|\mathbf{k}|} + e^{-|\mathbf{k}|}) \right] \right\} \quad (\text{B8})$$

when  $p = |\mathbf{k}|$ . The complex wave number  $p$  is

$$p = \mathbf{k} \cdot \mathbf{k} - \frac{il}{\kappa} (\mathbf{v} \cdot \mathbf{k}) \quad (\text{B9})$$

FORTRAN code to generate models from these response functions can be obtained from the author.

*Acknowledgments.* I thank LeRoy Dorman for his many helpful suggestions and the reviewers for pointing out the weak points in the original manuscript. This work was supported by the NASA Geodynamics Program under grant NAG5152.

#### REFERENCES

- Backus, G. E., and F. Gilbert, The resolving power of gross earth data, *Geophys. J. R. Astron. Soc.*, 16, 169–205, 1968.
- Banks, R. J., R. L. Parker, and S. P. Huestis, Isostatic compensation on a continental scale: Local versus regional mechanisms, *Geophys. J. R. Astron. Soc.*, 51, 431–452, 1977.
- Birch, F. S., Conductive heat flow anomalies over a hot spot in a moving medium, *J. Geophys. Res.*, 80, 4825–4827, 1975.
- Caldwell, J. G., and D. L. Turcotte, Dependence of the thickness of the elastic oceanic lithosphere on age, *J. Geophys. Res.*, 84, 7572–7576, 1979.
- Carlsaw, H. S., and J. C. Jaeger, *Conduction of Heat in Solids*, 2nd ed., Oxford University Press, New York, 1959.
- Chapman, M. E., and M. Talwani, Comparison of gravimetric geoids with Geos 3 altimetric geoid, *J. Geophys. Res.*, 84, 3803–3816, 1979.
- Chapple, W. M., and D. W. Forsyth, Earthquakes and bending of plates at trenches, *J. Geophys. Res.*, 84, 6729–6749, 1979.
- Cochran, J. R., and M. Talwani, Free-air gravity anomalies in the world's oceans and their relationship to residual elevation, *Geophys. J. R. Astron. Soc.*, 50, 495–552, 1977.
- Crough, S. T., Thermal origin of mid-plate hot-spot swells, *Geophys. J. R. Astron. Soc.*, 55, 451–469, 1978.
- Detrick, R. S., and S. T. Crough, Island subsidence, hot spots and lithospheric thinning, *J. Geophys. Res.*, 83, 1236–1244, 1978.
- Detrick, R. S., R. P. Von Herzen, S. T. Crough, D. Epp, and U. Fehn, Evidence for lithospheric reheating from heat flow measurements on the Hawaiian swell, *Nature*, 292, 142–143, 1981.
- Dorman, L. M., and B. T. R. Lewis, Experimental isostasy, 1, Theory of the determination of the earth's isostatic response to a concentrated load, *J. Geophys. Res.*, 75, 3357–3365, 1970.
- Dorman, L. M., and B. T. R. Lewis, The use of nonlinear functional expansions in calculations of the terrain effect in airborne and marine gravimetry and gradiometry, *Geophysics*, 39, 33–38, 1974.
- Gass, I. G., D. S. Chapman, H. N. Pollack, and R. S. Thorpe, Geological and geophysical parameters of mid-plate volcanism, *Philos. Trans. R. Soc. London, Ser. A.*, 288, 581–597, 1978.
- Hager, B. H., and R. J. O'Connell, A simple global model of plate dynamics and mantle convection, *J. Geophys. Res.*, 86, 4843–4867, 1981.
- Haxby, W. F., and D. L. Turcotte, On isostatic geoid anomalies, *J. Geophys. Res.*, 83, 5473–5478, 1978.
- Heestand, R. L., and S. T. Crough, The effect of hot spots on the oceanic depth-age relation, *J. Geophys. Res.*, 86, 6107–6114, 1981.
- Jeffreys, H., *The Earth*, 6th ed., Cambridge University Press, New York, 1976.
- Kaula, W. M., Material properties for mantle convection consistent with observed surface fields, *J. Geophys. Res.*, 85, 7031–7044, 1980.
- Kirby, S. H., Tectonic stresses in the lithosphere: Constraints provided by the experimental deformation of rocks, *J. Geophys. Res.*, 85, 6353–6363, 1980.
- Lambeck, K., Gravity anomalies over ocean ridges, *Geophys. J. R. Astron. Soc.*, 30, 37–53, 1972.
- Lambeck, K., and S. M. Nakiboglu, Seamount loading and stress in the lithosphere, *J. Geophys. Res.*, 85, 6403–6418, 1980.
- Lewis, B. T. R., and L. M. Dorman, Experimental isostasy. 2, An isostatic model for the United States derived from gravity and topographic data, *J. Geophys. Res.*, 75, 3367–3386, 1970.
- Mammerickx, J., Depth anomalies in the Pacific: Active, fossil and precursor, *Earth Planet. Sci. Lett.*, 53, 147–157, 1981.
- McKenzie, D. P., Some remarks on heat flow and gravity anomalies, *J. Geophys. Res.*, 72, 6261–6273, 1967.
- McKenzie, D. P., Surface deformation, gravity anomalies and convection, *Geophys. J. Roy. Astron. Soc.*, 48, 211–238, 1977.
- McKenzie, D. P., and C. Bowin, The relationship between bathymetry and gravity in the Atlantic ocean, *J. Geophys. Res.*, 81, 1903–1915, 1976.
- McNutt, M., Compensation of oceanic topography: An application of the response function technique to the Surveyor area, *J. Geophys. Res.*, 84, 7589–7598, 1979.
- Menard, H. W., Depth anomalies and the bobbing motion of drifting islands, *J. Geophys. Res.*, 78, 5128–5137, 1973.
- Menard, H. W., and T. M. Atwater, Changes in direction of seafloor spreading, *Nature*, 219, 463–467, 1968.
- Menard, H. W., and L. M. Dorman, Dependence of depth anomalies upon latitude and plate motion, *J. Geophys. Res.*, 82, 5329–5335, 1977.
- Ockendon, J. R., and D. L. Turcotte, On the gravitational potential and field anomalies due to thin mass layers, *Geophys. J. R. Astron. Soc.*, 48, 479–492, 1977.
- Oldenburg, D. W., A physical model for the creation of the lithosphere, *Geophys. J. R. Astron. Soc.*, 43, 425–451, 1975.
- Oldenburg, D. W., A comprehensive solution to the linear deconvolution problem, *Geophys. J. R. Astron. Soc.*, 65, 331–357, 1981.
- Parker, R. L., The rapid calculation of potential anomalies, *Geophys. J. R. Astron. Soc.*, 31, 447–455, 1972.
- Parker, R. L., Understanding inverse theory, *Annu. Rev. Earth Planet. Sci.*, 5, 35–64, 1977.
- Parker, R. L., and D. W. Oldenburg, Thermal model of ocean ridges, *Nature Phys. Sci.*, 242, 137–139, 1973.
- Parsons, B., and D. P. McKenzie, Mantle convection and the thermal structure of the plates, *J. Geophys. Res.*, 83, 4485–4496, 1978.
- Parsons, B., and F. M. Richter, A relation between driving forces and geoid anomaly associated with mid-ocean ridges, *Earth Planet. Sci. Lett.*, 51, 445–450, 1980.
- Parsons, B., and J. G. Sclater, An analysis of the variation of the ocean floor bathymetry and heat flow with age, *J. Geophys. Res.*, 82, 803–827, 1977.
- Pollack, H. N., I. G. Gass, R. S. Thorpe, and D. S. Chapman, On the vulnerability of the lithospheric plates to mid-plate volcanism: Reply to comments by P. R. Vogt, *J. Geophys. Res.*, 86, 961–966, 1981.
- Sandwell, D. T., and K. A. Poehls, A compensation mechanism for the Central Pacific, *J. Geophys. Res.*, 85, 3751–3758, 1980.
- Sandwell, D. T., and G. Schubert, Geoid height versus age for symmetric spreading ridges, *J. Geophys. Res.*, 85, 7235–7241, 1980.
- Schubert, G., C. Froidevaux, and D. A. Yuen, Oceanic lithosphere and asthenosphere: Thermal and mechanical structure, *J. Geophys. Res.*, 81, 3525–3540, 1976.
- Sclater, J. G., and J. Francheteau, The implications of terrestrial heat flow observations on current tectonic and geochemical models of the crust and upper mantle of the earth, *Geophys. J. R. Astr. Soc.*, 20, 509–542, 1970.
- Sclater, J. G., R. N. Anderson, and M. L. Bell, Elevation of ridges and evolution of the central eastern Pacific, *J. Geophys. Res.*, 76, 7888–7915, 1971.
- Sclater, J. G., L. A. Lawver, and B. Parsons, Comparison of long-wavelength residual elevation and free-air gravity anomalies in the North Atlantic and possible implications for the thickness of the lithospheric plate, *J. Geophys. Res.*, 80, 1031–1052, 1975.
- Sleep, N. H., and B. Rosendahl, Topography and tectonics of ridge axes, *J. Geophys. Res.*, 84, 6831–6839, 1979.
- Turcotte, D. L., and E. R. Oxburgh, Finite amplitude convection cells and continental drift, *J. Fluid Mech.*, 28, 29–42, 1967.
- Turcotte, D. L., and E. R. Oxburgh, Stress accumulation in the lithosphere, *Tectonophysics*, 35, 183–199, 1976.
- Walcott, R. I., Flexure of the lithosphere at Hawaii, *Tectonophysics*, 9, 435–446, 1970.
- Watts, A. B., An analysis of isostasy in the world's oceans, 1, Hawaiian-Emperor seamount chain, *J. Geophys. Res.*, 83, 5989–6004, 1978.

(Received February 27, 1981;  
revised October 2, 1981;  
accepted October 16, 1981.)